

AFIT/DS/ENP/94-04

AD-A284 852



THE OPTICAL EMISSION AND ABSORPTION PROPERTIES
OF SILICON-GERMANIUM SUPERLATTICE STRUCTURES
GROWN ON NON-CONVENTIONAL SILICON SUBSTRATE ORIENTATIONS

DISSERTATION

Presented to the Faculty of the Graduate School of Engineering

of the Air Force Institute of Technology

Air University

In Partial Fulfillment of the
Requirements for the Degree of
Doctor of Philosophy



Theodore L. Kreifels, B.S., M.S.

Captain, USAF

August 1994

~~18798~~ 94-30537



012 200

DTIC QUALITY INSURED

Approved for public release; distribution unlimited



THE OPTICAL EMISSION AND ABSORPTION PROPERTIES
OF SILICON-GERMANIUM SUPERLATTICE STRUCTURES
GROWN ON NON-CONVENTIONAL SILICON SUBSTRATE ORIENTATIONS

Theodore L. Kreifels, B.S., M.S.
Captain, USAF

Accession For	
NTIS CRA&I	<input checked="" type="checkbox"/>
DTIC TAB	<input type="checkbox"/>
Unannounced	<input type="checkbox"/>
Justification	
By	
Distribution/	
Availability Codes	
Dist	Avail and/or Special
A-1	

Approved:

Robert J Hengsholel

8-11-94

Jung Kee Seo

8-11-94

Byron M. Hill

8-11-94

Paul S. Sunde

8-11-94

Accepted:

Phil Alab

Dean, School of Engineering

Preface

The purpose of this dissertation was to characterize the optical emission and absorption properties of silicon-germanium superlattices grown on non-conventional orientation silicon substrates. The goal of this effort was to validate recent theoretical studies with experimental data in the hope of someday extending the photodetection properties of silicon to the near infrared of electromagnetic region.

This research would not have been possible without a reliable supply of silicon-germanium samples to examine. My sincere thanks to Dr. Phillip Thompson from the Naval Research Laboratory for providing high-quality superlattice structures, his insight, and most important, his constant encouragement. I also wish to thank LtCol Gernot Pomrenke from the Air Force Office of Scientific Research for his financial support to AFIT and NRL—his commitment to this research and to AFIT is much appreciated.

I also wish to thank my advisors, Dr. Robert Hengehold and Dr. Yung Kee Yeo, for sharing so much of their life's work with me, and for having the wisdom to expect much from me when times were good and for being gentlemen when times were bad; the technical staff, especially the talented Greg Smith, who taught me so much in the lab; my unflappable lab assistant, Greg Quinn (may both Gregs live long and prosper); the helpful front office staff, Nancy, Diana, and Karen—they are the best!; Maj Glen Perram, Maj Mike Roggemann, and Capt Jeff Grantham for being such superb military faculty role models, officers, and friends; and of course, my fellow doctoral students for their constant support, friendship, and humor.

Finally, I wish to thank my darling daughter, Donna, for cheerfully accepting little more than a bedtime story each evening and an occasional trip to the park while Daddy was busy at school; and my loving wife, Susan, for setting aside her dreams for three more years so that I could pursue my own.

-tlk

Table of Contents

	Page
Preface	iii
List of Figures	vi
List of Tables	ix
List of Symbols	x
Abstract	xv
I. Introduction	1
II. Background	6
Elemental Properties of Silicon and Germanium	6
Si _{1-x} Ge _x Alloys, Heterostructures and Superlattices	10
Quantum Well and Superlattice Models	14
Zone Folding, Strain, and Doping	17
Photoconduction and Resonant Tunneling	22
Detector Characterization	30
Advanced Treatment of Optical Absorption in SiGe Superlattices	34
Background Summary	53
III. Experimental	55
Samples	55
Photoluminescence	61
Fourier Transform Infrared Spectroscopy	68
FTS Absorption Terms	85
Background Subtraction Techniques	86
Peaks Observed at 3-5 microns Using SPNV Subtraction	92
Signal-to-Noise Ratio Analysis	96
IV. Results and Discussion	101
Confirmation of Photoluminescence Emission from the Superlattice	101
Effects of Growth Temperature on PL Emission	107
Effects of Sample Temperature on PL Emission	114
Structural Uniformity	116
Effects from Doping on Photoluminescence	119
PL Data Supporting FTS Absorption	128

Fourier Transform Spectroscopy: Identification of Absorption Peaks	
Associated with the Si Substrate	130
Validation of Background Subtraction Techniques	133
Absorption Results from NRL Samples	139
Results from the Single Quantum Well and Kronig-Penney Models	144
Determination of Valence Band Selection Rules	149
V. Summary	161
Recommendations for Future Work	165
References	166
Vita	171

List of Figures

Figure	Page
1. A simple schematic diagram describing a basic materials research program.....	4
2. Critical thickness of silicon-germanium alloys.....	11
3. An ideal reverse-biased <i>p-n</i> photodiode detector.....	23
4. Energy band schematic of avalanche multiplication.....	24
5. Avalanche photodiodes designs using band gap engineering. (a) MQW APD; (b) solid-state PMT APD; and (c) channeling APD.....	26
6. A resonant tunneling quantum well.....	28
7. Effective mass filtering in a superlattice photoconductor.....	29
8. Illustration of various transitions in a quantum well structure.....	35
9. Illustration of free-carrier absorption transitions within the conduction and valence bands.....	37
10. The (a) waveguide geometry with no facets, and (b) waveguide with 45 degree facets and original decomposed to perpendicular and normal components.....	39
11. Electric dipole oscillations relative to the quantum well plane in <i>r</i> -space with respect to incident polarized light:.....	40
12. The (a) coordinate system , and (b) surface planes of the first Brillouin zone of a face-centered cubic structure in <i>k</i> -space. Figures (c) and (d) illustrate the coordinate system and the ellipsoid constant-energy electron surface.....	42
13. Schematic diagram of a typical superlattice structure.....	56
14. Parameter space for the research reported in this study.....	58
15. Schematic diagram of radiative transitions between the conduction band (E_C), the valence band (E_V), and exciton (E_E), donor (E_D), and acceptor (E_A) levels in a semiconductor.....	63
16. Schematic diagram of photoluminescence experimental apparatus.....	64
17. Optical system response of photoluminescence apparatus.....	67
18. Michelson interferometer.....	69
19. Functional schematic of the BioRad FTS system.....	77
20. Lapping assembly used to fabricate an optical waveguide.....	79
21. Schematic of sample fashioned into an optical waveguide.....	80
22. Facet geometry of a sample waveguide.....	80

23. Waveguide bevel angle shown as a function of the index of refraction of silicon.....	83
24. FTIR system response curve using the DTGS and PbSe detectors.....	84
25. Schematic illustration absorption definitions.....	85
26. Data plot illustrating relative differences in magnitude of absorption terms.....	87
27. Various background subtraction techniques used in this study.....	88
28. FTIR absorption data of similar SL structures on different substrate orientations in single-pass, normal-view mode.....	93
29. Plot of Eq(9) illustrating phase angle effects of an etalon.....	95
30. SNR data analysis for FTIR system using SPNV and waveguide configurations.....	100
31. PL spectra from (100), (110), and (111) silicon substrates.....	102
32. SIMS plot of a SiGe superlattice grown at 550 °C on (110) Si.....	104
33. PL spectra of undoped SiGe superlattices as a function of Ge composition.....	106
34. PL spectra of six SiGe (100) samples with similar superlattice structures grown at different substrate temperatures.....	108
35. PL spectra of three SiGe (110) samples with similar superlattice structures grown at different substrate temperatures.....	111
36. PL spectra of three SiGe (111) samples with similar superlattice structures grown at different substrate temperatures.....	112
37. PL spectra of a (100) SiGe superlattice as a function of sample temperature.....	115
38. PL spectra of a (110) SiGe superlattice as a function of sample temperature.....	117
39. PL spectra of a (111) SiGe superlattice as a function of sample temperature.....	118
40. PL spectra of (100) SiGe superlattice showing wafer uniformity as a function of radial distance from center.....	120
41. PL spectra of (110) SiGe superlattice showing wafer uniformity as a function of radial distance from center.....	121
42. PL spectra of (111) SiGe superlattice showing wafer uniformity as a function of radial distance from center.....	122
43. PL spectra of (100) SiGe superlattices with valence band wells which have been center-doped with boron.....	124
44. PL spectra of (100) SiGe superlattices with boron doped VB wells as a function of Ge composition.....	125
45. PL spectra of (110) SiGe superlattices with valence band wells which have been center-doped with boron.....	126

46. PL spectra of (111) SiGe superlattices with valence band wells which have been center-doped with boron.....	127
47. PL spectra of a (100) SiGe superlattice before and after waveguide fabrication..	129
48. Absorption spectrum of a Czochralski <i>p</i> -type (100) silicon substrate.....	131
49. FTIR absorption spectra of an InGaAs/AlGaAs superlattice using the SelfRef and Fresnel Angle background subtraction techniques.....	134
50. FTIR absorption of five InGaAs/AlGaAs superlattices with different well widths.....	136
51. FTIR absorption spectra of a <i>p</i> -type SiGe superlattice as a function of polarization (SLRef).....	137
52. FTIR absorption of SiGe sample 40504.1(100) as a function of polarization (SubRef).....	140
53. FTIR absorption of NRL sample 40504.1(100) as a function of polarization (SelfRef).....	142
54. FTIR absorption of SiGe sample 40504.1(100), background leveled (SelfRef).....	145
55. Bandgap schematic for a SiGe structure.....	148
56. Selection rules for allowed valence-band transitions on (a) (100), (b) (110), and (c) (111) Si substrates.....	155
57. FTIR absorption of similar SiGe (110) structures as a function of boron dopant concentration (SelfRef).....	159
58. Background-leveled FTIR absorption of similar SiGe (110) structures as a function of boron dopant concentration (SelfRef).....	160

List of Tables

Table	Page
I. Atomic, thermal, electronic, magnetic, and mechanical properties of intrinsic silicon and germanium.....	6
II. Theoretical results for absorption coefficients of Si and Ge on various substrates.....	47
III. Summary of intersubband, intervalence-subband, and free-carrier transitions observed in $\text{Si}_{1-x}\text{Ge}_x/\text{Si}$ MQWs as a function of incident light polarization and silicon substrate.....	52
IV. Superlattice IR detectors and crystal orientations reviewed in literature.....	54
V. Design considerations for each physical region of a superlattice.....	57
VI. List of samples used in this research.....	59
VII. Absorption coefficients and penetration depths of available laser lines.....	62
VIII. Currently available detectors, associated beamsplitters, and their effective range for the Bio-Rad FTS-60A.....	78
IX. PL emission peaks due to boron impurity in Si substrates.....	104
X. Identified phonon-assisted transitions measured below the no-phonon line....	107
XI. Multi-phonon transition peaks for bulk Si substrate.....	131
XII. Selection rules for allowed valence-band transitions on (100), (110), and (111) Si substrates.....	154
XIII. Transition wavelengths between HH and LH states within the SiGe valence band well.....	157

List of Symbols

AES	Auger electron spectroscopy
AFIT	Air Force Institute of Technology
AFM	atomic force microscopy
APD	avalanche photodiode
AOM	acoustic optical modulator
BE	bound exciton
BGN	bandgap narrowing
BICFET	bipolar inversion channel field effect transistor
BJT	bipolar junction transistor
BMEC	bound multi-exciton complexes
CB	conduction band
CCD	charge coupled device
CL	cathodoluminescence
CMOS	complimentary metal oxide semiconductor
CV	capacitance-voltage
CVD	chemical vapor deposition
CZ	Czochralski zone
DHBT	double heterostructure bipolar transistor
DHBT	double heterostructure bipolar transistors
DLTS	deep level transient spectroscopy
DOES	double heterostructure optoelectronic switching
DOS	disk operating system
DRAM	dynamic random access memory

EHD	electron-hole drop
EL	electroluminescence
EL	electron level
EXDS	energy dispersive x-ray spectroscopy
FE	free exciton
FET	field effect transistor
FTIR	Fourier transform infrared spectroscopy
FTS®	Fourier transform spectroscopy (registered trademark of Bio-Rad Inc.)
FZ	float zone
GSMBE	gaseous source molecular beam epitaxy
HBT	heterostructure bipolar transistors
HEMT	high electron mobility transistors
HH	heavy hole
HHMT	high hole mobility transistor
I-V	current-voltage
IBE	isoelectronic bound exciton
IC	integrated circuit
IMPATT	impact ionization avalanche transit time
IR	infrared
ISCB	intersub-conduction band
ISVB	intersub-valence band
LA	longitudinal acoustic
LDA	local density approximation
LED	light emitting diode
LEED	low-energy electron diffraction
LH	light hole

LO	longitudinal optical
LPE	liquid phase epitaxy
LSI	very large scale integration
LWIR	long wavelength infrared
MBE	molecular beam epitaxy
MISFET	metal insulator semiconductor field-effect transistor
MIR	multiple internal reflection
MITATT	mixed tunneling avalanche transit time
ML	monolayer
MOCVD	metal organic chemical vapor deposition
MODFET	modulation doped field effect transistor
MOS	metal oxide semiconductor
MOSFET	metal oxide semiconductor field effect transistor
MQW	multiple quantum well
NLO	nonlinear optics
NP	no phonon
NP/pr	no phonon/phonon replica
NRL	Naval Research Laboratory
ODMR	optically detected magnetic resonance
OPA	optical parametric amplifier
OPO	optical parametric oscillator
<i>p-i-n</i>	<i>p</i>-type/<i>i</i>ntrinsic/<i>n</i>-type (semiconductor structure)
<i>p-n</i>	<i>p</i>-type/<i>n</i>-type (semiconductor structure)
pin	<i>p</i>-type/<i>i</i>ntrinsic/<i>n</i>-type (semiconductor structure)
PL	photoluminescence
PLE	excitation photoluminescence

PMT	photomultiplier tube
QW	quantum well
RB	Rutherford backscattering
RBS	Rutherford backscattering spectroscopy
RHEED	reflected high energy electron diffraction
RS	Raman spectroscopy
RT	resonant tunneling
RTA	rapid thermal annealing
RTCVD	rapid thermal processing and chemical vapor deposition
SEED	self electro-optic effect device
SelfRef	self reference
SEM	scanning electron microscopy
SIMS	secondary-ion mass spectrometry
SL	superlattice
SLRef	superlattice reference
SLS	strained layer superlattice
SNR	signal-to-noise ratio
SPNV	single pass normal view
STM	scanning tunneling microscopy
SubRef	substrate reference
TA	transverse acoustic
TEM	transmission electron microscope
TO	transverse optical
TRPL	time resolved photoluminescence
UHV	ultra high vacuum
ULSI	ultra large scale integration

UPS	ultraviolet photoelectron spectroscopy
VB	valence band
VLSI	very large scale integration
VLWIR	very long wavelength infrared
XPS	x-ray photoelectron spectroscopy

Abstract

Optical emission and absorption properties of $\text{Si}_{1-x}\text{Ge}_x/\text{Si}$ superlattices grown on (100), (110), and (111) Si substrates were investigated to determine the optimal growth conditions for these structures to be used as infrared detectors. Fully-strained $\text{Si}_{1-x}\text{Ge}_x/\text{Si}$ superlattices were grown by molecular beam epitaxy (MBE) and examined using low-temperature photoluminescence (PL) to identify no-phonon and phonon-replica interband transitions across the alloy bandgap. Phonon-resolved emission was most intense for undoped quantum wells grown at 710 °C for all three silicon orientations. Room temperature absorption measurements were conducted on (100) and (110) $\text{Si}_{1-x}\text{Ge}_x/\text{Si}$ superlattices using Fourier transform spectroscopy while varying incident electric field polarization. Absorption samples were fashioned into waveguides to enhance multiple internal reflection. Strong intersubband absorption was observed at 7.8 μm from a sample composed of 15 quantum wells of 40 Å $\text{Si}_{0.8}\text{Ge}_{0.2}$ separated by 300 Å of Si grown on (100) Si by MBE at 550 °C. Valence band wells were doped $5 \times 10^{19} \text{ cm}^{-3}$ with boron. This transition, identified as $\text{HH1} \leftrightarrow \text{HH2}$, exhibited strong polarization dependence according to (100) Si selection rules. No subband transitions were observed on similar (110) $\text{Si}_{1-x}\text{Ge}_x/\text{Si}$ superlattices ranging in boron dopant from $1-8 \times 10^{19} \text{ cm}^{-3}$. Selection rules for (110) Si indicate an $\text{HH1} \leftrightarrow \text{LH2}$ transition is allowed within the transmission bandpass of the experimental apparatus at both parallel and normal incident electric field polarizations; however, this peak was most likely masked by free-carrier absorption which dominated the spectrum. Intersubband absorption transitions were observed only for doped superlattices grown at 550 °C. A clear correlation between PL emission and photo-absorption was unattainable since the growth conditions necessary to ameliorate intersubband absorption quenches interband emission.

THE OPTICAL EMISSION AND ABSORPTION PROPERTIES
OF SILICON-GERMANIUM SUPERLATTICE STRUCTURES
GROWN ON NON-CONVENTIONAL SUBSTRATE ORIENTATIONS

I. Introduction

In the past two decades the linear feature size of transistor circuits available on the market has decreased by 50% every 2 years¹ to their present micron scale. To maintain this rate of reduction, the electronics industry would need to reach sub-nanometer dimensions by the end of the next two decades, meaning simple devices and circuits would be the length of only a few atomic spacings! Presently, reducing circuit dimensions and increasing their speed have become trade-offs between gain and base resistance, base width and breakdown voltage, and collector capacitance of the basic circuit material.² However, at sub-nanometer dimensions, established concepts such as Ohm's law and macroscopic definitions like resistance and capacitance lose their meaning. As a result, today's researchers now strive for new understanding and new possibilities in the physical world that lies between micro- and macroscopic principles.

One new possibility would be the total integration of several electro-optic devices on a monolithic semiconductor crystal. The practical uses for such a "superchip" would be phenomenal. Optical detection, charge carrier transport and amplification, light emission and wave guiding, and electro-optic switching to other external circuits—all on a single photonic chip—would revolutionize the electronics and computer industries and have an enormous impact on several device applications.

The first totally integrated photonic circuit would not only allow engineers to build smaller circuits than ever before, but would also require the electro-optical properties of a

material, or its electronic bandgap, to be tailored for specific uses. Photoresponse, refractive index, and charge carrier amplification would be engineered from the same base material(s), but configured in clever structures to meet design objectives. However, until the mid-1970's, scientists and engineers could only study the characteristics of bulk semiconductor materials, or a crude alloy of materials, and work within those physical properties. A variety of ingenious devices were constructed to modulate current, detect and emit light via individual solid-state transistors, photodiodes, lasers. Much effort was spent developing ways to grow ultra-pure materials and study the consequences of doping base materials. At the same time, smaller circuits were made with ever increasingly sophisticated photolithographic techniques. But until that time, man had continued to make small, complex electronic devices from bulk materials. Not until the arrival of highly-controlled semiconductor growth techniques such as molecular beam epitaxy in 1975, could extremely thin planes of material be grown as epilayers on bulk substrates. Today, essentially two-dimensional planes of a material, only 1-2 atoms thick, can be grown routinely. This new growth technology has allowed scientists to now experimentally investigate quantum size structures which were formerly only theoretical concepts.

This dissertation investigates the optical emission and absorption properties of several silicon-germanium superlattices grown on three silicon substrates: the conventional orientation, [100], and two non-conventional orientations, [110] and [111]. The goal of this research is to provide the experimental evidence needed to someday design and build a silicon-based infrared detector that can efficiently detect light at normal incidence. I chose to investigate superlattices grown on non-conventional silicon substrates, primarily because recent papers^{3,4} have provided theoretical evidence indicating that bandgap alignments and electronic transition rules predict strong, normal-incidence absorption at these orientations. Developing such a detector could be one of the

first steps towards a totally integrated photonic circuit on a non-conventional silicon substrate, or, at least, inspire a variety of novel devices in important applications.

Focused materials research must always start and end with a specific device application in mind to guide the material selection and characterization process. This process usually starts with a commercial, industrial, medical, or military need defining the device application. Next, a material is selected with properties favorable for this application. It is important to note that all of the material qualities must be considered at this stage—mechanical, chemical, thermal, as well as electrical and optical—in light of the specific application. The device will not serve as a useful conductor, for example, if it melts in its operating environment or is too brittle to withstand vibration. Next, the material is characterized for the specific application and this information is coordinated with what is already known about the material. A simple device is fabricated and studied, and after the critical features are fine tuned, the device is made. Figure 1 illustrates this process in a simplified schematic diagram. This study contributes to Phase I and part of Phase II shown in this diagram.

Specifically, the optical emission and absorption characteristics of silicon-germanium superlattice structures grown on non-conventional silicon substrate orientations were investigated. Superlattice structures were designed at the Air Force Institute of Technology (AFIT) to preferentially trap holes at discrete energy levels in valence band wells, and later grown at the Naval Research Laboratory (NRL). The surface morphology of each sample was studied using Nomarski microscopy at NRL and the samples sent to AFIT for optical diagnostics. The physical integrity of a select few structures was confirmed by transmission electron microscopy (TEM) and secondary-ion mass spectrometry (SIMS) at NRL. The samples were examined at AFIT using photoluminescence (PL) to first identify the no-phonon, transverse-optical, and transverse-acoustic emission peaks, and then to track peak shifts as a function of germanium

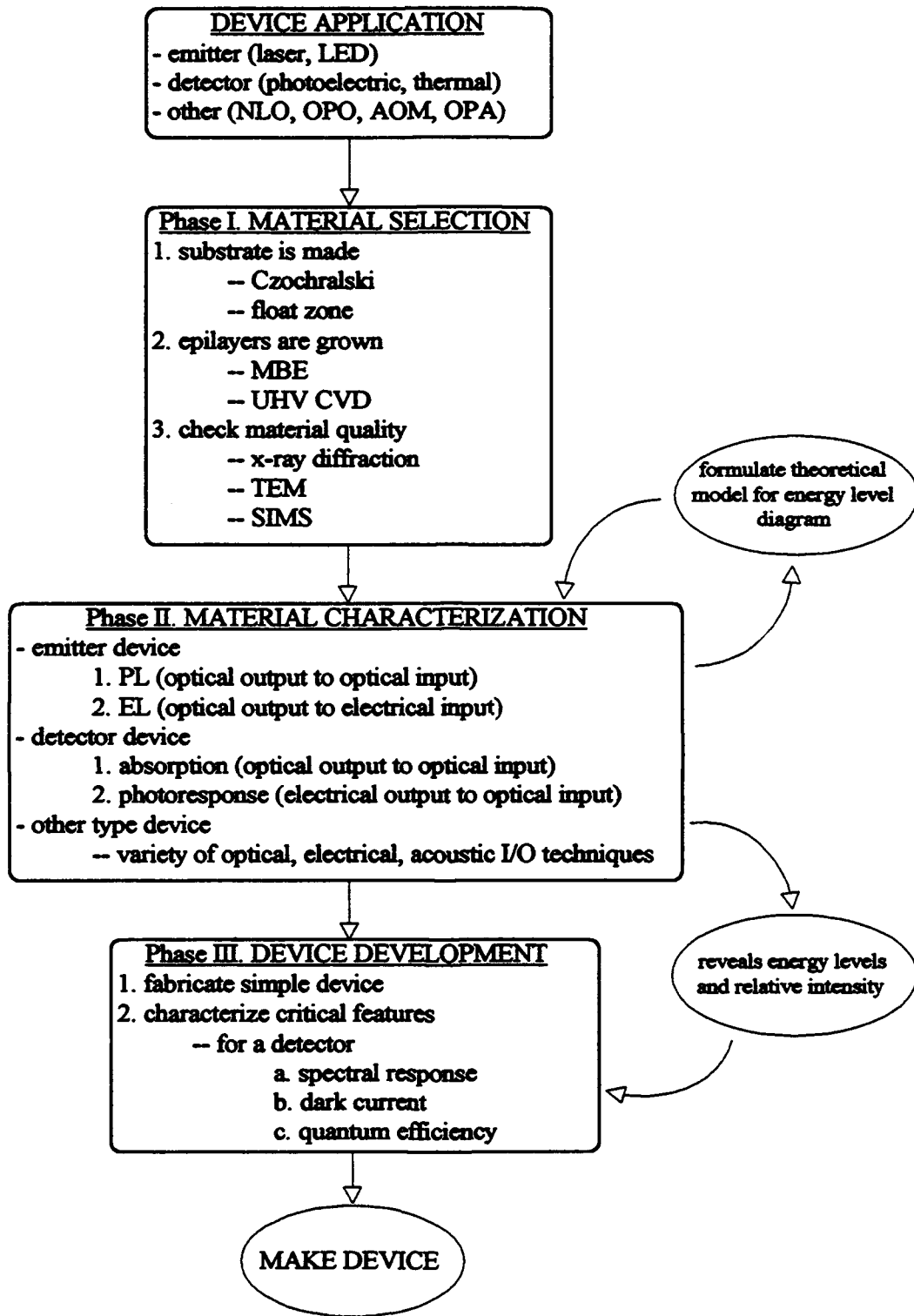


Figure 1. A simple schematic diagram describing a basic materials research program.

composition, sample temperature, doping concentration, and wafer position. The samples were next fashioned into waveguides and examined using Fourier transform infrared spectroscopy (FTS®) to identify absorption peaks. Normal incidence absorption was studied as a function of substrate crystal orientation and dopant concentration by varying the polarization of the incident light as it passed through the sample waveguide.

This dissertation is organized in the following manner: Chapter I introduces the topic, provides motivation for the research, and briefly explains the research goals and methods. Chapter II gives a detailed background of previous research in this field, starting with the elemental properties of silicon, germanium, and their alloys to the development of heterostructures, superlattices, detector characterization, and a review of key advanced papers leading to this research. Chapter III describes the sample specifications and experimental apparatus and procedures. Chapter IV reports the results of this research and discusses the important trends in the data, comparing this data with previous work and theory. Finally, Chapter V summarizes the important results, and concludes with recommendations for future research.

II. Background

Elemental Properties of Silicon and Germanium

Silicon and germanium are semiconducting elements with a diamond lattice crystalline structure. Both elements belong to the cubic crystal family and may be viewed as two interpenetrating face-centered cubic (FCC) sublattices with one sublattice displaced from the other by one quarter of the distance along a diagonal of the cube. Each atom is surrounded by four equidistant nearest neighbors placed at tetrahedral angles.

Nature has provided us with a virtually inexhaustible supply of these materials. Silicon is the second-most abundant element in the earth's crust. It is also extremely easy to extract and relatively easy to isolate (or refine) to an ultra pure form. Silicon and germanium are both Column IV elements and perfectly suited for each other chemically, each sharing four strong covalent bonds. They are also very durable materials with excellent mechanical and thermal properties.

Since the early 1950s, intrinsic silicon and germanium, and their bulk crystalline alloys, have benefited from continuous research and ongoing device development (see review article⁵ by Jain). The atomic, thermal, electronic, magnetic, chemical, and mechanical properties of intrinsic silicon and germanium are well understood and summarized in Table I.

Table I. Atomic, thermal, electronic, magnetic, and mechanical properties of intrinsic silicon and germanium.⁶

PROPERTIES	UNITS	Silicon (Si)	Germanium (Ge)
Atomic number	-	14	32
Atomic weight	(based on C ¹²)	28.086	72.59
Periodic classification	-	IV A	IV A
Atomic volume	cm ³ /g·atom	12.07	13.5

PROPERTIES	UNITS	Silicon (Si)	Germanium (Ge)
Atomic radius	Å	1.18	1.22
Ionic radius	Å	0.41 (Si ⁴⁺)	0.53 (Ge ⁴⁺)
Density	g/cm ³	2.33	5.323
Lattice type	-	FCC, diamond	FCC, diamond
Lattice constant, a	Å	5.417	5.658
Valence electrons	-	3s ² 3p ²	4s ² 4p ²
Melting point	°C	1412	934
Boiling point	°C	2480	2827
Critical temperature	K	4920	5642
Linear thermal expansion coefficient	10 ⁻⁶ cm/cm/°C	4.2	5.75
Specific heat	cal/g/°C	0.162	0.074
Electronic specific heat	10 ⁻⁴ cal/mole/°C ²	0.050	0
Thermal conductivity	cal/cm ² /cm/sec/°C	0.20	0.15
Latent heat of fusion	kcal/mole	12.0	7.6
Latent heat of vaporization at B.P.	kcal/mole	71	79.9
Heat of combustion	kcal/mole	191 (to SiO ₂)	
Heat of sublimation	kcal/mole	108.4	89.5
Heat capacity at constant pressure	cal/°C/mole	4.64	5.47
Heat content at M.P.	kcal/mole	8.07	5.81
Entropy	cal/°C/mole	4.50	7.43
Longitudinal sound velocity	m/sec	9101	4914 (001)
Electrical resistivity	microohm·cm	2.3x10 ⁵	47x10 ⁶
Photoelectric work function	eV	4.1	4.56
First ionization potential	eV	8.151 (Si ⁺)	7.899 (Ge ⁺)
Oxidation potential	V	1.2 (acid, Si/SiO ₂)	0.0 (Ge ²⁺)
Electrochemical equivalent	mg/Coulomb	0.07269 (Si ⁴⁺)	0.1881 (Ge ⁺)
Magnetic susceptibility	c.g.s. units	-0.13x10 ⁻⁶	-0.10x10 ⁻⁶
Refractive index	-	3.45 (at 2 μm)	4.10 (at 2 μm)
Young's modulus of elasticity	10 ⁻⁶ kg/cm ²	1.05	1.01
Shear modulus	10 ⁻⁶ kg/cm ²	0.405	0.40
Bulk modulus	10 ⁻⁶ kg/cm ²	1.008	0.7874
Poisson's ratio	-	0.44	0.27

Not only is our scientific knowledge of these materials well established, but our nation's silicon-based electronics design and manufacturing industry is very mature. Very large scale integration (VLSI) of integrated circuits (ICs) are highly developed for silicon. Isolation and growth techniques, material deposition, photolithography, contact technology, etching methods—in effect, all aspects of device fabrication are in place.

Then it becomes especially important to note that existing Si-Ge photonic devices of all types are compatible with this technology. From a compelling geo-political view, consider that essentially all of the world's integrated circuits are silicon-based. If we can extend the capabilities of silicon into the near infrared (IR), the nation would be well-positioned to exploit our advantage in this market and secure defense-related technology.

However, silicon and germanium have two serious material disadvantages: both elements suffer from (1) an indirect band gap, and (2) low charge-carrier mobilities compared to other semiconductors such as gallium-arsenide (GaAs). Intrinsic silicon, for example, is a very poor optical emitter. Silicon will not lase or even undergo appreciable luminescence without strong excitation. In addition, bulk silicon and germanium have lower optical absorption than many other materials. Furthermore, the index of refraction is essentially constant over a relatively wide range. For example, the index of refraction of single-crystal silicon at room temperature changes only from 3.4975 to 3.4176 over a wavelength range from 1.357 to 11.04 μm . The index of refraction of germanium is even less sensitive: it varies from 4.1016 to only 4.0021 over a wavelength range from 2.0581 to 13.02 μm . Obviously, this poses a problem if you wish to build a waveguide or an electro-optic modulator.

However, silicon photodiodes set the standard for semiconductor detectors in the visible. Silicon's 1.12 eV band gap is large enough to reduce generation and recombination noise to negligible levels, yet small enough for photodiodes to remain sensitive. Fabricating a silicon photodetector on a silicon IC is trivial from a present-day technology

point of view. Yet, silicon's usefulness as a detector quickly diminishes beyond its abrupt absorption edge near $\lambda=1.1 \mu\text{m}$. (Recall, energy (in eV) = $1.24 / \lambda$ (in μm)). Germanium has a band gap of approximately 0.7 eV at 300 K and remains responsive only out to approximately $\lambda=1.5 \mu\text{m}$.

This is unfortunate because there presently exists much scientific interest in the near to mid IR and a great need for high-speed devices that can couple directly to existing silicon devices. Optical telecommunications (OTCs) and data networks (ODNs) operate at $1.3 \mu\text{m}$ with only a 0.6 dB/km loss in GeO_2 -doped silica optical fiber.⁷ Remote sensing and active imaging concepts also use laser illuminators operating anywhere from 1-12 μm . Several more applications in the communications industry, astronomy, medicine, and the military are all creating a deep niche to fill for fast, sensitive, solid-state detectors responsive in these regions of the electromagnetic spectrum.

In 1984, Luryi *et al.* developed the first single-crystal Si-Ge *p-i-n* diode grown on silicon by molecular-beam epitaxy (MBE).⁸ Although they reported a quantum efficiency of 41% at 300 K, the germanium epilayer grown on the silicon substrate had several dislocations attributed to a mismatch in the lattice constant of the two materials at the interface. The defects threaded up through the germanium mesa comprising the *p-i-n* diode causing relatively high dark current.

To overcome the growth defects created by an abrupt interface of these two materials, the next logical step was to investigate if an alloy or a superlattice of silicon and germanium could be made. However, for Si-Ge alloys and superlattices to succeed, crystal growers had to first obtain excellent two-dimensional growth, morphology, and crystalline quality, while considering other important growth parameters such as critical thickness and strain.

Si_{1-x}Ge_x Alloys, Heterostructures and Superlattices

Extensive studies^{9,10,11} of the optical and electronic properties of bulk Si_{1-x}Ge_x alloys have determined that the alloy band gap is a function of composition, with a Si-like conduction band (CB) minima in the [100] direction up to an 85% Ge composition, beyond which the CB behaves more Ge-like with minima in the [111] direction. The study by Herman *et al.* established that the alloy band structure was highly dependent on the ordering of the Si and Ge atoms within the alloy.

Strain changes the energy band gap and the subsequent change to the optical and electronic properties of strained-layer alloys can be significant. Although the band gap remains indirect, the strain splits the degeneracies of the conduction and valence bands, affecting charge carrier mobilities.¹² Yet without methods of making highly-ordered alloys, studies in alloy composition and strain remained dormant for nearly 25 years until several engineering advances in materials growth took place.

Single-crystal Si-Ge alloys were difficult to grow because the lattice constant of Si and Ge differ by over 4% ($a_{\text{Si}}=5.431 \text{ \AA}$, $a_{\text{Ge}}=5.657 \text{ \AA}$). Bean *et al.* established that high-quality epilayers could be grown provided that, generally, (1) the lattice mismatch is small, (2) the growth temperature is kept within a certain range, and (3) the epilayers do not exceed their critical thickness h_c .¹³ The critical thickness is the maximum thickness a good quality layer or superlattice can be grown without introducing misfit dislocations and depends on alloy composition (see Figure 2).

Since $a_{\text{Si}} < a_{\text{Si-Ge}} < a_{\text{Ge}}$, a Si-Ge alloy grown on a Si substrate has biaxial compression in the plane of the surface and extension normal to the surface causing a tetragonal distortion in the growth direction (the opposite is true if the SiGe alloy is grown on a Ge substrate). The lattice constants of bulk Si_{1-x}Ge_x alloys have been measured by several researchers^{14,15} and found to obey Vegard's Law:

$$a_{SiGe} = a_{Si} + (a_{Ge} - a_{Si})x = a(x) . \quad (1)$$

In this fashion, crystalline mismatch is accommodated entirely by elastic strain in the epilayer. The growth of such an epilayer is called pseudomorphic, commensurate, or coherent. In 1975, the first high quality pseudomorphic layers of $Si_{1-x}Ge_x$ were grown on silicon by Kasper¹⁶ using ultrahigh vacuum (UHV) epitaxy.

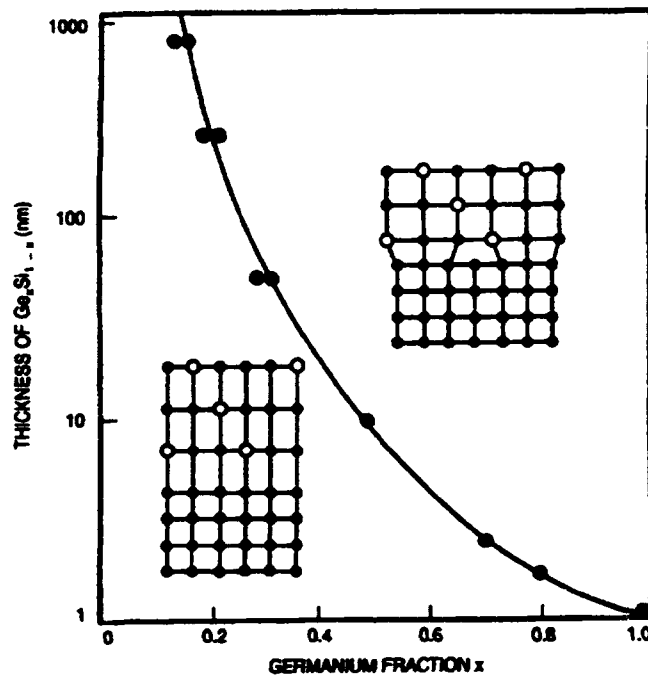


Figure 2. Critical thickness of silicon-germanium alloys.¹³

The advantages of these strained epitaxial layer $Si_{1-x}Ge_x$ alloys were quickly applied in several modified silicon devices. Researchers at AT&T Bell Laboratories successfully built an avalanche photodiode (APD) which exploited the reduced band gap of the strained alloy layer.¹⁷ In this case, the active strained layers were sandwiched between higher index layers of Si providing a waveguide transverse to the growth direction. Here,

the waveguide structure provides the long absorption path needed to compensate for the low absorption coefficient of the indirect band gap alloy.

$\text{Si}_{1-x}\text{Ge}_x$ alloys have also been used to produce Si-based heterojunction bipolar transistors (HBTs).^{18,19} In an ideal device, the HBT base resistance is kept low by doping the base region with a higher dopant concentration than the emitter region. For Si-Ge HBTs, the base region consists of a $\text{Si}_{1-x}\text{Ge}_x$ alloy layer which has a lower band gap than the Si emitter region. The band gap difference between the Si and alloy regions results in a large valence band off-set, creating an energy barrier for holes injected from the base into the emitter, further increasing hole concentrations. This reduces the base resistance and base width, which increases the switching speed of the transistor.²⁰

During this same period, another crystal growth technique, molecular-beam epitaxy (MBE) was being developed. Invented at Bell Laboratories in 1975 by Cho and Arthur,²¹ the MBE technique could grow multi-layer heterojunction structures with abrupt interfaces and precisely controlled doping profiles over distances as short as one or two atomic monolayers. Finally, the concept of a superlattice structure, first proposed in 1969 by Esaki and Tsu,²² could be realized.

A superlattice is a periodic alternation of two or more crystalline epilayers which exhibits unique optical and carrier transport properties which differ from the bulk constituents. These alternating layers cause a 1D spatial variation of the conduction band (CB) and valence band (VB) edges. By placing an ultra thin lower-gap semiconductor epilayer between two wide-gap epilayers one can create a potential well with quantized energy levels. An "ultra thin" epilayer is comparable to the thermal de Broglie wavelength of an electron (e.g., 12 Å at 1 eV or about 6 atomic spacings). The quantum well (QW) depth is the energy difference between the bottom of the conduction bands (or valence bands in the case of holes) in the two materials and is also called a band discontinuity. The spacing and position of the discrete energy levels in the well depend on well thickness and

depth. Multiple quantum wells (MQWs) are formed by repeating this structure two or more times. The period of the MQW structure is the sum of the well and barrier thickness. MQWs superimpose a new, artificial periodicity onto the underlying crystalline lattice, thus literally forming a "superlattice".

The potential offered by these new materials spurred further advances in various growth and device fabrication techniques. Several types of superlattices were constructed by periodically alternating ultra thin n- and p-type layers,²³ grading the composition,²⁴ or by alternating undoped layers with doped layers with a wider band gap.²⁵ When MQW barriers are made very thin, typically $<50 \text{ \AA}$, then tunneling between the coupled wells becomes significant and carrier mobility increases drastically. Manasevi *et al.*²⁶ was one of the first to observe this unusual mobility enhancement in superlattice structures. Today, the term superlattice now refers to the special case of multiple quantum wells which are sufficiently thin to enable this tunneling mobility.

The ultimate speed of any electronic device depends on time constants that are products of device resistance and capacitance. Reducing resistance, or higher charge carrier mobility, leads to higher device speeds. Since ionized donor atoms are a significant source of resistance through scattering which limits charge carrier mobility, then by spatially separating the active region of a device from the donor ions, as in a superlattice, one can reduce Coulombic scattering and lower the effective resistance of the region.

The most optically responsive material is one in which the CB minima are aligned with the VB maxima in momentum (or k-) space resulting in a direct transition energy band gap. When the CB minima are not aligned with the VB maxima in k-space the gap is described as indirect and requires phonon assistance for a downward energy transition.

A superlattice may also be classified by the alignment of the conduction and valence band with the material epilayers in real (or r-) space. This band alignment, Type I or Type II, determines the electron-hole recombination length and thus the optical proper-

ties of the superlattice. A Type I alignment is one in which the conduction band minima and valence band maxima are aligned in r -space in the same epilayer. This spatial alignment results in shorter recombination lengths and more intense luminescence.

Si-Ge band alignments are normally Type II with a CB minimum in the Si layers and a VB maximum in the Ge layers. For growth on silicon, the band difference between Si and Ge results in a valence band offset of 0.78 eV, with a conduction band offset of 0.15 eV.²⁷ For growth on $\text{Si}_{0.5}\text{Ge}_{0.5}$, the VB offset is relatively unchanged at 0.77 eV but the CB offset becomes 0.83 eV. In addition, Si, Ge, and their alloys are also indirect band gap materials. A theoretical study by Gell²⁸ investigated conditions necessary for both a direct band gap and a Type I band alignment. He determined that Si-Ge superlattices grown on a $\text{Si}_{1-x}\text{Ge}_x$ buffer with x ranging from 0.6 to 0.8 would yield a parallel lattice constant between the bulk Si and Ge values in a Type I direct band gap superlattice. Calculations by Froyen *et al.*²⁹ confirmed that direct band gap Si-Ge superlattices must have a parallel lattice constant greater than the average of bulk Si and Ge lattice constants.

Quantum Well and Superlattice Models

To determine the band-to-band and intersubband transition energies of multiple quantum well structures, one first needs to develop a model to establish the approximate energy levels of a simple multiple quantum well structure. The simplest, yet crudest model always begins with the classic "particle in a box" depiction requiring the one-dimensional, time-independent Schrödinger equation:

$$-\frac{\hbar^2}{2m^*} \frac{\partial^2 \psi(z)}{\partial z^2} + U(z)\psi(z) = \xi\psi(z) \quad (2)$$

where \hbar is Planck's constant, h divided by 2π ; m^* is the particle effective mass, ψ is the particle wave function; z is the growth direction; U is the potential energy of the well; and ξ is the confinement energy levels of the well. In the most basic approximation of this

model, one may assume a single, infinitely tall well ($U = \infty$). This assumption eliminates the second term of the left-hand side of Eq. (2), leaving a second-order ordinary differential equation with a single trigonometric (sine or cosine) solution with discrete energy eigenvalues. The next step in difficulty, and therefore, accuracy, is to assume a single well exists with a *finite* depth, that is, U now represents the conduction or valence band energy offset, and $U=0$ elsewhere. With a finite potential energy, U , one arrives at two transcendental trigonometric solutions³⁰ which satisfy both even (symmetric) and odd (asymmetric) discrete energy solutions and may be solved graphically or numerically:

$$k \tan\left(\frac{kl_w}{2}\right) = \kappa$$

and

$$k \cot\left(\frac{kl_w}{2}\right) = -\kappa,$$

where l_w, l_b are the well and barrier widths; and k, κ are the propagation constants defined as

$$k = \sqrt{\frac{2m\xi}{\hbar^2}}$$

and

$$\kappa = \sqrt{\frac{2m(U(z) - \xi)}{\hbar^2}}$$

If N identical quantum wells are grown with barriers sufficiently thin to allow tunneling, then the wave functions of the single-electron particle in each well interact and the total wave function becomes an array of N square-well potentials. To solve for the discrete energy eigenvalues for *multiple* quantum wells, one must account for this neighboring well interaction. In 1931, Kronig and Penney made a significant contribution³¹ in the treatment of electron energies in solids by arriving at an exact

solution to the Schrödinger equation for an ideal, infinitely long, periodic, one-dimensional, square-well potential. If N is extremely large, say, on the order of Avogadro's number, then each of the single-well levels split into N levels spaced so close together that they form nearly continuous energy bands. Since the potential energy function has the the periodicity of the wells, $U(z+d) = U(z)$, where $d = l_w + l_b$, then one expects the solution to have the same periodicity, assuming one doesn't encounter the "last well". This conceptual difficulty is mitigated by imagining that the multiple well structures extend to infinity or that the ends "join" together to form a closed ring.

A solution that satisfies the Bloch condition on the wave function may be written in the form of the product of a plane wave and function having the periodicity of the structure:

where
$$\psi(z) = e^{ikz} u(z) ,$$

$$u(z+d) = u(z) ,$$

thus
$$\psi(z+d) = e^{iqd} \psi(z) ,$$

where q is the Bloch wave vector. The solutions to Eq. (2) are now assumed to be of the form

and
$$\psi(z) = Ae^{ik_w z} + Be^{-ik_w z} \quad \text{for } 0 < x < l_w ,$$

$$\psi(z) = Ce^{ik_b z} + De^{-ik_b z} \quad \text{for } l_w < x < d ,$$

where
$$U(z) = 0 \quad \text{for } 0 < x < l_w ,$$

and
$$U(x) = 0 \quad \text{for } l_w < x < d ,$$

and where
$$k_w = \sqrt{\frac{2m_w \xi}{\hbar^2}} ,$$

and
$$k_b = \sqrt{\frac{2m_b (U(z) - \xi)}{\hbar^2}} ,$$

where k_w and k_b are the propagation constants for the well and barrier respectively.

The coefficients A , B , C , and D can be determined as the solution set of four simultaneous linear homogeneous equations with no other possible solution than $A = B = C = D = 0$ unless the determinant of the coefficients equals zero. Solving the determinant then yields an exact solution of the Schrödinger equation in the familiar form of the dispersion relation:

$$\cos(qd) = \cos(k_w l_w) \cosh(k_b l_b) + A \sin(k_w l_w) \sinh(k_b l_b), \quad (3)$$

where

$$A = \frac{m_b k_w}{m_w k_b}.$$

Eq. (3) may be solved numerically for ξ to determine the quantum confinement energies for either the conduction or valence band. Solutions to ξ when $q=0$ define a set of quantum levels which depend upon the well potential energy, well width, and effective mass.

For $\text{Si}_{1-x}\text{Ge}_x$ structures on (100) and (111) Si, the valence band heavy hole (HH), light hole (LH), and spin-orbit (SO) subbands are uncoupled so that each can be computed separately for a first-order approximation using either the single quantum well or Kronig-Penny solutions. Although, the HH, LH, and SO bands are coupled for (110) Si, the single quantum well approach still yields values within 10-15% of more sophisticated quantum well models. One estimates the bandgap by computing the first ground state of the valence band, HH1, and adding this value to the gap difference arrived at using empirical relations. The Kronig-Penny dispersion relation has a reported accuracy in earlier studies³² to within tens of meV for compensated quantum well structures in excess of 20 quantum wells.

Zone Folding, Strain, and Doping

Although $\text{Si}_{1-x}\text{Ge}_x$ heterostructures and superlattices enhance certain electro-optical properties, no combination of these materials has yet resulted in a direct band gap

semiconductor. Another approach has been to investigate superlattices with alternating layers of pure silicon and germanium (Si_MGe_N) with the hope of developing a direct band gap material. Here, M and N represent the number of monolayers (ML) of Si and Ge respectively. In 1986, Bevk *et al.* demonstrated that ultra thin Si_MGe_N superlattices could be grown using MBE. These 4:4 structures alternated four monolayers of Ge with four monolayers of Si atop a Si substrate.

In 1989, Pearsall *et al.* concluded that if the period thickness of a superlattice is less than 20 ML, the band structure cannot be described by simply accounting for strain and confinement, one must also include the additional effects of Brillouin zone folding.^{33,34} Using these zone-folding techniques, the conduction band minima for the Si-Ge average bulk bands at 80% the distance to X would fold to the zone center by dividing the Brillouin zone by five. Thus superlattices with periods of 10, 20, or 30 are possible candidates for direct optical transitions.

Pearsall also successfully used a 1D Krönig-Penney model for determining the band structures of the quantum wells and zone folded superlattices. For wide barrier QW structures, the model gives solutions which are highly localized in the well regions. As the barrier layer thickness decreases, the states become progressively de-localized, and the electrons exist in low as well as high potential regions. In fact, if each layer of the superlattice is greater than 4 ML, such that the band structure of the layer can be defined by effective masses, the Krönig-Penney model appears to provide accurate results.

Detailed comparisons between effective mass and empirical pseudopotential calculations show that for superlattices with periods less than 4 ML, the Krönig-Penney model provides useful trends but should be considered cautiously.^{35,36} When the superlattice consists of alternate monolayers, the Krönig-Penney model reduces to the virtual crystal approximation which gives the band structure of most semiconductor alloys with an accuracy of about 10 percent.

Local density approximation (LDA) studies have shown that it is necessary to grow superlattice structures on a substrate buffer which has a lattice constant larger than pure silicon.^{37,38} Further work by Gell³⁹ has shown that direct band gap systems can only be achieved within a restricted range of buffer compositions which does not include the end-point composition $x=1$. Later, Gell proposed the concept of a buffer induced optical window for which holes and electrons are localized simultaneously within superlattice regions.⁴⁰ In each case, the direct gap structures Gell proposes are superlattices with a period of about 8 to 12 atomic ML containing biatomic sheets of Si (Si_2Ge_N , $6 \leq N \leq 10$). Such superlattices must be grown on Ge-rich buffers with about 60-90% Ge. The oscillator strength of the folded direct transitions in these $2:N$ structures is predicted to be about 10% of the strength characteristic of normal direct transitions.⁴¹ This is consistent with earlier estimates made by Gnuzmann and Clausecker.⁴² However, no one to date has been able to conclusively prove from empirical evidence that zone folding provides a direct energy band gap transition.

Electronic band structure and band alignment are also highly dependent on the strain within and between the epilayers of the superlattice.⁴³ In a symmetrically-strained superlattice, the composition and thicknesses of the two layers are adjusted so that (1) they are equally and oppositely strained, and (2) the strain energy of the pair of layers making any one period within the superlattice is minimum.⁴⁴ If one keeps the thicknesses of each individual layer of an ideal symmetrically-strained superlattice less than the critical thickness, h_c , then in principle, there is no limit to how thick one can grow the superlattice as a whole. In addition, very thick and stable superlattices can be fabricated without creating misfit dislocations by growing an alloy buffer layer with an average lattice constant. The method of designing and fabricating buffer layers has been discussed in detail by Kasper⁴⁵ and Herzog.⁴⁶

In 1990, strain symmeterized 6:4 superlattices were found to exhibit strong photoluminescence in the 0.7 to 0.9 eV range, indicative of a direct band gap.⁴⁷ However, these structures have a Type II band alignment, meaning that the photoluminescence is due to recombination near the Si-Ge interfaces. In addition, splitting the CB minimum due to strain was found to reduce the effective mass and improve electron mobility in a direction perpendicular to the interface by approximately 50% when Si-Ge strained epilayers were grown on (100) Si.⁴⁸ This improvement does not occur if the epilayer is grown on (111) Si. Fortunately, optical phonon frequencies appear to be very sensitive to the strain present in Si, Ge, and Si-Ge alloy layers. Frequency shifts due to strain provide a reliable and sensitive method for measuring the strain in commensurate lattice-mismatched layers and superlattices.

As in bulk semiconductors, impurities can significantly alter the optical and electrical properties of superlattices. The most interesting studies in recent years have involved two-dimensional doping, where impurities are confined to planes within the superlattice. This type of doping is known as δ -layer doping⁴⁹ and is normally confined to one or two monolayers of the superlattice. When the dopant is distributed over several mono-layers, this may be referred to as sharp-profile doping. For a heterogeneous structure, delta-layer or sharp-profile doping, either p - or n -type in each of one layer type is known as delta-doping. Another possible structure is n - i - p - i doping where alternating layers are either n -type/ i -type/ p -type/ i -type, or n -type/ p -type. All of these structures are also known simply as doping superlattices.

Esaki and Tsu⁵⁰ first proposed doping superlattices in 1970. Dohler^{51,52} first showed that n - i - p - i doping can create a space charge induced superlattice potential with unusual properties, including an indirect band gap in r -space (spatial separation of holes and electrons). This permits the electronic band structure of the doping superlattices to be

"tunable", along with long electron hole recombination times and significant optical nonlinearities.⁵³

For a Si-Ge superlattice on silicon, the conduction band minima are in the Si layers while the valence band maxima are in the Ge layers—the Type II staggered alignment mentioned in the previous section. Therefore, two types of doping superlattice are possible: (1) the Si layers are *n*-type doped and the Ge layers are *p*-type doped, and (2) the Si layers are *p*-type doped and Ge layers are *n*-type doped. In the first case, the Type II staggered band alignment is made even more staggered, which tends to reduce luminescence. In the second case, the doping tends to reverse the Type II alignment, resembling a Type I alignment with strong luminescent properties.

The electronic band structure calculations by Gallup and Fong⁵⁴ indicate that doped *n-i-p-i* Si-Ge superlattices may have direct band gaps as well as adjustable band alignments in *r*-space. In addition, these direct band gaps resulted from structures with superlattice periods other than ten, the direct band gap requirement from zone folding arguments. This implies that doping provides an important additional parameter for the electronic band gap engineering of ultra thin strained-layer superlattices. Their calculations show that band structure is sensitive to doping concentration, layer thickness, and doping layer location within the Si epilayer. Although no one has yet been able to reach the dopant concentrations necessary to convert the band alignment of a Si-Ge structure from Type II to Type I, evidence indicates it still may be possible to alter the alignment enough to reduce potential barriers and increase carrier tunneling through minibands resulting in more pronounced optical properties.

Donor and acceptor impurities also have a substantial effect on the optical properties of bulk semiconductor materials. Luminescence due to near-band-edge states, and effective mass theory have successfully described how shallow impurity-related bound states contribute to luminescence.⁵⁵ As one might expect, doped superlattices also have

shallow impurity bound states and effective mass theory has been adapted to describe these states.^{56,57} According to theory, near-band-edge impurity states depend upon the location of the impurity within the superlattice layers, layer (barrier) thicknesses, and band offsets (barrier heights).

Photoconduction and Resonant Tunneling

A photodetector is any device that measures photon flux by converting the energy of the absorbed photons into some measurable form. Photographic film is one type of photodetector. However, the two principal classes of photodetectors that convert optical power into an electrical signal are thermal detectors and photoelectric detectors. Thermal detectors convert photon energy into heat and are relatively slow as a result of the time required to change their temperature. Photoelectric detectors however are based on the photoeffect, in which the absorption of photons by some material results directly in an electronic transition to a higher energy level and generation of mobile charge carriers. Under the effect of an electric field these carriers move and produce a measurable electrical current or signal. The photoeffect may be external or internal. The external photoeffect involves photoelectric emission, in which photogenerated electrons escape from the material as free electrons. The internal photoeffect defines photoconductivity, where excited carriers remain within the material, and increase its conductivity.

When photons are absorbed by a semiconductor material, mobile charge carriers are generated in the form of an electron-hole pair for every absorbed photon. Therefore, the electrical conductivity of the material increases in proportion to the photon flux. An electric field applied to the material by an external voltage source causes the electrons and holes to be transported resulting in a measurable electric current.

A photodiode detector is a photoconducting semiconductor with a $p-n$ junction whose reverse current increases when it absorbs photons. A reverse-biased $p-n$ junction

under illumination is shown in Figure 3. Photons are absorbed in every region of the device and an electron-hole pair is generated. However, charge carriers are transported in a particular direction only where an electric field is present. Since a $p-n$ junction can support an electric field only in the depletion layer, this is the best region to generate photo-carriers. Electrons and holes generated in the depletion layer quickly drift in opposite directions under the influence of the electric field. Since the field points in the $n-p$ direction, electrons move to the n side and holes to the p side. As a result, the photocurrent created in the external circuit is always in the reverse direction from the n to the p region.

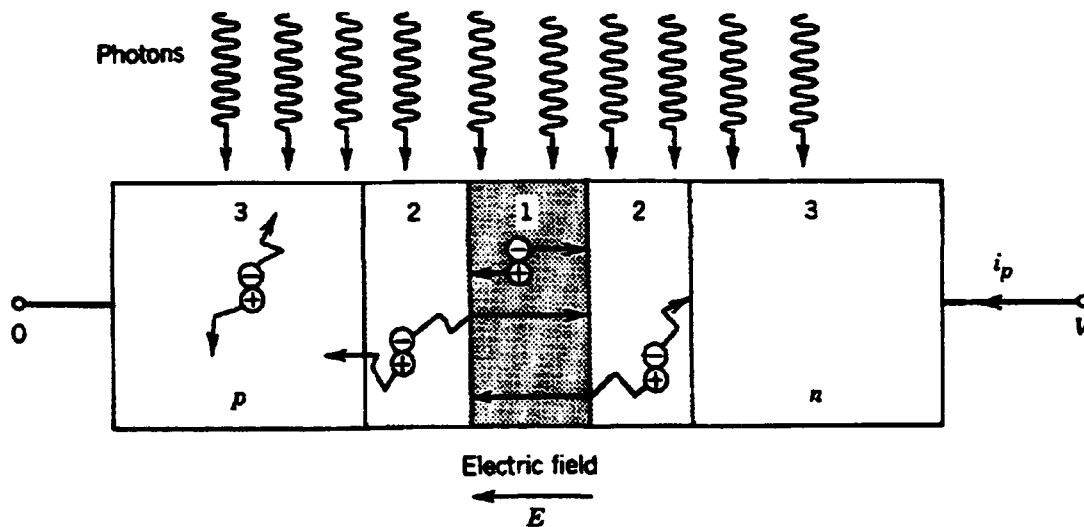


Figure 3. An ideal reverse-biased $p-n$ photodiode detector.⁵⁸

Electrons and holes generated next to the depletion layer enter the depletion layer by random diffusion. An electron coming from the p side is quickly transported across the junction and contributes a charge to the external circuit. A hole coming from the n side has a similar effect. Electrons and holes created far away from the depletion layer cannot be transported because no electric field is present. They wander randomly until they are annihilated by recombination and do not contribute a signal to the external electric current.

A $p-i-n$ photodiode has several advantages over the $p-n$ photodiode. The intrinsic (usually lightly doped) layer sandwiched between the p and n layers extends the width of the region supporting the electric field, in effect, widening the depletion region. A wider depletion region increases the area available to absorb light and transport charge. Increasing the depletion width also reduces the junction capacitance, which reduces the RC time constant.

Although $p-n$ and $p-i-n$ photodiodes are generally faster than photoconductors, they do not exhibit gain. In an avalanche photodiode (APD), however, each detected photon is converted into a cascade of moving carrier pairs. Weak light can then produce a current that is sufficiently amplified to be registered by the electronics following the APD. An APD is a strongly reverse-biased photodiode in which the junction electric field is large; the charge carriers therefore accelerate and acquire sufficient energy to excite new carriers by impact ionization. A simple schematic of this process is shown in Figure 4.

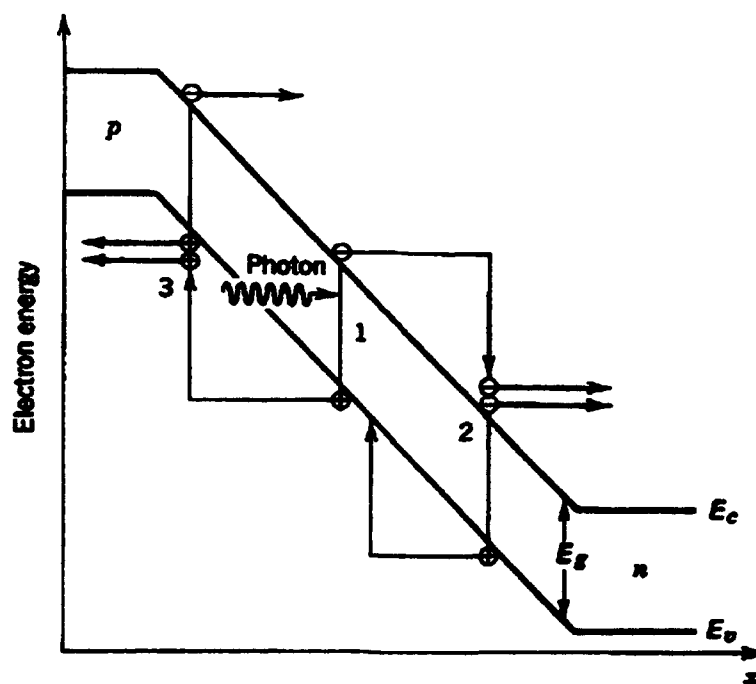


Figure 4. Energy band schematic of avalanche multiplication.⁵⁸

Although the detected signal from an APD is stronger, the avalanche multiplication (or gain) creates extra noise which must be added to the shot noise of incident photons and the circuit noise. This excess noise comes from the fluctuations of the avalanche gain and occurs in two directions across the APD since holes and electrons travel in opposite directions. If both electrons and holes undergo impact ionization at the same rate, the avalanche gain is equally strong in both directions and the excess noise may become very large. However, if only one carrier ionizes, the avalanche proceeds in only one direction and excess noise is minimized. Therefore, to limit the excess noise caused by avalanche multiplication, holes and electrons must ionize at vastly different rates.

In intrinsic silicon, the ratio of these ionization coefficients, κ , is greater than 20:1 (electrons:holes) so there is little avalanche noise.⁵⁹ This ratio may also be expressed in terms of α/β where α corresponds to electrons and β to holes. By themselves, α and β represent ionization probabilities per unit length (rates of ionization, cm^{-1}); the inverse coefficients, $1/\alpha$ and $1/\beta$, represent the average distances between consecutive ionizations. The ionization coefficients increase with the depletion-layer electric field (since it provides the acceleration) and decrease with increasing device temperature. The latter case occurs because increasing temperature causes an increase in the frequency of collisions which lowers the opportunity a carrier has of gaining sufficient energy to ionize. In most simple models, α and β are assumed to be constants that are independent of position and carrier history.

When only electrons ionize appreciably ($\alpha \gg \beta$, or $\kappa \rightarrow \infty$), then the avalanching process proceeds principally from left to right. When all the electrons arrive at the n side of the depletion layer, the process terminates. However, if electrons and holes both ionize appreciably ($\alpha \approx \beta$, or $\kappa \approx 1$), then those holes moving to the left create electrons that move to the right, which, in turn, creates more holes moving to the left. Although this process

increases the gain of the device, it is undesirable for several reasons: (1) it is time consuming which reduces the device bandwidth, (2) it is random and increases device noise, and (3) it can be very unstable, which may cause an avalanche breakdown.

Therefore, one wants to design an APD from a material that permits only one type of carrier (either electrons or holes) to impact ionize. If electrons have the higher ionization coefficient for example, the best results are obtained by injecting the electron of a photocarrier pair at the p edge of the depletion layer and by using a material whose value of κ is as large as possible. If holes are injected, the hole of a photocarrier pair should be injected at the n edge of the depletion layer and κ should be as small as possible. The ideal case of single-carrier multiplication is achieved when $\kappa=\infty$ or $\kappa=0$.

Using band gap engineering, one can artificially tailor the band structure of the semiconductor to significantly alter the ratio of these ionization coefficients to increase gain and reduce excess noise. The superlattice APD shown in Figure 5(a) alternates

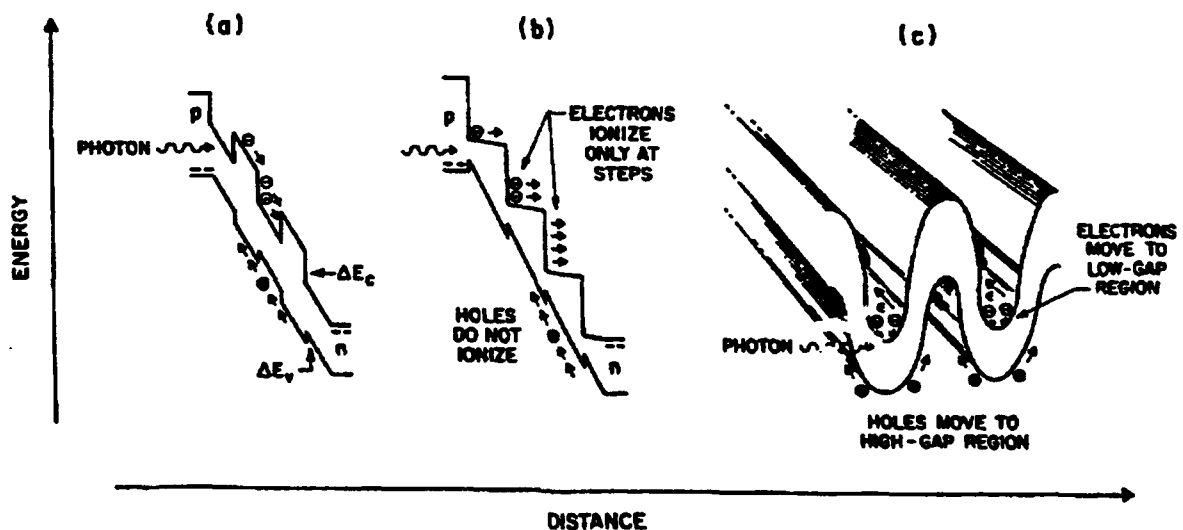


Figure 5. Avalanche photodiodes designs using band gap engineering: (a) MQW APD, (b) solid-state PMT APD, and (c) channeling APD.⁶⁰

layers of high- and low-gap materials restricting ionizing collisions to the low-gap regions. Carriers then accelerate and gain energy but do not ionize in the wide-gap regions. After entering the next well, a free electron gains enough energy from the CB discontinuity ΔE_C to ionize. The VB discontinuity, ΔE_V , however, is not as large yet supplies a similar acceleration to holes. When $\Delta E_C > \Delta E_V$, electrons enter the well with higher kinetic energy and ionize more efficiently than holes. This concept, first demonstrated by Capasso *et al.* increased α/β by a factor of 3 to 4 in a GaAs device.

The staircase APD shown in (b) uses a superlattice of layers that are graded from low gap to high gap. Here, the band gap widens gradually in each layer but narrows abruptly at the layer interface. As in (a), the band gap difference is more obvious in the CB where the discontinuities form steps, then, as a reverse bias is applied, the sawtooth band diagram resembles a staircase. A free electron drifts toward the right in the graded layer but cannot ionize since the field is too low. However, the discontinuity itself provides enough energy for an electron to ionize, therefore, ionizing collisions occur only at the steps. Since the VB steps are the wrong sign and the electric field too small, holes do not ionize in this structure as they drift from right to left.

In several ways the staircase APD is like a standard photomultiplier (PMT) which is a photoemissive, high internal gain device with relatively low noise. As in a PMT, the negligible avalanche noise of the staircase APD can be attributed to not only the lack of feedback by ionizing holes but also from electrons ionizing at well-defined locations. In this way, the CB steps, are similar to PMT dynodes which minimize the intrinsic randomness of the gain.

Another device, the channeling APD (c) consists of an alternating *p*- and *n*-layers of different band gap, with lateral *p*- and *n*-contacts.⁶¹ Here, the 3D energy band diagram resembles two gutters separated vertically by the band gap. Channels formed by the *p*-*n* junction run parallel to the layers. A periodic, transverse electric field (perpendicular to

the layers) results from the alternated $n-p-n-p$ layers, while an external field is applied parallel to the layers. The transverse field collects electrons in the low-gap n -layers, where they are channeled by the parallel electric field, so electrons impact ionize in the low-gap n -layers. But the transverse field also causes holes created by electrons ionizing in the n -layers to transfer into the wide-gap p -layers before ionizing. Once there, holes cannot impact ionize, because the band gap is too high to permit multiplication. The α/β ratio of this device is therefore, very high and avalanche noise very small. It has been demonstrated⁶² that channeling devices can totally deplete charge carriers from a large volume of semiconductor material, regardless of the doping level.

Quantum resonance, or resonant tunneling occurs when the energy of an injected carrier is equal to the energy of one of the energy levels in the potential well allowing the carrier to penetrate (or tunnel) through a barrier. Figure 6 shows how tunneling occurs with an applied d-c bias. Electrons originate near the Fermi level to the left of the first barrier and tunnel through the well. Tsu and Esaki⁶³ computed the resonant transmission coefficient as a function of electron energy for multi-barrier structures from the tunneling point of view, leading to the derivation of current-voltage characteristics.

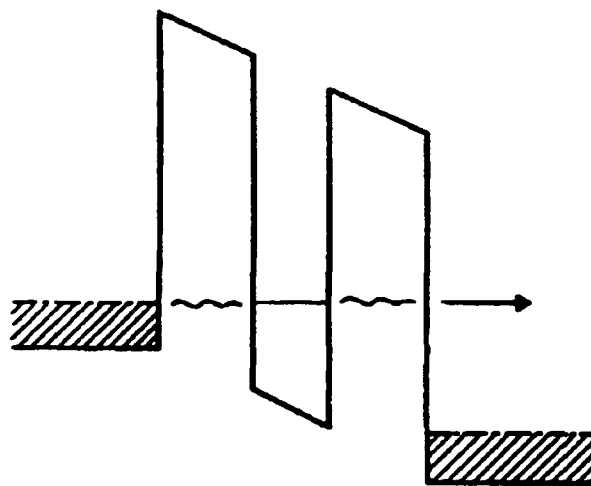


Figure 6. A resonant tunneling quantum well.⁶⁴

A superlattice using resonant tunneling can also act as an effective mass filter. Since the tunneling probability increases exponentially with decreasing effective mass, electrons are transported through the superlattice more readily than the heavier holes as long as the valence band discontinuity is not negligible compared to the conduction-band discontinuity (refer to Figure 7). Effective mass filtering is the basis of tunnel photoconductivity. In a classic photoconductor, photogenerated electrons and the electrons injected from Ohmic contacts can be viewed as moving through the semiconductor and around the circuit until they recombine with the slowly moving photogenerated holes. This produces a current gain whose value is given by the ratio of electron-hole pair lifetime to the electron transit time.

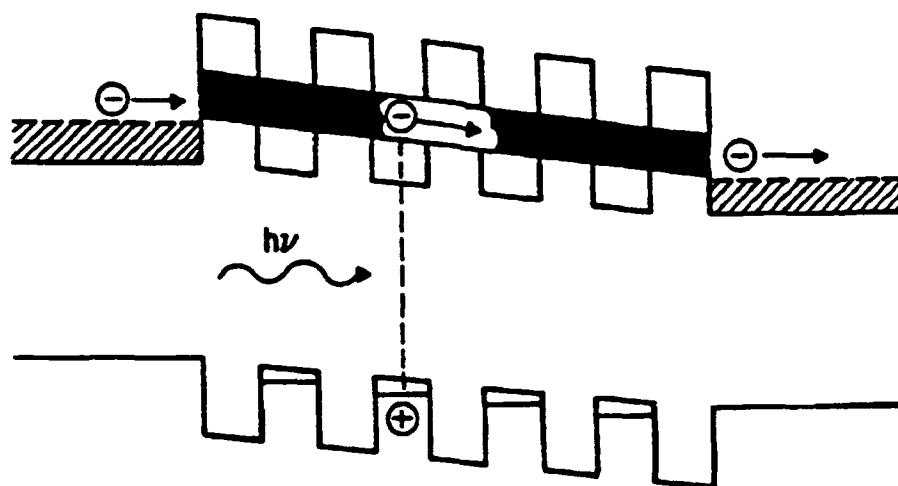


Figure 7. Effective mass filtering in a superlattice photoconductor.⁶⁵

In a superlattice, however, photogenerated heavy holes tend to remain localized in wells as a result of their negligible tunneling probability. Electron states tend to be extended because of the small electron effective mass ($\approx 1/10$ of the heavy hole mass) and ultra thin barriers. These extended states form a miniband and the photoelectrons are transported by band-type conduction. Since carrier mobility in the miniband depends

exponentially on the superlattice barrier thickness, the electron transit time, and the photoconductive gain-bandwidth product can be artificially tuned over a wide range. This offers intriguing versatility which is not available in a standard photoconductor. High-performance infrared photoconductors that use effective mass filtering were first demonstrated by Capasso.⁶⁶

Detector Characterization

An ideal imaging detector has a peak response at a desired wavelength, high detectivity, operates at a moderate temperature, and is easily fabricated over large, uniform arrays. For example, low background applications such as satellite-based astronomy or space surveillance requires detectivities in excess of 10^{13} cm $\sqrt{\text{Hz/W}}$ with minimum operating temperatures fixed by the size/power of the cryocooler.⁶⁷ In the past ten years, there has been considerable interest in applying multiple quantum well structures as IR detectors since the effective band gap of these structures may be tuned to respond at a desired wavelength and designed to minimize noise. However, most work to date has been with III-V materials exhibiting intersubband absorption of electrons.^{68,69} GaAs/AlGaAs multiple quantum well detector arrays with hybrid Si signal processing electronics have also been fabricated and characterized.^{70,71} Yet, despite the promise III-V materials offer, Si-based infrared detectors present the added potential advantage of monolithic integration with mature Si signal processing electronics for a fast, sensitive, high-resolution focal plane arrays.

Fabricating a quantum well detector requires a considerable amount of design before growing the crystal. One normally wants a quantum well structure with a single bound state and an excited state near the barrier for design and modeling purposes. The position of the bound and extended states as a function of the well width can be calculated using the effective mass approximation. To fabricate a device, one needs to select a

substrate, a buffer composition, a specific superlattice structure, a capping layer, doping concentrations, circuit design, and growth and etching processes. Finally, one has to confirm the device's physical properties and characterize its optical properties. X-ray diffraction and TEM are popular diagnostics to examine device structure. FTIR is often used to determine optical absorption. However, to begin to evaluate a device's worth as a detector, one needs to measure its responsivity as a function of wavelength, dark current as a function of bias voltage, and spectral noise density.

Responsivity relates the electric current flowing in a device to the incident optical power. For example, if every photon incident on a device were to create a single photoelectron with unit gain, a photon flux ϕ (photons per second) would produce an electron flux corresponding to an electric current $i_p = e\phi G$, where e is elemental electron charge and the gain, $G=1$. Optical power, $P = h\nu\phi$ (Watts) at frequency, ν , would then cause an electric current $i_p = eP/h\nu$. Since the fraction of photons producing detected photoelectrons is η rather than unity, then the electric current could be described as

$$i_p = \eta e\phi = \eta eP/h\nu = \mathfrak{R}P .$$

The proportionality factor \mathfrak{R} , between the electric current and the optical power, is defined as the responsivity of the detector and has units of Amperes/Watt. Note that \mathfrak{R} increases with wavelength λ since photoeffect detectors are responsive to photon flux rather than to optical power. As λ increases, a given optical power is carried by more photons, which in turn, produces more electrons. The region over which \mathfrak{R} increases with λ is limited, however, since the wavelength dependence of η affects both short and long wavelengths.

To directly measure \mathfrak{R} , one normally illuminates the detector with a calibrated, blackbody IR source located as close as possible to the detector. The source emission is

chopped for background subtraction and spectrally filtered through a specific range with a bandwidth that provides acceptable resolution. The detected signal current is measured per unit incident power. The spectral incident power is calculated from the temperature of the blackbody and its distance from the detector. The measured responsivity is corrected by allowing for dispersion grating response, and losses through optical transmission windows and collection optics. In a first-order approximation, reflection losses, polarization factors, or other intrinsic design factors are normally not accounted for. Finally, the responsivity is plotted as a function of wavelength to determine peak response, then repeated as a function of device temperature.

Dark current measurements are even more straightforward considering no light source is required. In fact, since objects at room temperature emit copious amounts of infrared radiation, the sample and collection optics need to be carefully shielded to eliminate background noise. A voltage is applied across the detector and the dark current density (A/cm^2) is measured as a function of bias voltage. If more than one detector is etched onto a chip, then one should compare the dark currents from a number of different size detector areas to determine if there is any leakage current from the side walls of the superlattice mesas. Finally, one would repeat this procedure as a function of detector temperature.

Spectral noise density is a measure of the average total noise due to frequency components between f and $f+\Delta f$, the electrical bandwidth. Spectral noise includes the effects of shot noise (photon and photoelectron), excess noise (from the avalanche process in an APD), and Johnson noise. Very low spectral noise is difficult to measure using room-temperature electronics; therefore, a load resistor is used in parallel with the quantum well detector on the cold finger in the Dewar. The output signal is sent through a pre-amp, then to a spectrum analyzer for analysis. The Johnson noise of the load resistor is calculated and this value sets the minimum measurable noise depending on load

resistance. The total range of noise measurement will be limited by $1/f$ noise at the low end and RC roll off at higher frequencies. RC roll off can be determined by the parallel resistance of the sample and load resistor, and the capacitance of the cabling. Amplifier noise is subtracted from the measured noise using a simple model of an equivalent circuit. Spectral noise ($A/\sqrt{\text{Hz}}$) as a function of dark current (A) is plotted. The detectivity of the sample is then computed using the measured values of responsivity and spectral noise.

To increase the detectivity of a quantum well IR detector, it is necessary to lower the dark current and spectral noise of the detector. To do this we must fully characterize the low-temperature performance of the device and understand the nature and origin of noise in a quantum well detector. Dark current appears to consist of resonant tunneling and thermionic emission current. At low temperatures, resonant tunneling contributes the most to total current noise, switching to thermionic emission of confined carriers from the quantum well as temperature increases. Since thermionic emission dominates dark current noise at high temperatures, thermionic current should be kept as low as possible to increase the maximum operating temperature of the detector.

To lower the tunneling current noise, one can either increase the barrier width or increase the barrier height. To lower the thermionic current, one must increase the barrier height. However, increasing barrier height also changes the absorption wavelength. Therefore, to decrease resonant tunneling and thermionic emission while simultaneously keeping wavelength fixed is to increase barrier width. In GaAs detectors, calculations have shown a decrease of approximately two orders of magnitude in the tunneling current when the barrier width is increased from 300 to 400 Å.⁷² Rosenbluth *et al.* have also analyzed the case of using a single, thick blocking quantum barrier in a 50 quantum well superlattice and found only a slight decrease in the dark current. The reason for this may be that for a given applied bias, a larger potential is dropped over the single, wide barrier than the smaller ones, increasing its dark current value close to the case of a structure

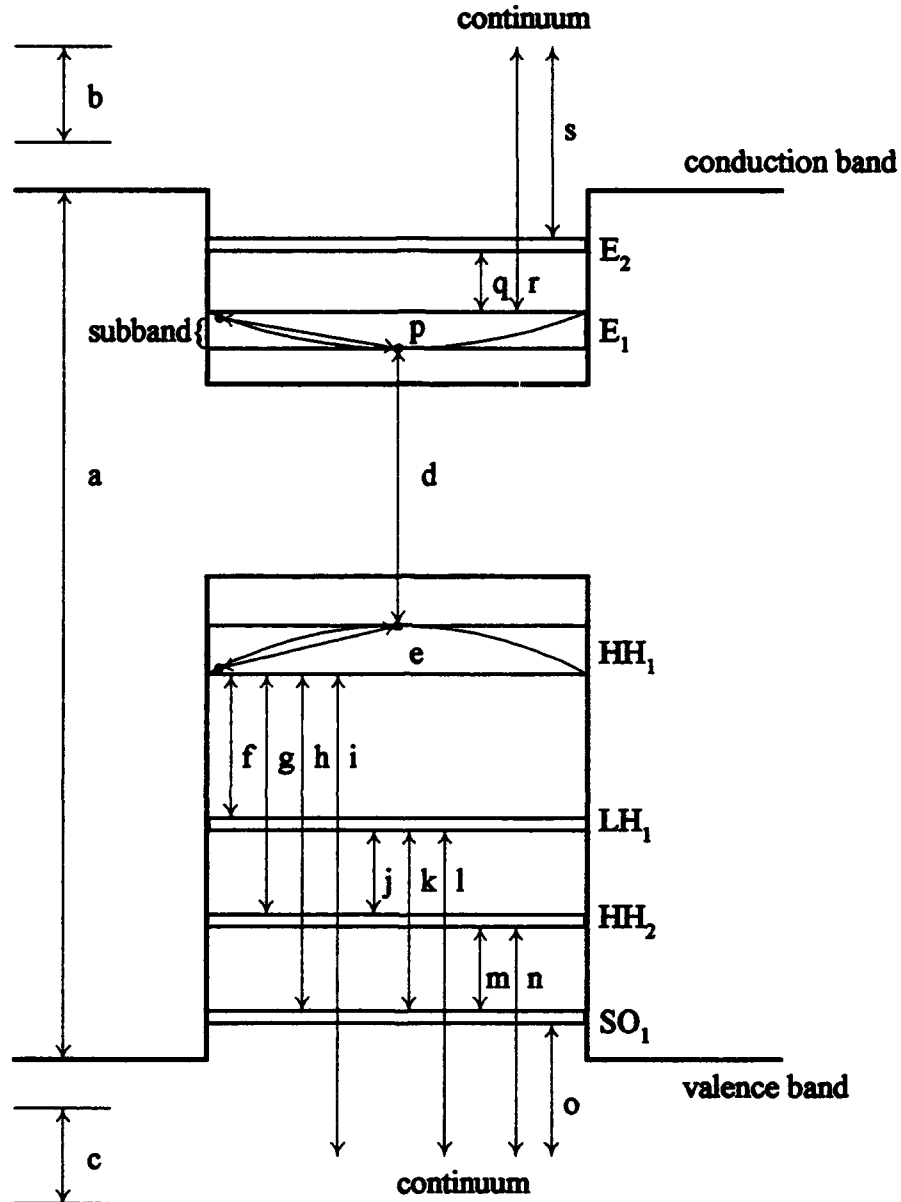
without a large blocking layer. They later determined that increasing all of the barriers uniformly provided the lowest dark current resulting in the highest detectivity.

In order to better understand the fundamental photoresponse of a detector, one must examine the transitions which occur between minibands within a quantum well and those across the bandgap. The next section provides definitions for these transitions and a discusses the quantum mechanic selection rules for various absorption processes.

Advanced Treatment of Optical Absorption in SiGe Superlattices.

Transition Definitions, Selection Rules, and the Mass Tensor. Allowed optical transitions can be split into two categories: *interband* transitions which occur *between* bands and subbands originating from different extrema, and *intra*band transitions which occur *within* bands and subbands and which involve the dipole matrix elements between envelope functions. At this point, it is very important to provide clear and rigorous definitions for these transitions occurring across the band gap and within band wells. Although these terms are relatively simple, they still cause a great deal of confusion when one first begins to read advanced publications since their meanings and energy transition behavior can be quite subtle. Most confusion arises from the various combinations of the terms "intra" (meaning literally, "within") and "inter" (meaning "between") with the terms "band" and "subband".

Referring to Figure 8, an *interband* transition occurs across the energy gap *between* the conduction band (CB) and the valence band (VB) as in transitions (a) and (d). This definition holds, if the transition occurs between a CB minima and VB maxima, such as the indirect transition in elemental Si, or from one subband to another—as long as the band-to-band transition is *across the gap*. If the transition occurs between a CB subband and a VB subband, as in transition (d), the transition may also be called an *interband-*



where:

a	interband
d	interband-intersubband
g and q	intersubband (or intraband-intersubband)
f, h, j, k, and m	intervalence-subband
b, c, i, l, n, o, r, and s	intraband to continuum energy level
e and p	intrasubband (free carrier)

Figure 8. Illustration of various transitions in a quantum well structure.

intersubband transition since the transition occurs between two bands and between two subbands. There are seven more interband-intersubband transitions possible in Figure 8 from HH1 to E2, LH1-E1 and E2, etc., which are not shown. Also note, this figure is a schematic diagram used to illustrate transition names only—the width of the minibands would actually increase with energy in a quantum well.

An *intersubband* transition occurs *between* any two subbands of the same effective mass *within* the same band, such as HH1 \leftrightarrow HH2, LH1 \leftrightarrow LH2, E1 \leftrightarrow E2, and so on, as in transitions (g) and (q). Since intersubband transitions occur *within a band*, and *between subbands*, these transitions are also sometimes called *intra-band-intersubband* transitions.

An *intervalence-subband* transition may occur between *any* two subbands with different effective masses within the valence band, as in transitions (f), (h), (j), (k), and (m). Intervalence-subband transitions have been recently⁷³ attributed to the anisotropy of the Hamiltonian and strong *s*- and *p*-state mixing when germanium compositions exceed $x=0.30$. As Ge composition increases, the bandgap of the Si_{1-x}Ge_x alloy decreases at the Γ -point resulting in large coupling between conduction and valence bands at $k\neq 0$. In this case, the *s*-like conduction bands mix with the *p*-like valence bands resulting in optical transitions between Bloch states of the valence subbands.

An *intra-band* transition occurs within the conduction or valence bands, but not from subband to subband. These transitions occur in free-to-extended state transitions shown in (b) and (c), and bound-to-free transitions shown in (i), (l), (n), (o), (r), and (s). *Intra-subband* transitions occur within a subband, as in transitions (e) and (p), and may be considered as a two-dimensional analog of free-carrier absorption.

A "free carrier" is a charge carrier (electron or hole) which is free to move within a band as shown in Figure 9. Free-carrier absorption is characterized by a relatively featureless absorption spectrum which increases as a function of the photon wavelength. To absorb a photon, the carrier makes a transition to a higher energy state within the band.

Such a transition requires an additional interaction to conserve momentum. The change in momentum can be provided by a phonon interaction with the lattice or by scattering from ionized impurities.

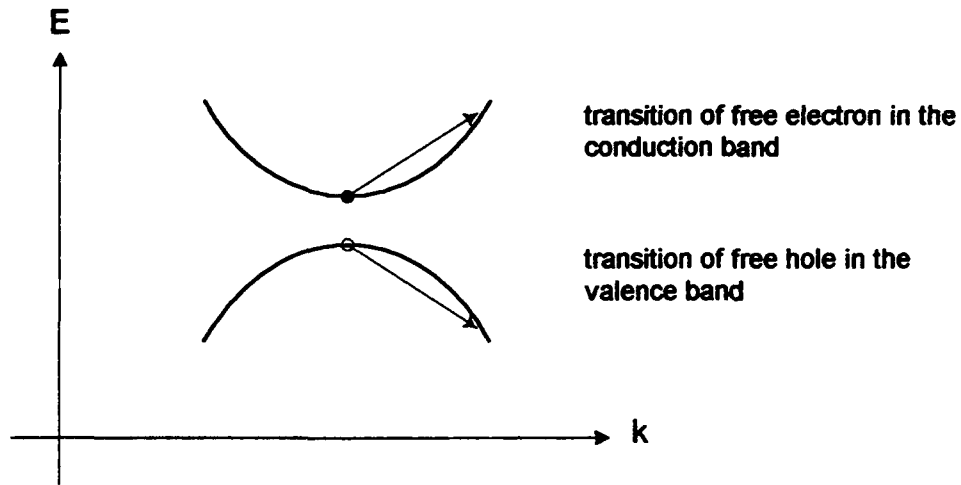


Figure 9. Illustration of free-carrier absorption transitions within the conduction and valence bands.

The classical formula for free-carrier absorption α_f is

$$\alpha_f = \frac{Nq^2 \lambda^2}{8\pi^2 m^* \eta c^3 \tau}$$

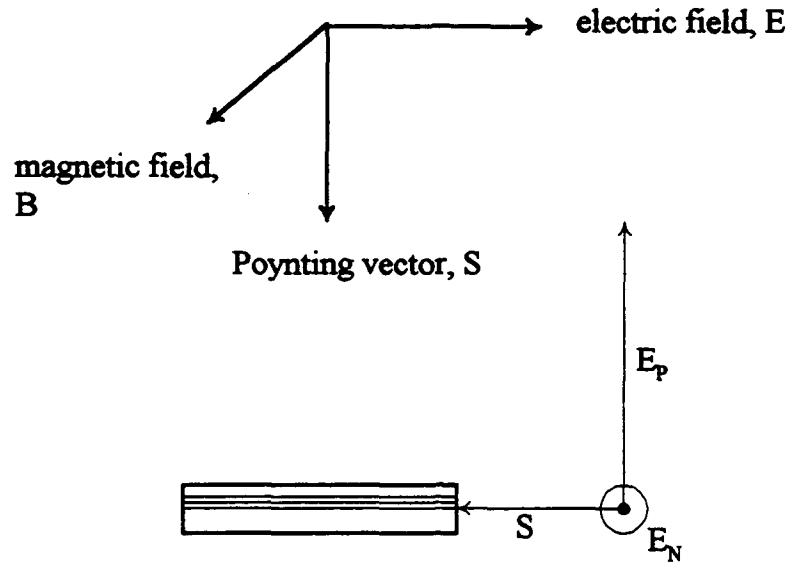
where N is the carrier concentration, q is the free-carrier charge, λ is the photon wavelength, m^* is the carrier effective mass, η is the index of refraction, c is the speed of light, and τ is the relaxation time. The relaxation time reflects the influence of scattering from phonons and impurities. For perfect heterostructures, free carrier absorption is forbidden since it is impossible to conserve energy and momentum simultaneously during the photon absorption by the free carrier. However, in imperfect heterostructures, free-carrier absorption may be induced by defects and impurities, resulting in phonons which

are capable of providing the energy and momentum necessary for the carrier transition.

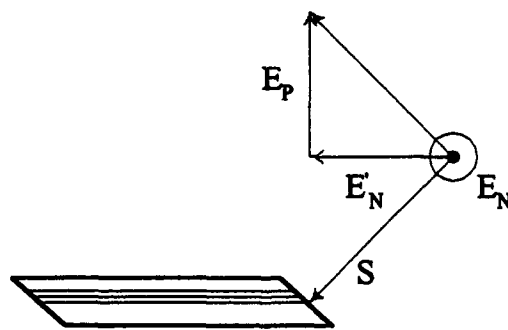
In detector applications, normal-incidence light is defined as radiation propagating parallel to the growth direction of the crystal wafer. In this orientation, the Poynting vector, \vec{S} , of the propagating wave is directed normal to the wafer surface, while the magnetic field, \vec{B} , and electric field, \vec{E} , lies parallel to the growth epilayer, or on the quantum well plane, as seen in Figure 10. If light enters the side of the sample specimen, a polarizer may be used to rotate the electric field perpendicular to the quantum plane, \vec{E}_p , as in Figure 10(a) allowing us to study how selection rules and the subsequent strength of various energy transitions are affected as a function of polarization. Facets cut 45° along the sides of the sample efficiently couple light into the high-index material which now acts as a waveguide undergoing multiple internal reflections. In this configuration, the "active" region of multiple quantum wells grown in ultra thin epilayers near the top surface are properly sampled as the light reflects from the top surface. Creating a waveguide of the sample material; therefore, has two important features: first and foremost, given the sample geometry, it is the only possible way to provide some means of rotating the polarized electric field vector out of the growth plane; and second, the waveguide geometry causes multiple internal reflections allowing for several "passes" through the active region which increases the absorption signal strength. Note, however, that six passes through the quantum plane will not necessarily increase signal strength six-fold: reflection losses at the top and bottom surfaces of the wafer reduce signal intensity by an estimated 20-30% per "bounce" from each surface.

In Figure 11(a), a single quantum plane is illustrated next to a faceted waveguide and both normal and perpendicular polarization vectors. The growth axis is depicted along the z direction. All three possible directions for electron motion in r-space are

orientation of normal incidence
light in a detector application



(a)



(b)

Figure 10. The (a) waveguide geometry with no facets, and (b) waveguide with 45 degree facets and original E_p decomposed to perpendicular and normal components.

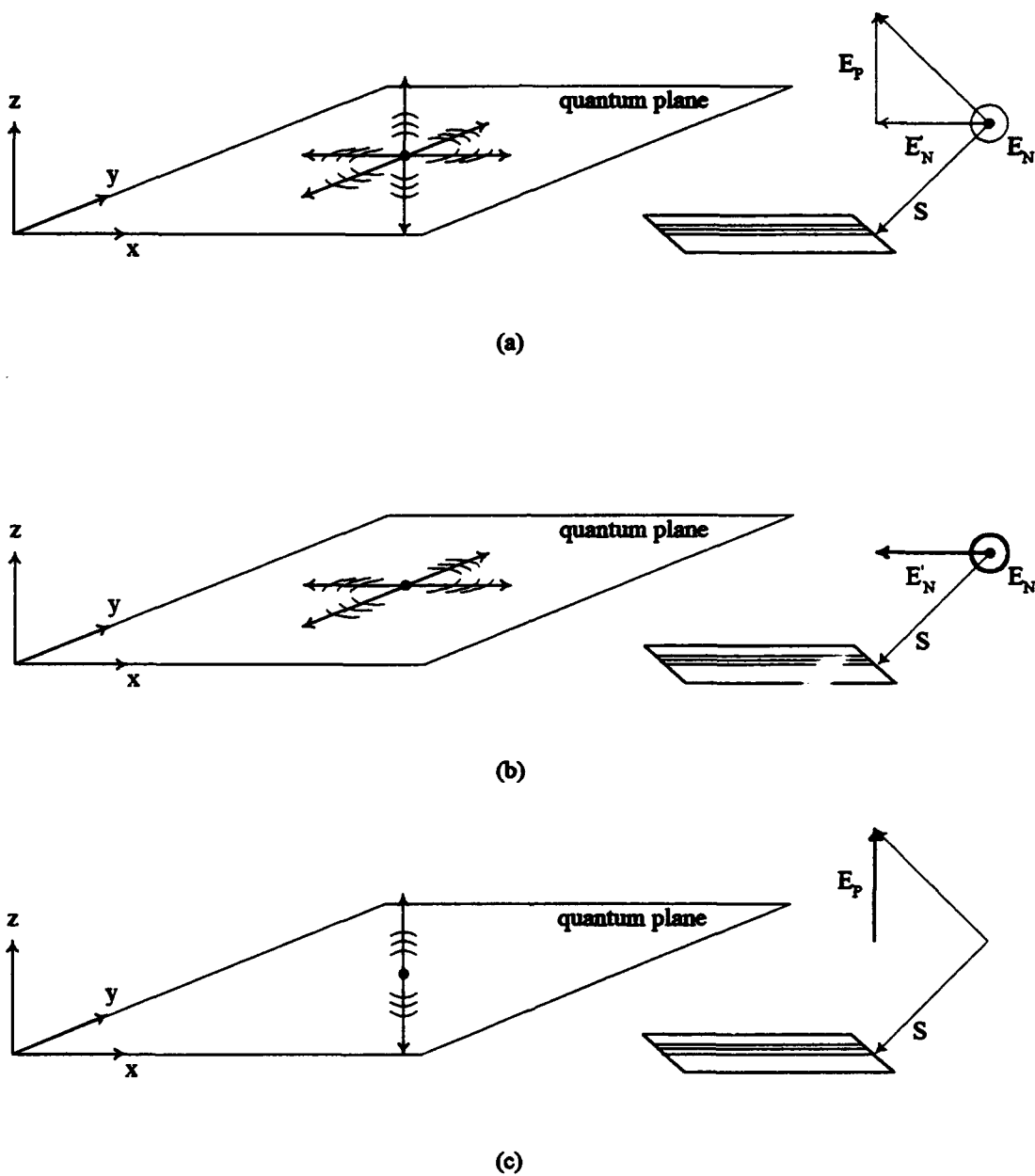


Figure 11. Electric dipole oscillations relative to the quantum well plane in r -space with respect to incident polarized light: (a) parallel and normal components of incident light, (b) normal components only, and (c) parallel component only.

shown in (a): two on the plane and one along the growth axis. In Figure 11(b), the effects of only normal incidence light as in a typical detector application is shown where an induced electric dipole oscillation is limited to that lying on the quantum plane. The vector component \vec{E}_p has no bearing in this scenario since it is impossible for an electric field perpendicular to the plane to induce a dipole in the x-y plane. The two normal components, \vec{E}_N and \vec{E}'_N , however, may induce an electric dipole in the plane.

In Figure 11(c), the electron is limited to a dipole oscillation normal to the quantum plane along the growth direction and $\vec{k}_\parallel = \vec{k}_x, \vec{k}_y$ is conserved. Clearly, the z-dipole may be induced by \vec{E}_p ; however, even \vec{E}_N and \vec{E}'_N may impart momentum normal to the quantum plane when the electron effective mass tensor has off-diagonal elements. Referring to Figure 12, the effective mass is defined as:

$$m^* = \frac{\hbar^2}{d^2 \epsilon / dk^2} .$$

Then, for three dimensions

$$\frac{1}{m^*} = \frac{1}{\hbar^2} \nabla_k (\nabla_k \epsilon) ,$$

or

$$\frac{1}{m_{\alpha\beta}^*} = \frac{1}{\hbar^2} \frac{\partial^2 \epsilon}{\partial k_\alpha \partial k_\beta} . \quad (4)$$

The second-order tensor is required since the curvature of a generalized $\epsilon(k)$ relation may vary along all possible directions in k-space. The left hand side of this general expression for effective mass may be expanded in the following manner:

$$\frac{1}{m_{\alpha\beta}^*} = \begin{vmatrix} \frac{1}{m_{xx}^*} & \frac{1}{m_{xy}^*} & \frac{1}{m_{xz}^*} \\ \frac{1}{m_{yx}^*} & \frac{1}{m_{yy}^*} & \frac{1}{m_{yz}^*} \\ \frac{1}{m_{zx}^*} & \frac{1}{m_{zy}^*} & \frac{1}{m_{zz}^*} \end{vmatrix} .$$

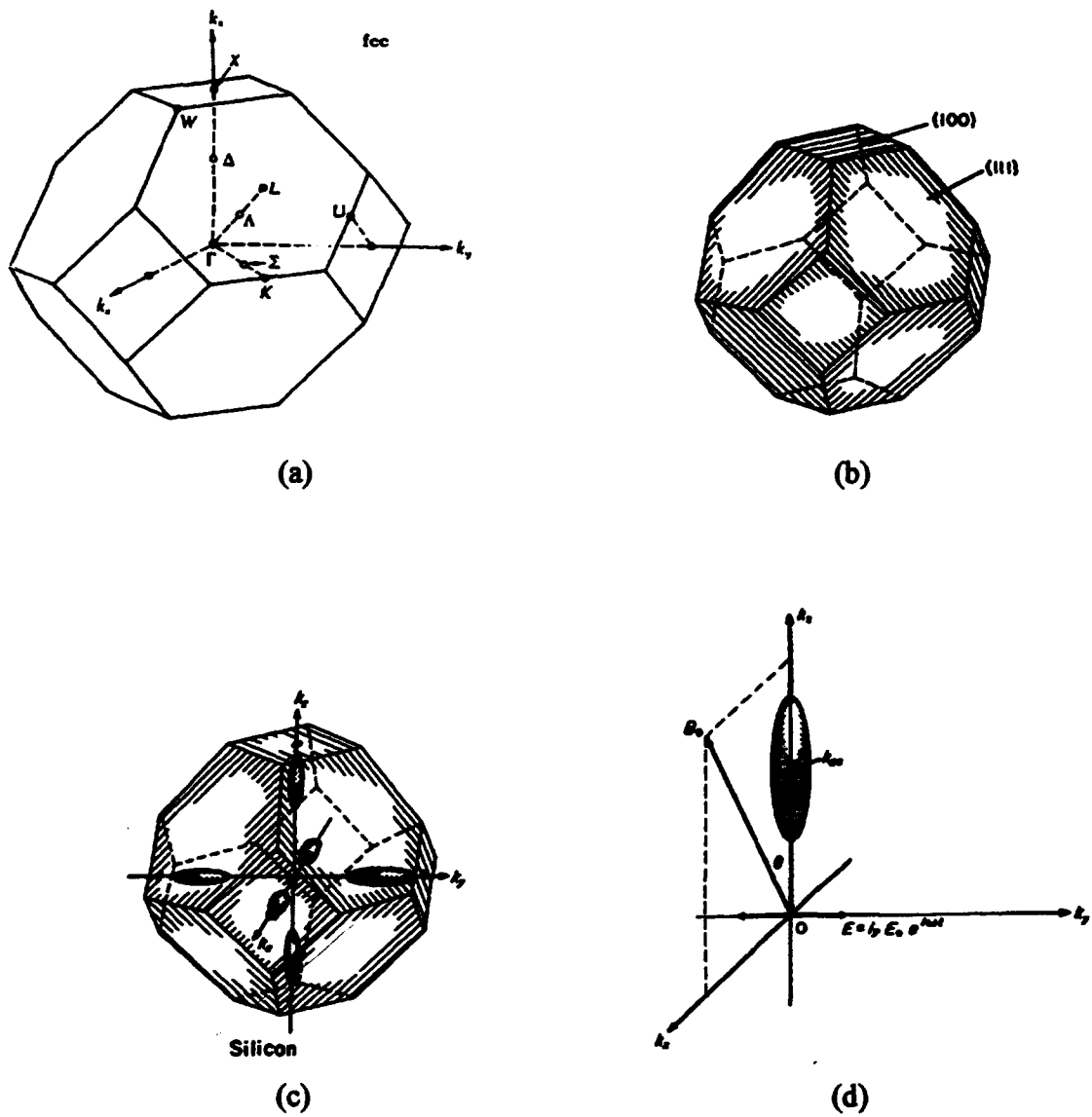


Figure 12. The (a) coordinate system , and (b) surface planes of the first Brillouin zone of a face-centered cubic structure in k -space. Figures (c) and (d) illustrate the coordinate system and the ellipsoid constant-energy electron surface.⁷⁴

Evaluating the right-hand side of Eq(4) for an ellipsoidal energy surface defined along the principal axes yields

$$\varepsilon - \varepsilon_c = \hbar^2 \left[\frac{k_x^2 + k_y^2}{2m_i^*} + \frac{(k_x^2 - k_{z0}^2)^2}{2m_i^*} \right],$$

then

$$\frac{\partial^2 \varepsilon}{\partial k_\alpha \partial k_\beta} = 0 \quad \forall \quad \alpha \neq \beta,$$

i.e., all off-diagonal elements of the tensor are zero, leaving

$$\frac{1}{m_{xx}^*} = \frac{1}{m_{yy}^*} = \frac{1}{m_i^*}$$

and

$$\frac{1}{m_{zz}^*} = \frac{1}{m_i^*}$$

where

$$\frac{1}{m_{\alpha\beta}^*} = 0 \quad \forall \quad \alpha \neq \beta.$$

Collecting terms,

$$\frac{1}{m_{\alpha\beta}^*} = \begin{vmatrix} \frac{1}{m_i^*} & 0 & 0 \\ 0 & \frac{1}{m_i^*} & 0 \\ 0 & 0 & \frac{1}{m_i^*} \\ \dots & & \dots \end{vmatrix}.$$

When the coordinate axes are defined to lie along the principal axes of the ellipsoidal constant-energy surfaces, the subsequent mass tensor has no off-diagonal terms. The remaining diagonal terms allow electron motion along the growth direction induced by \vec{E}_p , which lies perpendicular to the quantum well plane (or parallel to the growth direction). Off-diagonal terms allow similar electron motion induced by \vec{E}_n , or normal incidence light. Since there are no off-diagonal terms in the mass tensor, there can be no intersubband

transitions from normal-incidence light on (100) Si. However, normal incidence light may induce intersubband transitions on (110) and (111) Si substrates since non-zero terms do exist in the effective mass tensor at these crystal orientations.

The preceding argument is appropriate when considering electronic transitions in the CB of n -type $\text{Si}_{1-x}\text{Ge}_x$ material systems. However, the constant-energy surfaces of holes in the VB resemble a paraboloid centered at the origin of the coordinate axes. These concentric paraboloids map out the constant energy surfaces of the heavy-hole, light-hole, and split-off states and are coupled via strong mixing from off-diagonal elements in the Luttinger Hamiltonian as derived by Ikonik.⁷⁵ A derivation of the quantum mechanical selection rules for valence band transitions for (100), (110), and (111) Si substrates is provided in Chapter IV.

Early Interband Detectors. Although there have been many studies in SiGe superlattice growth and photoemission during the past 15 years; there have been relatively few reports of detailed absorption measurements and photodetector fabrication. The first SiGe photodetector was a single-crystal Ge p - i - n structure grown on a Si substrate by Luryi *et al.*⁸ at AT&T Bell Laboratories in September, 1984. This simple device had a photoresponse spectra typical of a Ge detector out to 1.55 μm with quantum efficiencies up to 41% for incident light up to 1.45 μm at 300 K. However, the silicon and germanium materials were grown incommensurate at the interface resulting in relatively high reverse-bias dark current caused by threading dislocations at the substrate-buffer layer which propagated through the Ge p - i - n junction.

Kastalsky *et al.* significantly improved a similar Si-Ge heterojunction device by "glitch-grading" the alloy transition region.⁷⁶ This growth technique involved repeatedly lowering the Ge content from 100% to 70% back to 100%. In this structure, the lateral strain generated by the glitches blocked most of the misfit dislocations from propagating beyond the glitch (alloy) region sparing the Ge p - i - n device from defects. The resulting

diode leakage was lowered to within less than an order of magnitude from the theoretical diffusion-limited saturation current in an ideal Ge p - n junction.

Temkin *et al.*⁷⁷ first reported the properties of a strained-layer p - i - n $\text{Si}_{1-x}\text{Ge}_x$ superlattice waveguide detector. In an effort to boost quantum efficiency, Temkin focused incident light into a waveguide formed by the larger index of refraction multi-layer superlattice which was sandwiched between two thick layers of n - and p -type Si. Internal quantum efficiencies of 40% at 1.3 μm were reported with a frequency response bandwidth over 1 GHz.

A short time later, Temkin *et al.*⁷⁸ demonstrated photoconductive gain in a $\text{Si}_{1-x}\text{Ge}_x$ strained-layer superlattice detector attributed to hole trapping in the alloy wells. A $\text{Si}_{0.6}\text{Ge}_{0.4}$ waveguide device showed an optical gain as large as 40 at 1.3 microns with a 5-7 Volt bias. In addition, the magnitude of the gain scaled with the depth of the wells. Electron tunneling in the valence band was ruled out due to the relative thickness of the Si barriers compared to the wells, relatively high electron mobility, and unvarying spectral response with applied forward bias.

In 1986, Pearsall *et al.*⁷⁹ measured the avalanche gain in $\text{Si}_{1-x}\text{Ge}_x$ heterostructure photodiodes. In this case, IR absorption occurred in a $\text{Si}_{1-x}\text{Ge}_x$ strained-layer superlattice which served as the waveguide core, while avalanche multiplication took place in one of the Si-cladding layers. The separate absorption and multiplication regions were carefully designed so that the electric field in the absorption region remained below threshold for impact ionization, but high enough to ensure a rapid sweep of photocarriers. Multiplication factors as high as 50 were obtained for 1.1 μm response.

Recent Intraband Devices. One of the first, most important, papers germane to this dissertation was published in August of 1988 by Yang and Pan,⁸⁰ who first proposed and calculated intersubband absorption of n -type $\text{Si}_{1-x}\text{Ge}_x$ MQWs at 10 μm for (100), (110), and (111) Si substrates. Their theoretical studies concluded that for the [110] and

[111] growth directions, normal incidence absorption was allowed due to the anisotropic effective mass of Si. Infinite barriers were assumed, strain effects were neglected, and simplified envelope functions for the calculation of the optical matrix elements were used. This paper provided quantitative analysis that normal incidence transitions were allowed in structures grown on non-conventional Si substrates since the parallel motions of electrons from normal-incidence light could be coupled to their perpendicular motion due to the effective-mass anisotropy.

From the Yang derivation, the optical transition matrix elements for SiGe multiple quantum wells may be written in the dipole approximation as

$$\langle \psi_i | H | \psi_f \rangle = \sum_{\mathbf{k}} \varphi_i^*(\mathbf{k}_z) \varphi_f(\mathbf{k}_z) \times \left[-\left(\frac{e}{\hbar c} \right) A_0 \hat{e} \cdot \nabla_{\mathbf{k}} \epsilon(\mathbf{k}) \right],$$

where H is the Hamiltonian acting on the initial and final electron wave functions ψ_i and ψ_f . A_0 and \hat{e} are the amplitude and polarization of the vector potential, $\epsilon(\mathbf{k})$ is the bulk energy band structure which determines the effective mass tensor, and $\varphi_i(\mathbf{k}_z)$ and $\varphi_f(\mathbf{k}_z)$ are the initial and final states of the electron envelope functions. As explained earlier, if $\epsilon(\mathbf{k})$ is isotropic, as in an origin-centered, spherical, constant-energy surface where $\epsilon_{xx} = \epsilon_{yy} = \epsilon_{zz}$, then normal incidence light, i.e. $\hat{e} = \hat{x}$ or $\hat{e} = \hat{y}$ which lies in the quantum well plane, yields a zero off-diagonal optical matrix element since the initial- and final-state envelope functions, φ_i and φ_f , are orthogonal. If $\epsilon(\mathbf{k})$ is not isotropic, such as the tilted ellipsoidal energy surface that would be viewed from the [110] or [111] directions, and either m_x^* or m_y^* is not zero, the intersubband transition is allowed.

An absorption coefficient at 10 μm was evaluated next for doped $\text{Si}_{1-x}\text{Ge}_x$ MQWs grown on (100), (110), and (111) Si substrates from the rate of intersubband transitions per unit volume per unit photon flux. The n -type doping necessary to achieve a 6 meV shift of the Fermi energy was different for each orientation, ranging from 10^{18} cm^{-3} for

[100] to about 10^{19} cm^{-3} for [111]. However, unlike the [100] orientation, the [110] and [111] growth directions showed an exceptionally large absorption since a non-zero effective mass element m_{zx}^* exists for those orientations (see Table II).

Karunasiri *et al.*⁸¹ were the first to observe intersubband infrared absorption of holes in a $\text{Si}_{1-x}\text{Ge}_x/\text{Si}$ superlattice. The minibands of the superlattice were populated with holes using an external bias across the device, and an enhanced photoresponse was observed when the emitter Fermi level aligned with one of these minibands. The results from this technique were further validated when peaks in photoresponse measurements appeared very close to the high conductivity regions in the dI/dV vs. V characteristics. In addition, polarization dependent data agreed well with selection rules.

Table II. Theoretical results for absorption coefficients of Si and Ge on various substrates.

QW material	substrate	$\alpha(x) \text{ cm}^{-1}$	$\alpha(y) \text{ cm}^{-1}$	$\alpha(z) \text{ cm}^{-1}$
Si	[100]	0	0	7100
	[110]	19800	0	43400
	[111]	4100	1400	81000
Ge	[100]	1500	770	70900
	[110]	0	6500	17500
	[111]	0	0	1200

Rajakarunanayake and McGill⁸² presented detailed calculations of absorption coefficients, and peak absorption wavelengths for intersubband transitions from n -type $\text{Si}_{1-x}\text{Ge}_x/\text{Si}$ superlattices grown on (100), (110), and (111) Si substrates. Peak absorption strengths of about $2000\text{-}6000 \text{ cm}^{-1}$ in the $8\text{-}12 \mu\text{m}$ range were obtained for typical sheet doping concentrations of 10^{12} cm^{-2} . This paper extended the earlier work by Yang and Pan⁸⁰ by rigorously accounting for strain effects and using more realistic band offsets.

Lin and Maserjian⁸³ introduced a new approach to Si-based IR detector design by fabricating a device based on internal photoemission over a $\text{Si}_{1-x}\text{Ge}_x/\text{Si}$ heterojunction

barrier. This HIP (hetero-junction internal photoemission) device was grown by MBE and required a degenerately doped p^+ -type $\text{Si}_{1-x}\text{Ge}_x/\text{Si}$ layer for strong IR absorption and photoresponse. Doping concentrations up to 10^{20} cm^{-3} were achieved using boron. The photoresponse of the device was found to be tailorable, and was extended into the LWIR by varying the Ge ratio, x , in the alloys layers. Results were obtained with $x=0.2, 0.28, 0.3$, and 0.4 on Si (100) substrates. Photoresponse at wavelengths ranging from $2\text{-}10 \mu\text{m}$ were obtained with QE above $\sim 1\%$ in these prototype devices.

Just as researchers from AT&T (such as Luryi, Temkin, Kastalsky, Bean, and Pearsall) dominated this field in the mid to late 1980's, several papers from researchers at UCLA (Wang, Karunasiri, Park, and Lee) began to dominate this area in the early 1990's. In June, 1990, Arbet-Engels, Karunasiri, and Wang reported the fabrication and testing of Si_MGe_N superlattice $p\text{-}i\text{-}n$ diodes using photocurrent spectroscopy.⁸⁴ In this work, the optical properties of SLs with a 10 monolayer periodicity were studied, each grown on (100), (110), and (111) Si substrates. Structural integrity was checked using TEM and X-ray diffraction spectroscopy. Although the (100) sample appeared to be near perfect with no misfit dislocations, the (110) sample had many twins but only a few dislocations, while the (111) sample showed very poor surface morphology. No evidence of a direct band gap was observed for any of the three orientations studied. Superlattices grown on the Si (100) substrate had transition energies explained by strain induced splitting of the light and heavy hole bands. For the (110) substrate, an absorption band edge at 0.67 eV was shown to originate from a confined hole band and an unconfined electron band in a nearly flat, Type I, conduction band. The (111) sample, which suffered from several defects, had very low photocurrent response.

Next, Karunasiri *et al.*⁸⁵ were the first to report intersubband IR absorption of holes in MQWs using $\text{Si}_{1-x}\text{Ge}_x/\text{Si}$ alloys at room temperature using FTIR spectroscopy and waveguided structures. An absorption peak at $8.1 \mu\text{m}$ was reported due to a

transition between the first two heavy hole bound states. Hole intersubband IR absorption in δ -doped p -type Si MQWs was first observed by Park *et al.*⁸⁶ Absorption peaks ranged between 3 and 7 μm and could be tuned by varying the doping concentration in the δ -doped layer. Polarization-dependent spectra showed good agreement with the intersubband selection rules and strongly suggested the transitions occurred between the first two heavy hole subbands. This device had some advantages over the SiGe/Si MQW structures developed by Karunasiri in that the total thickness of the device was not limited by the critical thickness of the strained SiGe. Therefore, one could grow as many doped layers as desired (or increase the well period) to enhance the quantum efficiency and absorption strength.

Karunasiri *et al.*⁸⁷ continued to investigate variants of a p -type (100) $\text{Si}_{1-x}\text{Ge}_x/\text{Si}$ MQWs and demonstrated a LWIR detector with a broad photoresponse peak near 9 μm with a FWHM of 6-12 μm (80 meV). A reduction in absorption strength was observed as the polarization angle was increased. In addition, the spectrum was considerably broader than what is normally observed in a III-V based QW structure (40 meV) which is due mainly to the nonparabolicity of the hole band causing the transition energy to partially depend on the transverse momentum.

Park *et al.*⁸⁸ further validated these results by providing photoresponse curves for similar p -type SiGe/Si MQWs as a function of beam polarization. For the 0° polarization case, the photoresponse was due to intersubband transitions between two heavy-hole subbands and in a small part due to internal photoemission of holes excited via free-carrier absorption. At 90° polarization (normal incidence), the intersubband transition was forbidden. The free-carrier absorption, however, was much stronger at 90° than at 0° polarization since the entire photon electric field lay in the x - y (growth) plane. Therefore, intersubband transitions were shown to be forbidden by selection rules in that type of structure for normally incident light, while free-carrier absorption was observed, primarily

due to heavy doping in the wells. This paper was significant since it proved that although free-carrier absorption was relatively weak at normal incidence, it was not restricted by the polarization field, and IR detection at normal incidence was at least possible on a Si (100) crystal.

Park also provided two other possible, yet admittedly very weak, mechanisms for normal incidence detection: (1) intervalence-subband transitions from the ground state of the heavy hole to the subbands of the light hole or the spin orbit split-off hole, and (2) non-parabolicity. However, these effects were considered too small in these structures and normal incidence detection was primarily attributed to internal photoemission.

Strong electron intersubband IR absorption from 5.8-8.1 μm in Sb δ -doped Si MQWs grown on a (100) Si substrate was reported by Lee *et al.*⁸⁹ Lee observed that peak positions could be tuned by changing the doping concentration in the QWs. As the doping concentration was increased, the absorption peak position shifted to higher energies since the potential well becomes deeper and the energy difference between subbands becomes larger. For QWs grown on (100) Si, intersubband transitions occurred only when an optical field component lay perpendicular to the quantum plane. Absorption strength was shown to be proportional to the square of the electric field component which varied as $\cos^2\theta$.

Later that same year, Lee *et al.*⁹⁰ reported the first observation of electron intersubband IR absorption for *n*-type, Sb δ -doped $\text{Si}_{1-x}\text{Ge}_x/\text{Si}$ MQW structures grown on (110) substrates. As in typical *n*-type GaAs/AlGaAs MQW IR detectors and the recent *p*-type structures grown on (100) Si substrates at UCLA, selection rules prohibited, or at least limited, the absorption of incident light normal to the QW layers. However, intersubband absorption was shown to be allowed for *both* optical field components perpendicular and parallel to the quantum wells due to the tilted ellipsoidal of constant energy surfaces—in other words, the intersubband transition of the (110) crystal did *not*

exhibit strong polarization dependence as did the (100) Si substrate. Absorption peaks ranged from 4.9-5.8 μm . As in past structures, peak energy was shown to be tunable from the far IR to a few microns by varying the germanium composition in the alloy barriers and the doping concentration in the Si QWs.

The absorption characteristics of this (110) Si crystal is explained by the effective mass tensor of electrons in the $X4$ valleys having both diagonal and off-diagonal terms due to the four tilted energy ellipsoids in k -space. As described earlier, the parallel field defined in this work is the optical field component along the QW planes or an electric field at normal incidence. The off-diagonal terms of the mass tensor contributed to the electron motion in the growth direction by the parallel (normal incidence) field. The diagonal terms contributed a component of the electron mass and its subsequent transport in the growth direction by the perpendicular field. The perpendicular field is the optical field along the [110] QW growth direction. Lee's results indicated that the effective electron mass is $0.32m_0$ in the growth direction, and $0.47m_0$ in the quantum plane.

Since the mass tensor of electrons in the $X2$ valleys has no off-diagonal terms, it cannot affect electron transport in the QW growth direction by the parallel (normal incidence) field. Therefore, only the perpendicular field can induce intersubband transitions for electrons in the $X2$ valleys as in the case of (100) Si. The effective mass of electrons in the two $X2$ ellipsoidals is the transverse mass or $0.19m_0$. Therefore, even though a parallel field (normal incidence light) cannot cause intersubband transitions for (100) substrates, it may induce relatively strong intersubband transitions for a (110) crystal.

Table III lists the transitions which have been reported thus far in doped $\text{Si}_{1-x}\text{Ge}_x$ MQWs. The goal of this research is to extend the results observed in n -type, antimony δ -doped $\text{Si}_{1-x}\text{Ge}_x$ /Si MQW structures grown on (110) Si substrates to boron doped, p -type (110) and (111) crystals. The most important theoretical questions to ask at this point are the following: Does the tilted-ellipsoid argument presented by Yang and Pan only apply

to *n*-type structures involving electron intra(conduction)band-intersubband transitions? If so, then this argument is only appropriate for Type II MQW structures with heavily doped *n*-type wells in the Si layers. On the other hand, Chang and James,⁹¹ imply intersubband transitions should occur on any substrate orientation primarily due to

Table III. Summary of intersubband, intervalence-subband, and free-carrier transitions observed in Si_{1-x}Ge_x/Si MQWs as a function of incident light polarization and silicon substrate. Note that intersubband transitions have been recently observed only on *n*-type (110) crystals with very weak polarization dependence.

Polarization ⇒ Si substrate ↓	\bar{E}_N (90°)	\bar{E}_P (0°)
<i>p</i> -type (100)	free-carrier (strong) intervalence-subband (weak)	free-carrier (weak) intersubband (strong)
<i>n</i> -type (100)	free-carrier (strong) intervalence-subband (weak)	free-carrier (weak) intersubband (strong)
<i>p</i> -type (110)	not published	not published
<i>n</i> -type (110)	free-carrier intersubband	free-carrier intersubband
<i>p</i> -type (111)	not published	not published
<i>n</i> -type (111)	not published	not published

the strong intermixing of heavy- and light-hole states creating finite dipole matrix elements. Will intersubband transitions on non-conventional *p*-type Si substrates exhibit a strong polarization dependence as observed in (100) samples? Will *p*-type structures grown on non-conventional substrates exhibit normal-incidence absorption via intervalence-subband transitions at higher energies? Will these intervalence-subband transitions be polarization dependent? These are questions which need further investigation.

Using bandgap engineering techniques, one may enhance optical absorption in the more desirable 2-5 μm and 8-12 μm ranges via higher-energy bound-to-free transitions in the VB and lower-energy subband-to-subband transitions within the VB well, respectively. Using non-conventional Si orientations may then allow this absorption at normal incidence—a critical requirement, ultimately, for efficient detector array fabrication.

Background Summary

One's ability to characterize the energy band diagram of a material, and design microstructures for specific applications, provides unprecedented potential for device development. Bandgap engineered silicon-germanium superlattices offer the following advantages in making a photodetector:

(1) the basic materials and their alloys are well understood and their growth and device fabrication techniques are well developed

(2) a Si-Ge superlattice can be bandgap engineered to be responsive at a desired wavelength in the near to mid IR with low noise

and

(3) the quantum-well effects of the superlattice provide high charge carrier mobility needed for a fast and sensitive solid-state detector

Nearly all silicon devices used today are grown on (100) Si substrates, so there is an obvious push to investigate this crystal orientation for IR detection in the hope of easily building monolithic multi-device chips. However, to extend normal incidence detection properties of Si beyond 2 μm , one needs to exploit intersubband transitions from a heavily-doped, first heavy-hole state to another valence band state near the continuum. At this time, various types of detectors made with other materials responsive at these desired wavelengths exist; however, most of these devices are thermal detectors which are slow with low detectivity. Recent advances in GaAs, which suffers from the same selection rules as Si, have permitted limited high-speed, normal-incidence detection using an etched-

grating front surface which flips the polarization in a more favorable orientation. Yet, to take full advantage of our Si-based VLSI technology and build large, uniform focal plane detector arrays, Si-based detector technology needs to be vigorously investigated. Recent theoretical studies show that (110) and (111) Si have strong linear absorption coefficients for normal incidence light; therefore, a reasonable course of action would be to experimentally investigate structures grown on these non-conventional orientations. A recent summary of papers show that structures listed in Table IV have already been investigated. This table clearly illustrates that the optical emission and detection properties of SiGe superlattices grown on non-conventional Si substrates require further investigation—this is the primary thrust of this dissertation.

Table IV. Superlattice IR detectors and crystal orientations reviewed in literature. Crystal orientations which are "struck through" have already been investigated.

Structure	Substrate
undoped Si_MGe_N MQWs	(100) , (110) , (111) Si
<i>n</i> -type $\text{Si}_{1-x}\text{Ge}_x$ MQWs	(100) , (110), (111) Si
<i>p</i> -type $\text{Si}_{1-x}\text{Ge}_x$ MQWs	(100) , (110), (111) Si
<i>n</i> -type Sb δ -doped Si MQWs	(100) , (110), (111) Si
<i>p</i> -type B δ -doped Si MQWs	(100) , (110), (111) Si
<i>n</i> -type Sb δ -doped $\text{Si}_{1-x}\text{Ge}_x$ MQWs	(100), (110) , (111) Si

III. Experimental

Samples

Growth Process and Physical Description. The SiGe multiple quantum wells were grown on 76 mm (100), (110), and (111) Si wafers using molecular beam epitaxy (MBE). Details of the growth system have been reported earlier.⁹² The Si and Ge molecular beams were obtained from elemental sources in electron gun evaporators. Boron doping was obtained from a specially designed high temperature effusion cell. Prior to growth, the substrates were cleaned by a modified Shiraki process^{93,94} which resulted in a H-terminated surface. Three commercial *p*-type Si substrates were used with resistivities of 10-20 $\Omega\cdot\text{cm}$ for (100) and (111) Si, and 20-70 $\Omega\cdot\text{cm}$ for (110) Si. The (110) and (111) Si wafers had the final 2.5% HF dip followed by a buffered HF dip, which appeared to result in fewer surface defects. All chemical cleaning was done in a standard hood in air. Immediately after cleaning, the wafers were loaded into a commercial Si MBE system for the growth of the Si epitaxial layers. Typical pressures were a base pressure of $\sim 10^{-9}$ Pa prior to filling of the liquid nitrogen cold traps and $6-9 \times 10^{-7}$ Pa during growth. Immediately preceding growth, the surface hydrogen was removed by heating the sample to 650 °C. The epitaxial growth was done with the substrate at set temperatures of 550, 650, 710, 800, or 850 °C. Temperature control was accomplished with pyrometer temperature measurement with feedback to the substrate stage heater. Temperature calibration was accomplished prior to growth by comparison with the eutectic temperatures of Au and Al on Si. A 1700 Å Si buffer layer was grown prior to the multiple quantum well growth. A typical structure was composed of five 40 Å $\text{Si}_{0.8}\text{Ge}_{0.2}$ quantum wells separated by 300 Å of Si. The quantum well widths were controlled by shuttering the Ge flux. The $\text{Si}_{1-x}\text{Ge}_x$ wells had germanium compositions, x , ranging from 0.20 to 0.50. All doped samples had boron

concentrations ranging from 1×10^{19} atoms/cm³ to 1×10^{20} atoms/cm³, 30 Å on center in the VB well, corresponding to sheet dopant concentrations ranging from 4.6×10^{12} to 2.2×10^{13} atoms/cm². The Si growth rate was 0.5 Å/s and the Ge growth rate was 0.13 Å/s. The growth rates were established by Si and Ge depositions on sapphire substrates, after which selective areas of the films were removed and the step heights were measured with surface profilometry. The typical superlattice structure was capped with 2000 Å of undoped, *p*-type silicon. X-ray diffraction analysis of a 1000 Å Si_{0.8}Ge_{0.2} layer with a 1000 Å Si cap was used to confirm the growth-rate measurements. Surface morphology was verified using 2×2 low-energy electron diffraction (LEED) and Nomarski optical microscopy. A schematic drawing of a typical superlattice structure is shown in Figure 13.

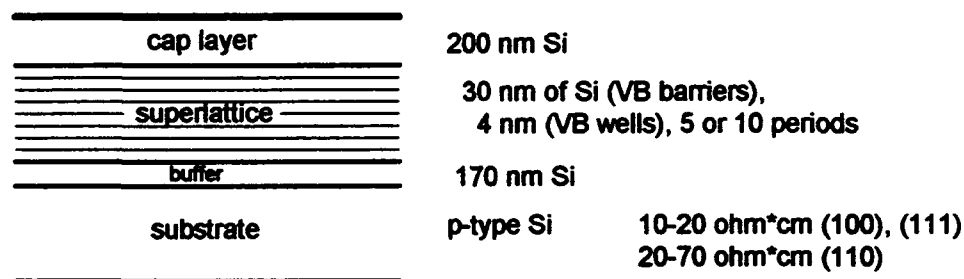


Figure 13. Schematic diagram of a typical superlattice structure.

Parametric Survey. The primary objective of this research was to investigate the photoluminescent and infrared absorption properties of Si-Ge superlattices grown on various silicon substrate orientations. The first step in this investigation then was to design a superlattice structure—a step which, in itself, involves dozens of growth, diagnostic, and device considerations born out in 15 years of research by many others

which has been reviewed in Chapter 1. A few important considerations are briefly summarized in Table V.

Table V. Design considerations for each physical region of a superlattice.

region	design options	considerations
cap layer	material type, dopant concentration, thickness	affects device configuration and defines charge carrier for electrical and photo-response measurements
	finish	increases internal reflectance for waveguide absorption measurements
superlattice	materials	determines energy band gap
	well/barrier thickness	defines charge confinement, tunneling probability, alters transition energies between discrete levels, shifts phonon spectra
	alloy composition	alters band gap, mechanical strain, absorption strength
	doping concentration	affects absorption strength
	period	defines total active region
buffer layer	material type, doping concentration, thickness	strain, strain stability, dislocation formation and propagation, material interdiffusion
substrate	material type	coordinated with cap layer to form device for electrical and photoresponse measurements
	orientation	affects location of band gap minima and maxima
	resistivity	affects free-carrier absorption
	finish	increases internal reflectance for waveguide absorption measurements

Initial studies often varied the superlattice well and barrier thicknesses to determine which emission lines were attributed to the superlattice and to investigate the bandgap emission characteristics of the material. More recent studies initially explored interband and intersubband absorption transitions on conventional silicon substrates and possible device configurations. The work reported in this dissertation extends this work by studying the effects of varying germanium composition and well doping concentrations on all three silicon substrates: the "conventional" or industry-standard

crystal (100), and the two "non-conventional" Si substrates (110) and (111). Figure 14 illustrates the parameter space of this research.

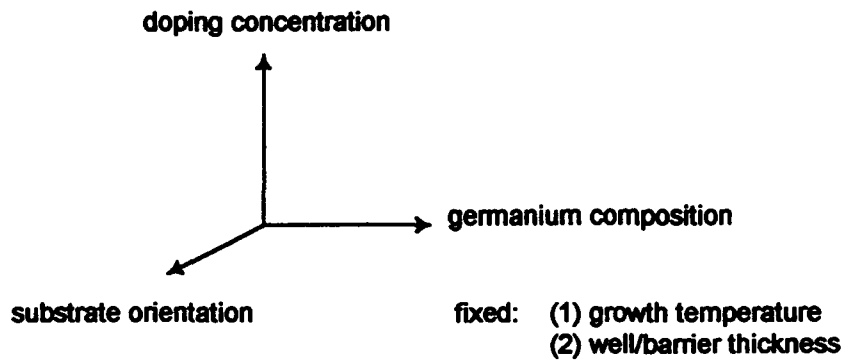


Figure 14. Parameter space for the research reported in this study.

Superlattice samples were grown at the Naval Research Laboratories (NRL) and sent to the Air Force Institute of Technology (AFIT) by express mail for optical diagnostics. Sample wafers were then cut and labeled for subsequent photoluminescence (PL) and Fourier transform infrared (FTIR) spectroscopy. Photoluminescence was first conducted on a specimen of each sample to determine crystalline quality and the results were transmitted by facsimile back to NRL. Mean-while, another sample specimen would be prepared to form an optical waveguide for FTIR absorption measurements. Table VI lists all the sample structures investigated.

When all equipment was fully operational, PL results were routinely provided back to the grower within three calendar days from initial growth. Expedient diagnostic response like this was essential in developing our understanding of the growth process on non-conventionally orientated substrates and building a sufficient stock of high-quality samples. During this process, several semiconductor growth parameters were also investigated. The effects of sample preparation, growth temperature, and growth

rate were also evaluated for the best crystalline quality and deposition kinetics to avoid dislocations and to maintain precise epilayer thickness control.

Post-Growth Annealing. Portions of the highest-quality superlattice samples grown on (100), (110), and (111) substrates were also used in an erbium ion implantation study. After implantation at 1 MeV, the superlattice structure was badly damaged and required rapid thermal annealing (RTA) to recrystallize the material. After cleaning each sample with an acetone scrub and methonal rinse, the RTA sample chamber was purged with N₂ gas. A forming gas consisting of 3% H and a balance of Ar was flowed over the samples as they were annealed with an A.G. Associates HeatPulse 210 RTA system at a Wright Laboratories (WL/ELR) facility. Annealing temperatures ranged from 450 °C to 850 °C in 50 °C increments. Annealing time was kept constant at 30 seconds for each temperature step.

Table VI. List of samples used in this research.

sample ID (substrate orientation)	germanium composition	boron conc. (atoms/cm ³)	VB well width (Å)	VB barrier width(Å)	number periods	growth temp. (°C)
21116.1(100)	0.20		30	300	5	710
21124.1(100)	0.20		30	300	5	650
21124.2(100)	0.20		30	300	5	550
21202.2(100)	0.20		30	300	5	710
30318.1(111)	0.20		36	360	5	710
30322.1(110)	0.20		36	360	5	710
30528.1(111)	0.20		30	300	5	710
30528.2(110)	0.20		30	300	5	710
30723.1(100)	0.20		30	300	5	550
30726.1(100)	0.20		30	300	5	710
30812.1(100)	0.20		40	300	10	600
30818.1(100)	0.30		40	300	10	600
30818.2(100)	0.40		40	300	10	600
30819.1(110)	0.20		40	300	10	710

sample ID (substrate orientation)	germanium composition	boron conc. (atoms/cm ³)	VB well width (Å)	VB barrier width(Å)	number periods	growth temp. (°C)
30819.2(111)	0.20		40	300	10	710
30908.1(100)	0.20		40	300	10	800
30915.2(100)	0.20		30	300	5	710
30916.1(100)	0.20		30	300	5	800
30921.2(100)	0.20	1×10 ¹⁹	40	300	5	710
30922.1(100)	0.20	1×10 ²⁰	40	300	5	710
30922.2(100)	0.20	5×10 ¹⁹	40	300	95	710
30924.1(100)	0.15		40	120	5	710
31006.2(100)	0.30		40	300	5	710
31007.1(100)	0.40		40	300	5	710
31007.2(100)	0.20		40	300	5	710
31013.1(100)	0.30	1×10 ¹⁹	40	300	5	710
31014.2(100)	0.40	1×10 ¹⁹	40	300	5	710
31015.1(100)	0.20	1×10 ¹⁹	40	300	5	710
31020.1(100)	0.20		40	300	10	850
31022.1(100)	0.10		40	120	95	710
31025.1(100)	0.50		40	300	5	710
40106.1(100)	0.20	1×10 ¹⁹	20	300	5	710
40107.1(100)	0.20	1×10 ¹⁹	60	300	5	710
40111.1(110)	0.20	1×10 ¹⁹	40	300	5	710
40112.1(111)	0.20	1×10 ¹⁹	40	300	5	710
40113.1(100)	0.20	1×10 ¹⁹	40	300	5	550
40303.1(111)	0.20		30	300	5	600
40303.2(111)	0.20		30	300	5	800
40304.1(110)	0.20		30	300	5	600
40304.2(110)	0.20		30	300	5	800
40404.1(110)	0.20	8×10 ¹⁹	40	300	10	550
40405.1(111)	0.20	8×10 ¹⁹	40	300	10	550
40406.1(110)	0.20		40	300	10	550
40407.1(111)	0.20		40	300	10	550
40504.1(100)	0.20	5×10 ¹⁹	40	300	15	550
40512.1(110)	0.20	5×10 ¹⁹	40	300	15	550
40513.1(110)	0.20		40	300	15	550
40520.1(110)	0.20	2×10 ¹⁹	40	300	15	550
40601.1(110)	0.30		40	300	15	550
40602.1(110)	0.30	2×10 ¹⁹	40	300	15	550
40708.1(100)	0.20		30	300	5	7100

Photoluminescence

Luminescence is an optical radiation (or light emission) process which occurs when an atomic or molecular system decays from a higher to a lower energy state. If the system is originally excited to a higher energy state by absorbing intense incident light, the resulting optical emission from the system is called photoluminescence (PL). PL is a highly valuable diagnostic tool to examine bulk and epitaxially grown semiconductors, and superlattices. A typical setup involves a laser illuminator, a temperature-controlled sample mount, a vacuum chamber, a monochromator and detector, collection optics, and signal electronics for storage and display. A laser is chosen with a wavelength corresponding to a photon energy above the band gap energy of the sample material:

$$E = h\nu \quad \nu\lambda = c$$

then

$$E = \frac{hc}{\lambda}$$

where E is the photon energy, h is Planck's constant, c is the speed of light, and λ is the wavelength of the source. Therefore, the 4880 Å line from an Ar^+ laser would have a photon energy of 2.54 eV, well above the 1.1 eV band gap of intrinsic silicon.

Similarly, a the 6471Å line from a Kr^+ laser would have a photon energy of 1.92 eV.

All PL data reported in this dissertation was taken with an Ar^+ laser operating at an optical power output between 50–60 mW in multiline mode.

Source Penetration Depth for Photoluminescence. The depth at which the laser beam penetrates the sample is determined by the absorption coefficient of the material at a particular wavelength and Beer's Law:

$$I(x) = I_0 e^{-\alpha x} \quad (5)$$

where $I(x)$ is the intensity of light as a function of depth, x , in the sample, I_0 is the intensity at the surface of the sample, and α is the absorption coefficient of the material.

From Eq (5)
$$x = \frac{-1}{\alpha} \ln \frac{I}{I_0}$$

defining
$$\frac{I}{I_0} = \frac{1}{e}$$

then
$$x = \frac{1}{\alpha}$$

A recent, very thorough study⁹⁵ of the dielectric functions of Si, Ge, and other important semiconductors provides extensive tables to interpolate absorption coefficients as a function of photon energy. A summary of important absorption coefficients and subsequent penetration depths computed from the previous expression are provided in Table VII.

Table VII. Absorption coefficients and penetration depths of available laser lines.

wavelength (Å)	photon energy (eV)	absorption (10 ³ cm ⁻¹)	penetration depth (μm)
6471 (red)	1.92	3.36	2.97
5145 (green)	2.41	15.0	0.665
4880 (blue)	2.54	20.6	0.484
3500 (UV)	3.54	1078	0.0093

When the sample is illuminated, excitation causes a non-equilibrium concentration of electrons and holes. At liquid helium temperatures (typically 3 K), electron-hole pairs form excitons which decay directly causing free-exciton luminescence. Additional structure in the spectra results from luminescence after these excited carriers are captured by donors, acceptors, or other impurities and defects (see Figure 15). Photoluminescence can be a very sensitive technique for detecting a wide variety of impurities and defects at very low concentrations. PL can also accurately measure band gap energies of bulk semiconductors, alloys, and superlattices.

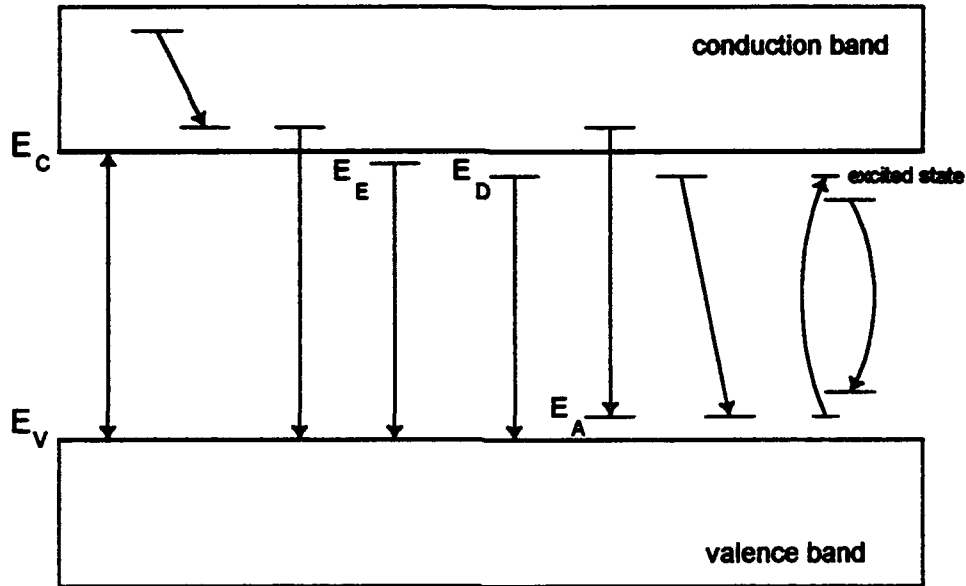


Figure 15. Schematic diagram of radiative transitions between the conduction band (E_C), the valence band (E_V), and exciton (E_E), donor (E_D), and acceptor (E_A) levels in a semiconductor.

The availability of easy-to-use lasers in a variety of wavelengths makes PL a superb semiconductor diagnostic; however, PL does have limitations. First, single-wavelength PL only probes the energy states below the energy gap. Only the lowest confined energy states that define the effective band gap of the superlattice are observed, other states near the gap energy must be probed using photoluminescence excitation spectroscopy (PLE). The overall experimental setup for PLE is essentially the same as PL, except a tunable laser is used to selectively excite states near the band edge. In addition, PL is still only a semi-qualitative process. Limited resolution of weak optical emissions and competition between various capture mechanisms and radiative and non-radiative processes make quantitative interpretation of PL spectra very difficult. However, after over nearly 30 years of research, several spectroscopic lines have been identified and serve as landmarks in the spectral emission of silicon. The most complete compilation of known emission lines to date may be found in Davies work.⁹⁶

Apparatus. A schematic illustration of the experimental apparatus used for photoluminescence is shown in Figure 16. All samples were mounted, strain-free, onto a copper cold finger inside a Janis Super VariTemp 10DT optical cryostat using rubber cement. A Welch Scientific 1397 vacuum pump was used to pump down the sample chamber to obtain sample temperatures as low as 1.4 K up to room temperature when used in concert with a thermal resistance heater mounted at the end of the finger.

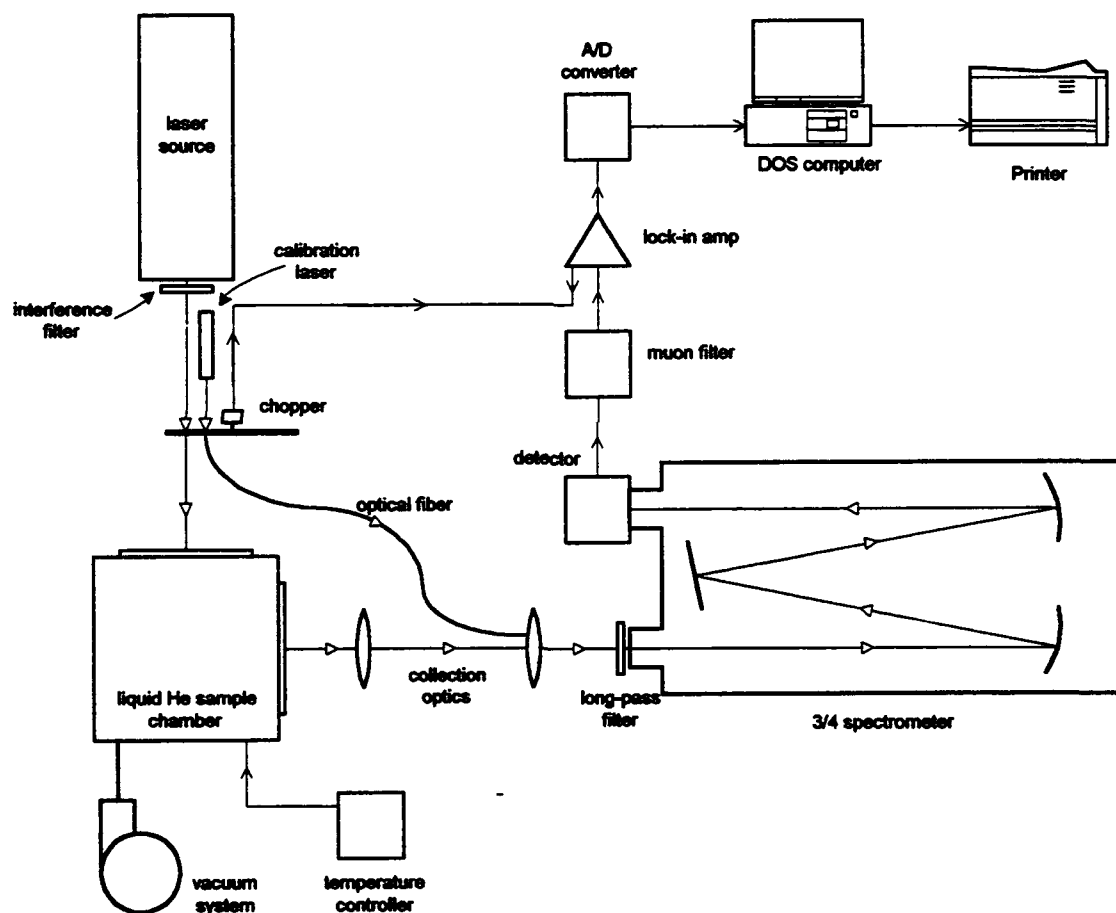


Figure 16. Schematic diagram of photoluminescence experimental apparatus.

Sample temperature was monitored by a Lakeshore 100DT silicon diode temperature sensor and controlled with a Lakeshore 805 temperature controller. Thermal isolation

between the liquid nitrogen cold jacket and liquid helium (LHe) reservoir on the Janis cryostat was achieved by evacuating the separation sleeve with an Alcatel CFV100 turbo-vacuum pump. The PL spectra was collected with a Spex1702, $\frac{3}{4}$ -meter, Czerny-Turner dispersive monochromator with $f/6.8$. Collection optics were f-matched to the sample chamber using a Newport KBX 154 lens with an outer diameter of $d=50.8$ mm and focal length $f=100$, and f-matched to the monochromator with a Newport KBX 193 lens with $d=76.2$ mm and $f=300$ mm. The signal was detected by a LN-cooled Applied Detector Corporation 403L solid-state germanium detector responsive from 0.8 to 1.7 μm . The analog signal was filtered by a North Coast 829B muon filter and amplified by a Stanford Research SR850 lock-in amplifier. After passing through a MetraByte DASH16F analog-to-digital interface board, the digital signal was received by a Zenith 248 (DOS-based IBM AT compatible) personal computer using Laboratories Technology Lab Tech Notebook version 5.0.3 data acquisition software. Laser excitation was provided by a Spectra Physics 2085 argon-ion laser with a dominant 4880 \AA line operating in multiline mode with a total optical power output set nominally to 50 mW. Spontaneous emission lines from the laser tube were filtered at the source with a 500 nm notch filter. Higher orders of the 4880 \AA laser line were filtered at the monochromator with a 1000 nm long-pass filter. The laser source was chopped with a Stanford Research SR540 optical chopper. The system was calibrated by a Melles-Griot Class IIIa helium gas laser that was first chopped and sent to the KBX 193 collection lens via a multi-mode optical fiber. A weaker, second-order line at 12,656 \AA (the primary 6328 \AA line times 2) was detected and written into the sample data file or recorded in a separate run. A linear regression technique was used later to calibrate the raw data to a data resolution of ± 0.5 meV. A 600 groove/mm grating blazed to

1.25 μm at first order was used in the Spex monochromator with input and output slits nominally set to 600 μm . With a grating plate factor of 21 $\text{\AA}/\text{mm}$, this corresponds to a spectral resolution of 12.3 \AA at 1.0 μm or 1.2 meV at 1.0 eV.

Sample Preparation and Mounting. Single, large samples, usually $\frac{1}{4}$ of a 3 inch diameter wafer were sent from the Naval Research Laboratories to the Air Force Institute of Technology by express mail. These samples were cut into smaller, 4 \times 4 mm, specimens using a Loomis Model MKT-38-LI machine wafer scribe, then bagged, and labeled. Before mounting on the cold finger, samples were sprayed with trichloroethylene (TCE), scrubbed lightly with a cotton swap soaked in acetone, rinsed with methanol, then rinsed again with de-ionized water. The samples were usually mounted, often four to a side, on a copper cold finger using a very small amount of rubber cement applied at the center of the upper half of the sample. During data runs, the laser spot would be centered on the lower half of the sample to minimize luminescence attributed to strain effects.

Data Acquisition Procedures. After mounting the sample, the sample chamber was cooled to liquid helium (LHe) temperatures by opening the throttle valve on the Janis dewar allowing the LHe reservoir to drip into the sample chamber. The sample is mounted on a copper cold finger just above this small pool of LHe, with the sample chamber pressure at typically 5 torr. The Ar^+ laser is switched on and allowed to stabilize. The Labtech software is configured to collect and display data. The scan range and duration is determined and this information is coordinated with the data acquisition system and the switch settings on the SPEX monochromator. A strong PL signal is sought from the sample by manually adjusting the monochromator to an expected signal wavelength. The lock-in amplifier is adjusted in sensitivity and phase locked to the optical chopper. Next, the collection optics are adjusted spatially for the strongest signal. The monochromator is manually reset to the start value of the scan

region. Once (1) the sample has reached thermal steady-state, (2) the laser power output is steady, (3) the data acquisition computer and monochromator are set for the correct start/stop values, scan speed, and scan duration, (4) the electronics sensitivity is tuned to a strong signal and phase locked, and (5) the optical system optimized—one is ready to take data.

System Response. The optical system response for this specific PL apparatus is shown in Figure 17. During this measurement, a 1000 °C blackbody source was placed near the sample chamber. The resulting spectra was determined by dividing the

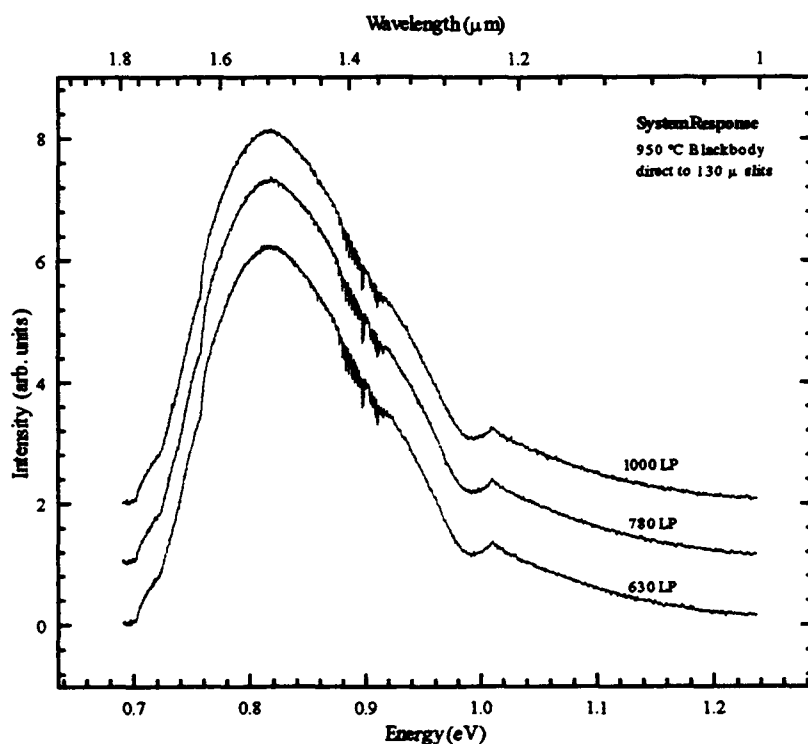


Figure 17. Optical system response of photoluminescence apparatus.

recorded data by the calculated output of perfect 1000 °C blackbody source. Results indicate relatively strong H₂O absorption occurs near 0.9 eV from water vapor found in

the laboratory atmosphere lying in the path between the sample chamber and the detector. Fortunately, this spectral region was totally avoided during this experiment, and as a result, no correction factors for changes in relative peak intensities were factored into any PL results. All PL reported in this work falls within a range from 0.95 to 1.25 eV.

Fourier Transform Infrared Spectroscopy

Introduction. The primary difference between Fourier transform spectroscopy (FTS) and other spectroscopic techniques is that the emission spectrum is obtained by taking the Fourier transform of an interferogram which is generated by a two-beam interferometer. This is fundamentally different from the photoluminescence (PL) technique mentioned earlier which is a "dispersive" spectroscopic technique. Dispersive spectroscopic techniques discriminate the total, multi-frequency, light signal emitted from the sample to spatially-separated, extremely narrow-frequency bands—just as a prism separates "white" light into a band of colors. In the experimental setup used for PL, the sample emission passes through a SPEX monochromator which uses a 600 groove/mm optical grating to spatially separate the signal into extremely narrow intensity bands as a function of frequency. The germanium detector responds to the signal intensity at each of these bands as the grating/mirror system scans the frequency-selected signal past the output slit. Other dispersive spectroscopic techniques may also use prisms, etalons, or combinations of these optical components; however, they all share the common function of spatially separating the signal as function of frequency, scanning the output past a detector, and recording the detector response.

FTS techniques, however, record the total intensity of the signal—all of the frequency-dependent intensities of sample emission—in a single interferogram. The primary optical system of the most basic FTIR setup is a Michelson interferometer which

consists of two plane mirrors at right angles to each and a beam splitter at 45° to the mirrors (see Figure 18). One mirror is fixed while the other is moved in a direction perpendicular to its front surface. The beamsplitter divides the incoming light from the source and, ideally, transmits 50% of the light to one mirror while the remaining energy is reflected to the other mirror. Beam splitters typically consist of a thin-film coating on a substrate material. The compensator is a second substrate of the same material and thickness as the beamsplitter which is placed in one leg of the inteferometer to equalize the optical path length.

Assuming a perfectly monochromatic source input, the two beams will be in phase when they return to the beamsplitter and constructively interfere when the two path lengths of the inteferometer are identical. Practically speaking, if one were to look into the inteferometer at the output, the field will appear bright. If one mirror is moved

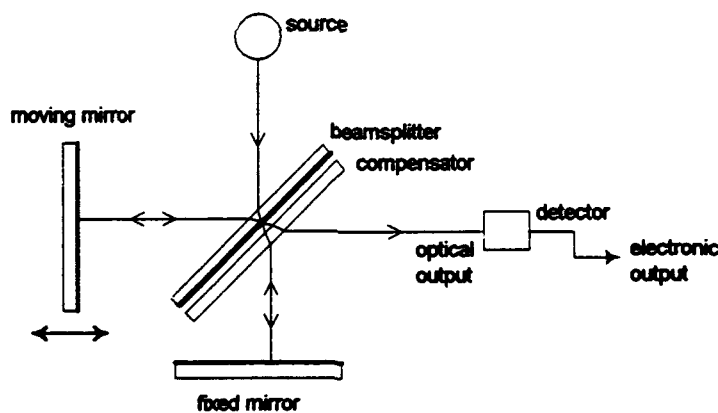


Figure 18. Michelson interferometer.

back $\frac{1}{4}$ of a wavelength, the two beams will now be 180° out of phase, destructively interfere, and the field will appear dark. If the moving mirror is smoothly translated in a single direction, the field would gradually appear light and dark for each quarter wavelength and form a perfectly oscillating sinusoidal signal which may be described as

$$I(X) = I(\nu) \cos(2\pi X \nu), \quad (6)$$

where $I(X)$ is the intensity of the output signal as a function of mirror displacement, X , and $I(\nu)$ is the source emission intensity as a function of optical frequency, ν . Note that $I(X)$ is the interferogram—a mapping of the optical signal intensity the detector senses at each position of the moving mirror. $I(\nu)$ is the emission spectrum.

The frequency of the output oscillation depends on (1) the frequency of the incoming, or source, electromagnetic radiation, and (2) the velocity with which the mirror is moved,

$$f = \frac{V}{(\lambda/2)} = 2V\nu,$$

where f is the frequency of the detected signal, λ is the wavelength of the incident monochromatic light, V is the velocity of the moving mirror, and ν is the frequency of the incident light measured in wavenumbers (cm^{-1}). This relationship allows a very high optical frequency to be encoded in the form of a low-frequency oscillation. For example, if we assume the moving mirror translates at a velocity of 0.25 mm/sec, then a $10 \mu\text{m}$ (1000 cm^{-1}) source is "down shifted" from an optical frequency of 3×10^{14} Hz to an acoustic frequency of 50 Hz. Magnetic voice coil actuators, piezoelectric transducers, and digital control systems can easily accommodate the acoustic frequency range. Voice coils are used to move the mirror in a continuous- or step-scan mode, while "piezos" keep the fixed mirror in dynamic alignment.

Of course, even a laser is not a perfect source of monochromatic light and the resulting interferogram is a less than perfect sinusoid. In fact, most FTS systems use a very broad band source of light to obtain the widest possible range of frequency information. The BioRad FTS-60V has two sources. SOURCE 1 is ceramic glowbar, a

high-resistivity thermal load that requires at least 30 minutes to temperature stabilize. This source is very dim in the visible and used for mid to far IR applications. SOURCE 2 employs a very bright tungsten-filament bulb and is used in the visible to near IR ranges. Both sources are encased in a temperature-controlled, copper-clad, water jacket.

When a broad-band source is considered, each frequency component is superposed onto each other, and although the resulting interferogram looks far from sinusoidal, the previous mathematical description is easily extended since each frequency may be considered independently. The resulting interferogram is the summation of all cosine oscillations caused by all of the optical frequencies of the source. When the two Michelson mirrors are equidistant, or have zero path difference, then all the waves are in phase and form a "centerburst." As the moving mirror translates away from the zero position, the independent oscillations rapidly sum out to a steady average value. The resulting ac signal (interferogram) obtained by moving the mirror may be expressed by

$$I(X) = \int_{-\infty}^{+\infty} I(\nu) \cos(2\pi X \nu) d\nu, \quad (7)$$

which is the integral of Eq. (6) of the monochromatic source over the entire frequency domain. (Recall the frequency, ν , is measured in wavenumbers, cm^{-1}). This equation is also one half of a cosine Fourier transform pair, the other half being

$$I(\nu) = \int_{-\infty}^{+\infty} I(X) \cos(2\pi X \nu) dX. \quad (8)$$

Equations (7) and (8) provide a clear relationship between the interferogram $I(X)$ and the spectrum $I(\nu)$. The interferogram is directly measured, while the spectrum may be found by simply taking its Fourier transform. Note however, that interferograms are seldom symmetric since it is impossible to make a perfectly-compensated interferometer

over an extended wavelength range. Imperfect compensation leads to sine components in the interferogram and an asymmetric centerburst. Therefore, the resulting interferogram and spectrum must be related by the following complex Fourier transform pair:

and

$$I(X) = \int_{-\infty}^{+\infty} I(\nu) e^{i2\pi X\nu} d\nu$$

$$I(\nu) = \int_{-\infty}^{+\infty} I(X) e^{-i2\pi X\nu} dX .$$

where the exponential term now contains both cosine and sine contributions.

Advantages of FTS Over Dispersive Spectroscopic Methods. In order to reconstruct the exact spectrum of the source, an interferogram would need to be measured from $-\infty$ to $+\infty$, which is impossible of course, since this would require an infinitely large interferometer. Since the interferogram can only be measured over finite mirror translation, the infinite interferogram discussed in the Introduction is, in effect, multiplied by a boxcar truncation function (i.e. $T(X)=1$ from X_{init} to X_{final} and $T(X)=0$ for all else). The convolution of the initial interferogram, $I(X)$, with the boxcar truncation function, $T(X)$, yields the resolution function of the form, $\sin(\nu)/\nu$, which is the Fourier transform of the truncated cosine wave. The central lobe of the resolution function is centered at the frequency of the cosine wave, as before, but now with finite width. This width, usually measured as the full-width-half-maximum (FWHM) of the central lobe, is inversely related to the maximum extent of the interferogram and the mirror movement. In general, the resolution of an FTS system may be roughly approximated by the following relationship:

$$resolution(cm^{-1}) \propto \frac{1}{mirror\ excursion\ (cm)} .$$

Therefore, as the number of cycles over which the cosine wave is observed increases, i.e. as the mirror moves further from mirror equidistance, the width of this resolution

function decreases and the resolution improves. It is important to repeat here that the "number of cycles" refers to the number of cosine wave oscillations corresponding to mirror displacement . For example, 128 cycles of a 6328 Å HeNe laser corresponds to the total mirror translation of 81 μm. Later, the "number of scans" refers to the number of times the mirror is repeatedly scanned through the total mirror displacement (in this case 81 μm), the results of which are "co-added" (averaged) to primarily smooth the spectra, which in effect, boosts the signal-to-noise ratio (SNR). In all cases, it is important to remember that the resolution function of the interferometer is fundamentally limited by the full travel range of the moving mirror. Controlling the moving mirror and keeping the entire system aligned had been an extremely difficult engineering problem until the relatively recent development of air bearings, digital control systems, and electro-mechanical transducers.

The resolution function may also be modified by multiplying the initial interferogram, $I(X)$, with something other than a simple boxcar truncation function to obtain a different resolution function. For example, using a triangle truncation function results in a resolution function of the form $\sin^2(\nu)/\nu^2$, which has much smaller side lobes than the $\sin(\nu)/\nu$ function, a narrower FWHM, and thus better resolution. The process of reducing the side lobes of the resolution function numerically by using a modified truncation function is called apodization. Also note, the multiplication of the Fourier transforms of two functions is mathematically known as the convolution of the two functions. For example, the multiplication of the interferogram by the boxcar function is analogous to the convolution of the spectrum with the resolution function $\sin(\nu)/\nu$. Only FTS has the unique ability to modify resolution by solely manipulating raw data using computational techniques such as apodization. Consider the impact of that last statement for a moment—with today's current computer capabilities, we can now

improve optical performance without changing a single optical element in the experiment!

A second, distinct advantage of FTS is that, unlike dispersive spectroscopic techniques, all optical frequencies are incident on the detector at once, or multiplexed. This is often referred to as Fellgett's advantage, and inherently permits exceptional trade-offs in the signal-to-noise ratio (SNR) and the time spent scanning the sample. In any spectroscopic system, spectral information contained in a narrower bandwidth than the resolution of the system is not observed. Therefore, the number of resolution elements of the spectrum, M , indicates the total amount of information contained in the spectrum and may be defined as the bandwidth, $\lambda_{\max} - \lambda_{\min}$, divided by the resolution $\delta\lambda$. In a dispersive spectrometer, the entire spectrum is observed for only a fraction of the total scanning time, T , divided by the number of resolution elements, M , observed in that time. The signal adds with the time spent observing it, while the random, white noise from the source adds as the square root of the observation time. Then, for a dispersive spectrometer, the signal adds as T/M , the noise as $(T/M)^{1/2}$, and the SNR as $(T/M)^{1/2}$. However, in an FTS system, each "resolution element" is being observed all of the time, i.e., all optical frequencies are multiplexed. Subsequently, the signal adds as T , the noise as $T^{1/2}$, and the SNR as $T^{1/2}$. After comparing the FTS and dispersive techniques on the basis of SNR alone, the multiplex case is superior to the dispersive technique by $M^{1/2}$. The Fellgett advantage is especially important when it becomes necessary for a researcher to examine a broad spectral bandwidth at high resolution.

Another advantage of FTS over a grating spectrometer is the increased light throughput. This is infrequently referred to as Jacquinot's advantage. While a dispersive spectrometer uses entrance and exit slits to act as aperture stops which filter side-lobe interference, a typical FTS use a relatively large diameter entrance aperture and turning mirrors. Compare a typical slit setting of 0.5×2 mm for a dispersive spectrometer with

a typical FTS setup comprising a 2-inch turning mirror set at 45° directing light into the sample chamber: 1 mm² versus ≈1050 mm²—an increase of over three orders of magnitude! This higher signal throughput is a valid advantage for all detectors.

In addition to having larger apertures, FTS setups are optically more efficient, since there are no reflection or transmission losses from dispersive gratings or prisms. Michelson mirrors and turning flats normally have broad-band, highly-reflective silver coatings. Collection mirrors on the far side of the sample leading to the detector are normally gold coated with even better broad-band behavior in the far IR than silver. High throughput and efficiency were the most important reasons why initial FTS techniques were developed in broad-band/low-light and narrow-band/high-speed applications. As a general rule, an equivalent spectrum may be measured with FTS in the same time as a grating spectrometer with better SNR or in a shorter time with equivalent SNR.

Although the FTS technique has been known for several decades, it was used only in extremely limited applications up until the 1970's, primarily because it required so much raw data reduction. Before high-speed analog-to-digital data acquisition systems and powerful computers, high-resolution FTS spectra could only be obtained over a very small spectral range. However, since the early 1970's, the throughput, speed, and resolution advantages of FTS have been extended over a broad spectral range limited only by appropriate detectors. The current state of technology in computer speed, data acquisition, reduced instruction set code, and the development of sophisticated algorithms for Fourier transforms, have greatly minimized this initial disadvantage. In fact, computer performance has improved so drastically in the past 20 years, that what was once this method's greatest weakness has become its greatest strength.

Apparatus. A functional schematic of the BioRad Fourier transform spectroscopy (FTS) system is shown in Figure 19. The Michelson interferometer is shown in the top half of the schematic comprising a source, beam splitter-compensator, translating mirror, and fixed mirror. A Class I HeNe laser is used for system calibration and dynamic alignment of the interferometer. Unlike the schematic representation in the figure, the BioRad FTS-60A actually has two sources, a ceramic glowbar (SOURCE 1) and a tungsten bulb (SOURCE 2), which may be software selected from the scan menu. The glowbar requires at least 30 minutes to thermally stabilize and is normally left on continuously. Preliminary runs may be accomplished just after the glowbar is turned on; however, if one wants to directly compare initial results with later runs, the system will require recalibration before each run until the source comes to equilibrium. When SOURCE 2 is selected, the glowbar switches off, the tungsten bulb illuminates, and a metal mirror drops into place injecting SOURCE 2 light into the interferometer. A potassium bromide (KBr) beamsplitter is used only with the glowbar source, while a quartz beamsplitter is used with the tungsten lamp. Compensators are built into the beamsplitter assembly which is kinematically mounted for easy removal and installation. The KBr beamsplitter must be stored and handled with extreme care since the thin film coating of this expensive optic readily absorbs moisture, or is hygroscopic. For example, the KBr beamsplitter must always be stored in a dessicated container or in a N₂-purged environment. One must only touch the sides of the optical mount of the KBr beamsplitter while ensuring that the palm of your hand never covers the optic when handling. Exposure to typical laboratory air for more than 30 minutes or even the moisture from simply cupping the beamsplitter in one's hand for a moment could ruin the optic. The interferometer compartment containing the beamsplitter is purged with dessicated compressed air with a N₂ gas purge emergency backup system. The moving

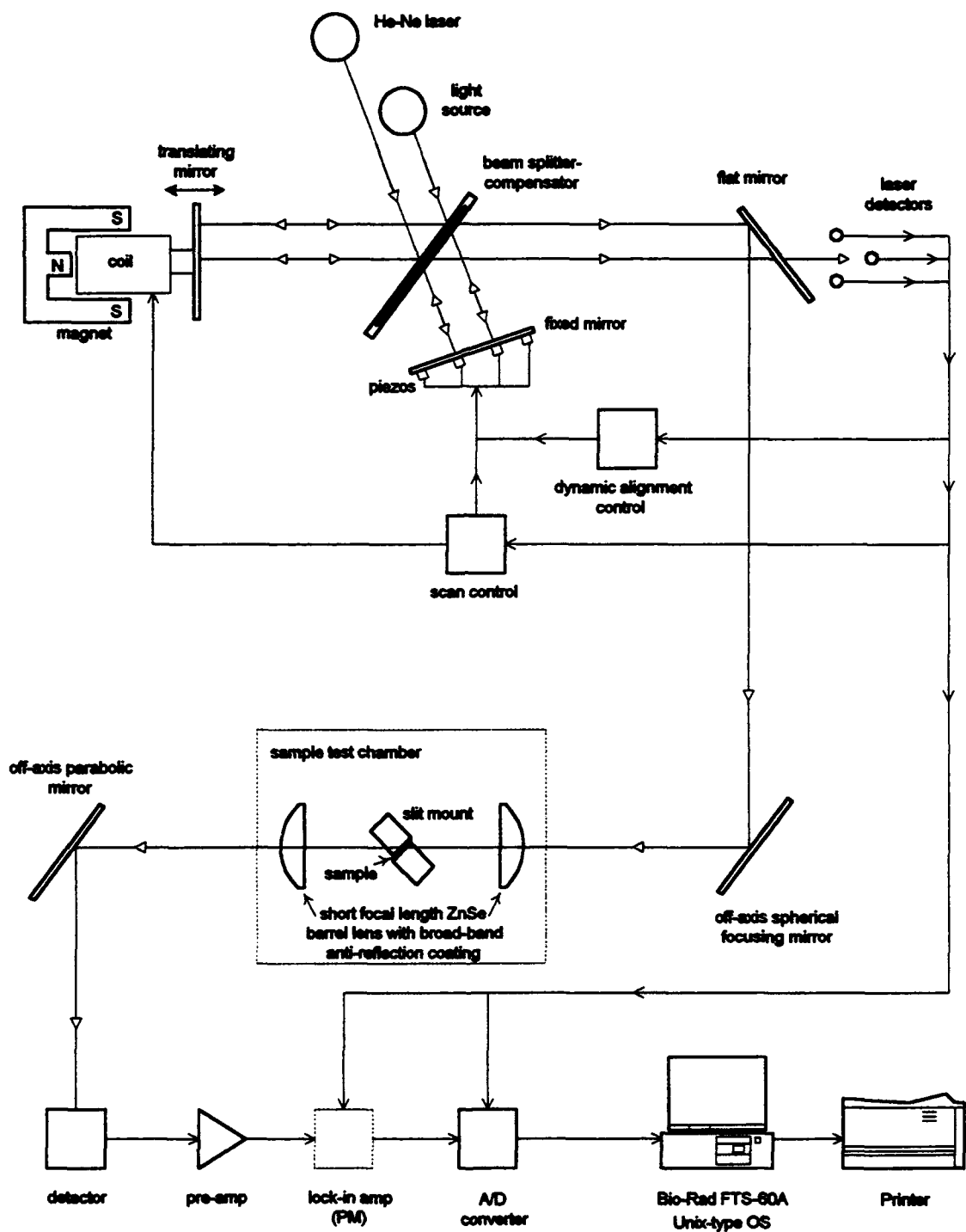


Figure 19. Functional schematic of the BioRad FTS system.

mirror has air bearings set at 18 psi and translates along the piston axis of the interferometer leg by a magnetic voice coil. Any errors in system alignment from the moving mirror are corrected by dynamically-controlled piezoelectric transducers mounted on the backside of the fixed mirror. The beam splitter is actually mounted at approximately 60° to minimize multiple reflections from its front and back surfaces. The inteferometrically modulated HeNe signal passes through a small aperture at the first turning mirror and is detected by a 3-point array of Si detectors. The subsequent electronic signal is sent to a digital control circuit for system alignment and to either the lock-in amp (if applicable) or directly to the analog-to-digital converter board as a system timing signal. The inteferometrically modulated light from the broadband source is directed to an Ag-coated off-axis spherical mirror where it is directed into an N₂-purged sample chamber. After passing through the sample the light emission from the sample is collected by an Au-coated off-axis parabolic mirror attached to the detector assembly and focused onto the face of the detector. Available detectors are listed in Table VIII, their complete specifications may be found in the laboratory

Table VIII. Currently available detectors, associated beamsplitters, and their effective range for the Bio-Rad FTS-60A.

detector	type	beamsplitter	eff. range (cm ⁻¹)	eff. range (μm)
silicon (Si)	photodiode	quartz	13000-25000	0.4 to 0.77
lead selenide (PbSe)	photodiode	quartz	3800-15000	0.67 to 2.6
deuterated triglycine sulfate (DTGS)	pyroelectric bolometer	potasium bromide (KBr)	400-5000	2.0 to 25.0

operations manual. The electronic signal is processed on a hard-wired motherboard built into the inteferometer unit, then sent to a 486-class, 50 MHz computer where the data is stored and displayed in a pseudo-Unix operating system environment written by

BioRad. After initial examination, selected files are converted to a disk operating system (DOS) format for further analysis, storage, and display.

Sample Preparation and Mounting. Samples were cut into 4×8 mm samples using a Loomis Model MKT-38-LI machine wafer scribe. The 8 mm edges were then beveled to 30.4 or 45 degrees and polished using the lapping jig shown schematically in Figure 20.

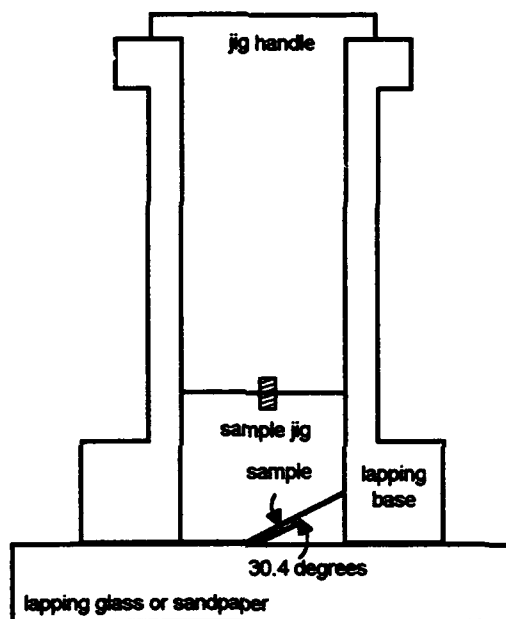


Figure 20. Lapping assembly used to fabricate an optical waveguide.

To fabricate waveguides, samples needed to be mounted on the sample jig, beveled, then polished—all without damaging the sample. First, the jig was heated on a hot plate. Then a bit of black wax was applied to the jig. Next, the sample was placed on the hot wax and tamped down evenly. The sample and jig were then immersed in a water bath to quickly cool the sample jig. The 8 mm edges were initially cut using 600-1500 grit sandpaper to grind the specimen edge. The best results occurred when the sample was pulled across the abrasive paper in one direction. Both 8 mm edges and the back side of the sample were then polished using the lapping glass lubricated with a

solution of 1.0 to 0.05 μm alumina polish beads mixed with one part Chlorox® bleach diluted with two parts de-ionized water. Each time a new sample was mounted or repositioned on the sample jig, the jig was heated, then quickly cooled in a water bath. Finally, wax residue was removed from the sample using trichloroethylene (TCE). The TCE was then rinsed from the sample with acetone, the acetone rinsed from the sample with methanol, the methanol rinsed away with de-ionized water and the sample allowed to air dry before mounting in the nitrogen-purged FTIR test chamber.

To create an optical waveguide, the front and back facets of the sample needed to be cut at a specific angle chosen after carefully considering how the sample was to be mounted inside the chamber, the index of refraction of silicon, and the most predominant emission wavelength from the intersubband transitions. A schematic of an optical waveguide with multiple internal reflections is shown in Figure 21. Figure 22 illustrates the waveguide facet geometry needed to determine the bevel angle.

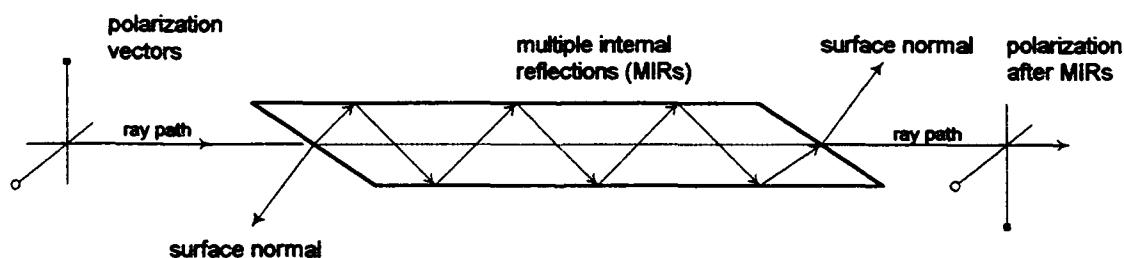


Figure 21. Schematic of sample fashioned into an optical waveguide.

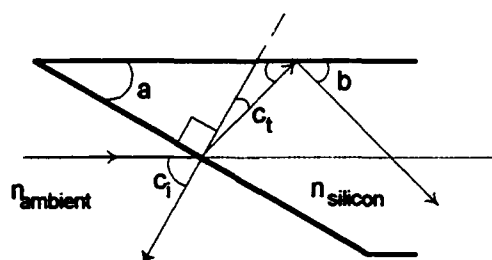


Figure 22. Facet geometry of a sample waveguide.

From Snell's Law $n_i \sin \theta_i = n_t \sin \theta_t$.

From the drawing $a + b + c_i + 90^\circ = 180^\circ$,

and $c_t = 90^\circ - a - b$.

Rewriting Snell's Law for this case yields

$$n_{amb} \sin(90^\circ - a) = n_{si} \sin(90^\circ - a - b) ,$$

where a is the bevel angle at which the facet must be cut measured from the front surface in this case, b is the multiple internal reflection (MIR) angle measured from the front and back surfaces of the sample, c_i and c_t are the incident and transmitted beam angles at the facet interface measured from the facet surface normal, n_{amb} is the index of refraction for the ambient environment in which the sample is placed, and the n_{si} is the index of refraction of the sample, which in this case, is primarily silicon. Since the longitudinal axis of the sample must be mounted parallel to the optical centerline in the cryostat assembly for low-temperature absorption runs, the optimal MIR angle, b was fixed at 45° . Therefore, the bevel angle, a , must be determined in terms of b which is fixed as a result of the experimental apparatus, and the indices of refraction. After several steps of algebraic manipulation and trigonometric substitution, this expression may be reduced to

$$a = \tan^{-1} \left[\cot b - \left(\frac{n_{amb}}{n_{si} \sin b} \right) \right] .$$

Since the only ambient conditions for the sample were high vacuum and immersion in dry nitrogen, then $n_{amb}=1$, leaving the following expression

$$a = \tan^{-1} \left[1 - \left(\frac{\sqrt{2}}{n_{si}} \right) \right] .$$

Now one only has to select the best index of refraction for silicon considering the expected absorption wavelength from the intersubband transitions. This decision must be arrived at prudently since the index of refraction for all materials changes as a function of wavelength, and once the sample facet is physically cut, the bevel angle is fixed. Fortunately, the index of refraction of silicon changes very little from the near to far IR. In fact, n_{Si} decreases only from 3.5 to 3.4 as the wavelength increases from 1 to 12 μm . The index of refraction of germanium also changes very little, from 4.1 to 4.0, in this same region. As a result, the the bevel angle for a silicon optical waveguide is relatively insensitive from 0.8 to 25 μm corresponding to the available source lamps and detectors associated with the FTIR apparatus. Figure 23 illustrates the waveguide bevel as a function of refraction index. Anticipating that intersubband absorption transitions would occur between 8 to 10 μm , the facet angle was cut to 30.4 degrees corresponding to the optimum facet angle for 45° MIR at 10 μm absorption. For room temperature measurements, all samples were cut with 45° facets and adjusted in azimuth for maximum signal.

Data Acquisition Procedures. System response must be determined for each optical configuration. Whenever a different filter, lens, window, or sample mount is installed, a new centerburst measurement must be accomplished to determine the appropriate combination of detector sensitivity and aperture settings. Achieving a centerburst magnitude ranging from -2.5 to -8.0 is necessary to ensure sufficient signal to noise during the actual measurement. After attaining a centerburst, the system must be re-aligned and recalibrated. The BioRad FTS-60A has a self-aligning Michelson interferometer and a software driver which enables both alignment and calibration to be accomplished with only a few keystrokes. As mentioned earlier, the ceramic glowbar (Source 1) also requires time to thermally stabilize and was normally always left on.

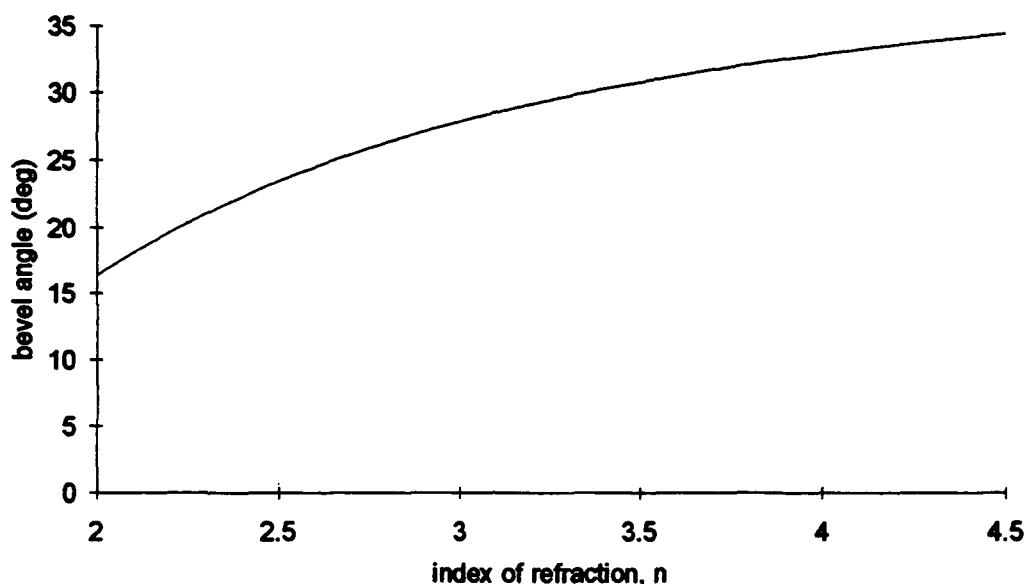


Figure 23. Waveguide bevel angle shown as a function of the index of refraction of silicon.

Valid measurements could be taken at least 30 minutes after turn on as long as the system remained calibrated. In addition, laboratory room temperature was also monitored—if the room temperature changed more than 5 °F the Michelson would require realignment and calibration. This actually became a bonafide concern during data acquisition since inadequate environmental control would sometimes cause room temperature to vary as great as 25 °F from 8:00 a.m. to 6:00 p.m. The single-most important step taken after calibration, was to take a background spectrum duplicating all aspects of the experiment as closely as possible without a sample loaded. The scan settings and the entire optical system, i.e. filters, lens, windows, and mounts, needed to be measured in place without a sample for a proper background subtraction later. Early test runs indicated that evacuating the cryostat and lowering the cryotip to liquid helium temperatures were unnecessary for low-temperature background runs. In summary, to

conduct reliable FTS measurements, one must accomplish the following steps in the order shown:

1. setup scan for a centerburst near -6.0
2. align and calibrate the system
3. run a 100% line
4. perform a background run
5. perform a sample run

System Response. A typical optical system response for this specific FTIR apparatus is shown in Figure 24. Results indicate relatively weak H₂O absorption occurs near 1650 and 3750 cm⁻¹, and CO₂ absorption at 2300 cm⁻¹. A constant N₂ purge through the sample chamber minimizes these effects.

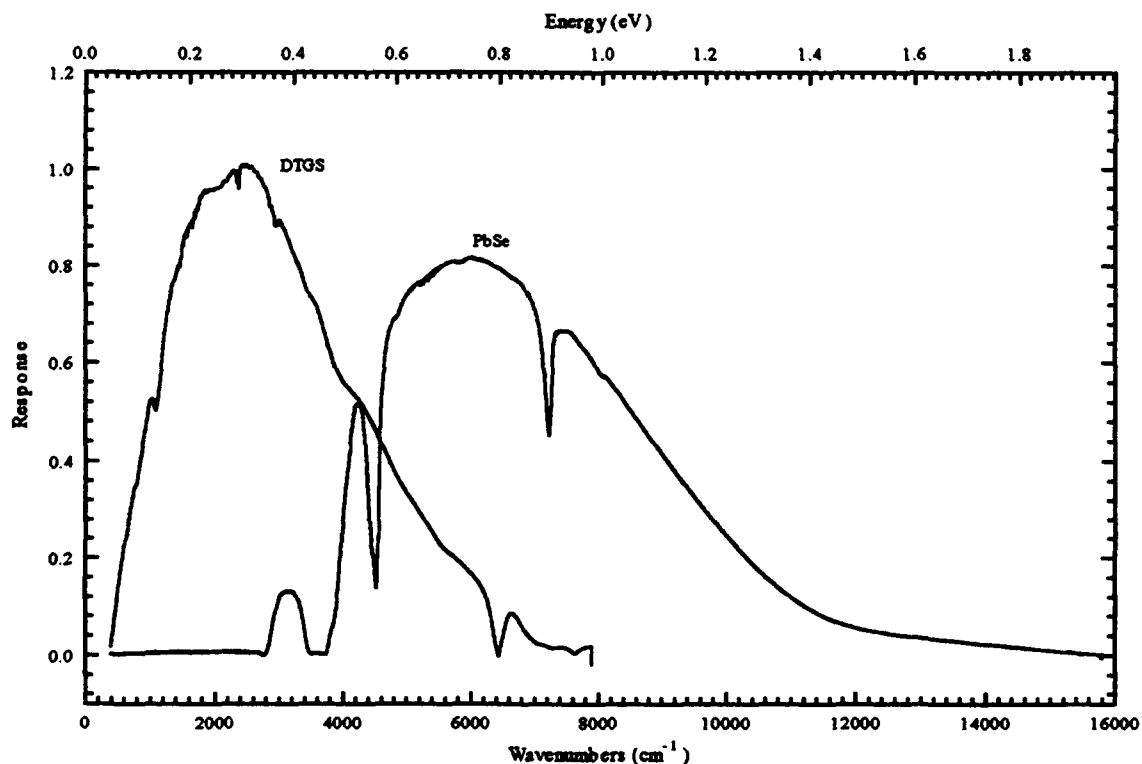


Figure 24. FTIR system response curve using the DTGS and PbSe detectors.

FTS Absorption Terms

Numerous absorption terms have arisen over the years from different fields of study. Absorbance has the most basic definition among these terms, but has been nearly replaced in favor of absorbance, a term preferred by chemists, and absorption coefficient, a term which defines absorption as a function of path length through the absorbing medium.

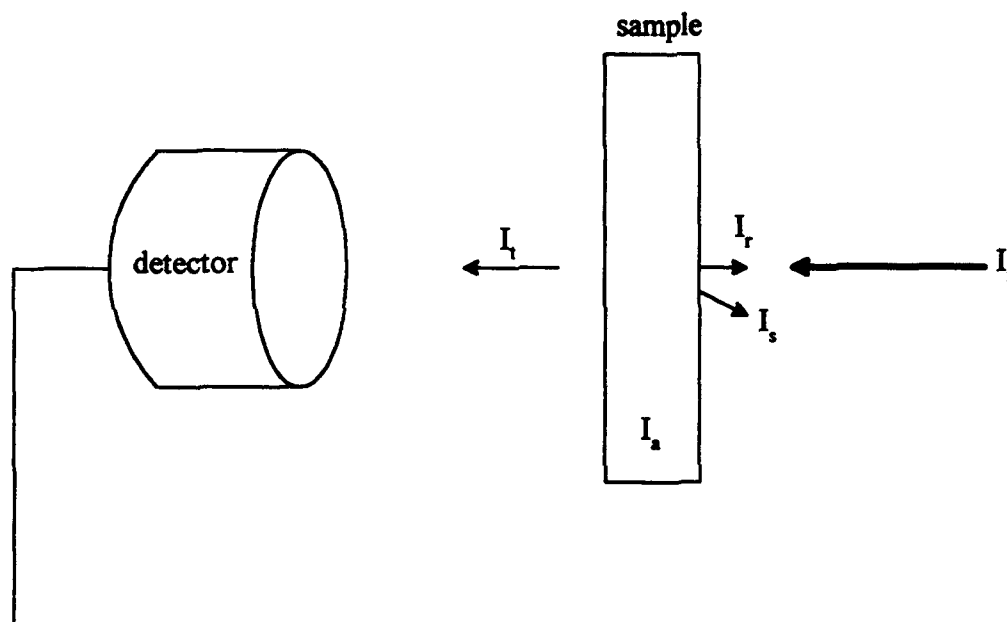


Figure 25. Schematic illustration absorption definitions.

From the simple illustration shown in Figure 25:

$$I_i = I_a + I_r + I_s + I_t,$$

where I_i is the single-beam spectrum intensity of the incident light, I_a is the light intensity absorbed in the sample, I_r is the light intensity reflected specularly from the front surface, I_s is the light intensity diffusely scattered from the front surface, and I_t is the light intensity which is transmitted. Assuming the reflected and scattered light is unchanged from sample to sample, then

$$I_i = (I_a + I_r + I_s) + I_t = I_{abs} + I_t,$$

and $\frac{I_{abs}}{I_i} + \frac{I_t}{I_i} = \text{absorbance} + \text{transmittance} = 1$.

Then

$$\text{transmittance} = T_{\text{meas}} = \frac{I_{\text{transmitted}}}{I_{\text{incident}}} = \frac{I_{\text{sample}}}{I_{\text{background}}},$$

$$\text{absorbance} = ABS = 1 - T_{\text{meas}} = 1 - \frac{I_{\text{transmitted}}}{I_{\text{incident}}} = 1 - \frac{I_{\text{sample}}}{I_{\text{background}}},$$

$$\text{absorbance} = \log_{10} \left(\frac{1}{T_{\text{meas}}} \right) = -\log_{10} \left(\frac{I_{\text{sample}}}{I_{\text{background}}} \right),$$

$$\text{and, absorption} = \alpha = \frac{-\ln(10^{-ABS})}{l_{\text{eff}}} = \frac{-\ln \left(10^{-\left(1 - \frac{I_{\text{sample}}}{I_{\text{background}}}\right)} \right)}{l_{\text{eff}}}.$$

I_{sample} and $I_{\text{background}}$ are the single-beam spectra recorded by the Fourier Transform Spectroscopy (FTS) system. Figure 26 illustrates the relative differences in magnitude among the different absorption terms. Since absorbance is less sensitive to small changes (from the *log* term), and the expression for absorption requires one to estimate the effective path length, l_{eff} , absorbance was chosen and is used throughout the remainder of this report.

Background Subtraction Techniques

A variety of background subtraction techniques were tested to enhance the absorption signal. Referring to Figure 27(a), normal incidence light, \vec{E}_N , has an electric field component (rising out from the paper) which lies on the quantum (x-y) plane as described in Chap 2. When the electric field vector is rotated perpendicular to the

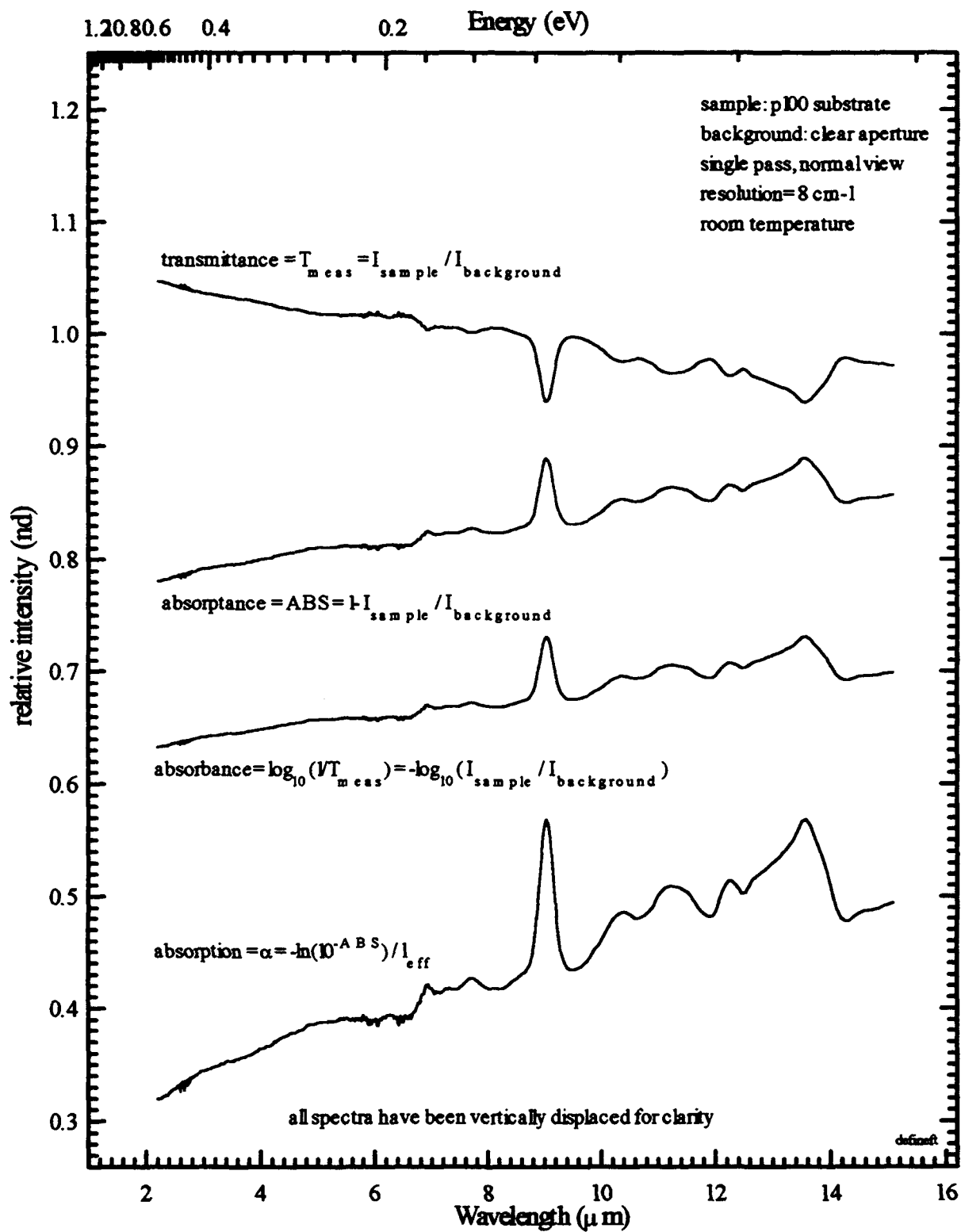


Figure 26. Data plot illustrating relative differences in magnitude of absorption terms.

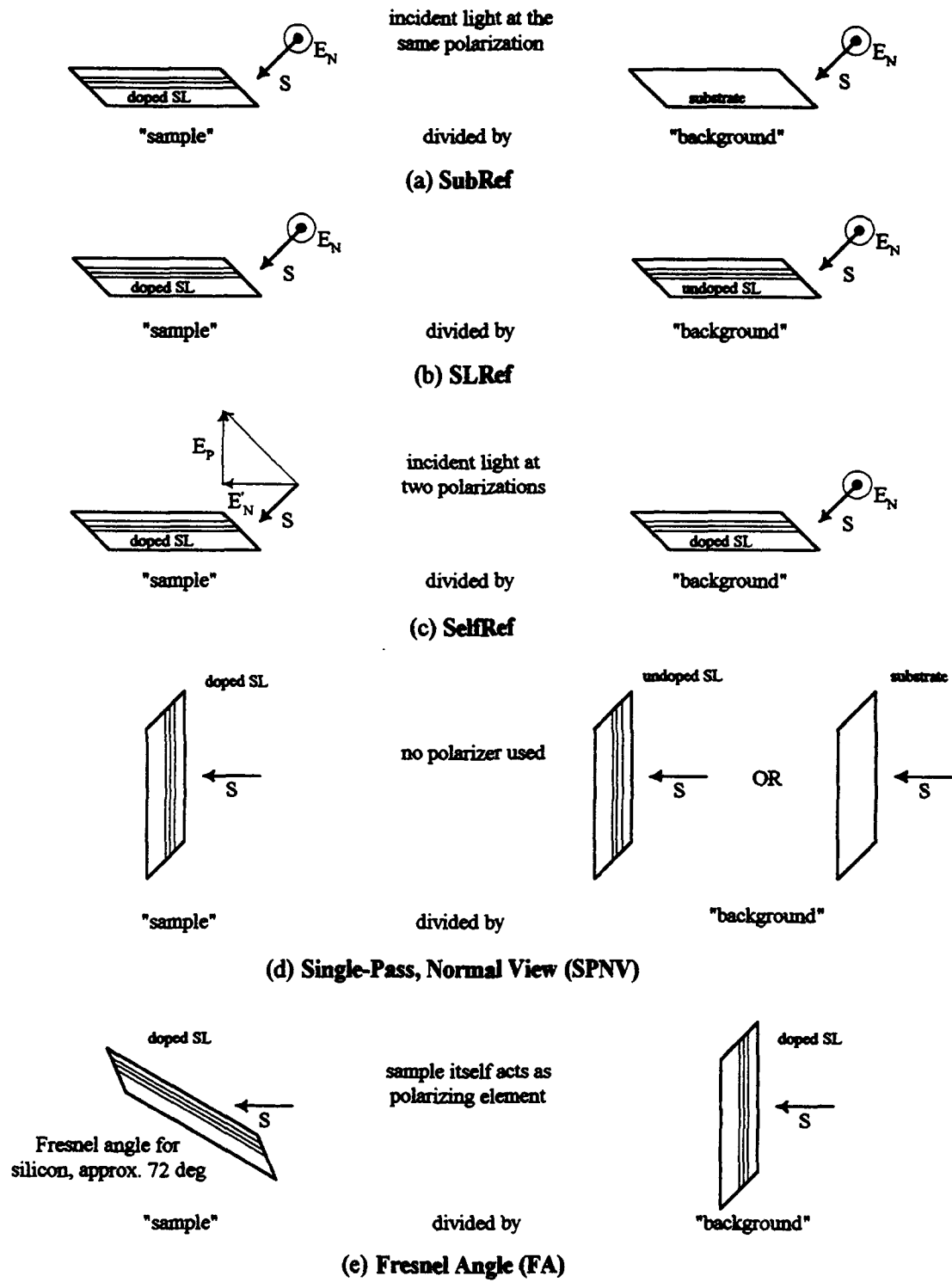


Figure 27. Various background subtraction techniques used in this study.

quantum plane, \vec{E}_p , as in Figure 27(b), the vector lies along the growth (z-) axis and may be referred to as parallel incidence light.

In the SubRef technique, a doped SL sample, fashioned into a waveguide, was mounted in the test chamber and the polarizer is rotated to a specific setting. A single-beam spectra was taken and stored as I_{sample} . Next, a substrate waveguide was placed into the FTS system and another spectra was taken at the same polarizer setting. This single-beam spectra is considered $I_{background}$. The SLRef technique is procedurally the same, except an undoped SL sample was used, when available, as a "truer" background spectrum.

The SelfRef technique was even simpler to perform. In this case, a doped SL sample was mounted as before and a single-beam spectra taken at one polarization setting. Next, without disturbing the sample in any way, the polarizer was rotated to another setting and a second single-beam spectra taken. Either of these two spectra were defined later as I_{sample} or $I_{background}$, depending on how the data was interpreted. The underlying principle supporting the SelfRef technique is that since Si is a cubic material, the spectra taken at one polarization should be no different than the spectra taken at another polarization. Therefore, the only spectra that remains using this background subtraction technique should be that attributed to the superlattice alone, which should show distinct absorption preferences for one polarization over another.

Initially, the raw data obtained using the Sub/SLRef and SelfRef techniques looks very different. This difference primarily lies in how free-carrier absorption is interpreted when the electric field vector lies on the quantum plane. However, after proper interpretation and background leveling, these two background subtraction techniques actually provided very similar results. Although the Sub/SLRef technique is more straightforward conceptually, the SelfRef technique has the distinct advantage of not

requiring a separate background sample to grow, prepare, and mount. In addition, the SelfRef technique also appeared to provide a slightly enhanced signal intensity and resolution.

The single-pass, normal view (SPNV) technique shown in Figure 27(c) is the most straightforward technique, yet provides questionable results for this application. In this case, as in the SubRef and SLRef techniques, a single-beam spectra of a doped SL sample was taken and directly compared with the spectra taken from either a substrate or undoped SL sample. This technique does not require the sample to be cut into a waveguide and does not require a polarizer or focusing optics in the beam path. In addition, signal throughput would typically increase by a factor of 4-5 while using this technique (after accounting for the absence of focusing optics and transmission losses) since a full circle of transmitted light could be collected from the backside of the normally-incident sample rather than a thin rectangle of light from the waveguide facet. However, this technique does not allow one to study the polarization dependence of the quantum plane which is fixed normal to the incident light. Furthermore, this technique permitted two separate etalon effects to occur which distorted the data in two ways.

First, if FTS resolution was set to 4 cm^{-1} (wavenumbers) or better (fewer wavenumbers), then very high-frequency, high-amplitude fringes would develop at shorter wavelengths using the SPNV background subtraction technique. High-frequency fringes occurred from 2 to $9 \mu\text{m}$ with sample thicknesses of approximately $0.28 \text{ mm} \pm 0.02 \text{ mm}$. These high-frequency oscillations completely masked the underlying absorption spectra. As the fringes diminished at longer wavelengths, one could observe that they did, in fact, "ride" the underlying spectra but continued to obscure sharp features. This type of fringing was mitigated by canting the sample 20-30 degrees from normal incidence, and later, decreasing resolution to 8 cm^{-1} .

A second thin etalon effect was also observed in all heavily-doped samples using the SPNV technique after decreasing resolution. In this case, a thin etalon which formed between the incident (top) surface and the last, doped-epilayer/buffer-layer interface caused an optical interference effect which appeared as an absorption peak. A plot of this phenomena and a detailed explanation for this effect is given in a later section. After the results from the SPNV technique were determined to be unreliable, this background subtraction technique was abandoned. Note however, this is still a perfectly sound subtraction technique for many, if not most, absorption applications. However, one must be very careful when using this technique with thin, highly specular, crystalline samples and coated optical elements.

Finally, the Fresnel Angle technique shown in Figure 27(d) is similar to the SPNV method, but employs the sample itself as a polarizing element. In this case, the same sample was used in both the sample and background runs, as in the SelfRef technique. The sample was rotated in azimuth to the material's Brewster angle and the single-beam spectra, I_{sample} was taken. Next, the sample was returned to normal incidence and $I_{background}$ was taken. This technique allows only the transverse magnetic (TM) mode of incident light to pass through the sample which has a component of the electric field vector perpendicular to the quantum plane. Unfortunately, the Fresnel technique was only effective with the relatively strong, direct-gap absorption transitions found in the InGaAs/AlGaAs samples. This technique was totally ineffective for all SiGe materials.

Selecting the FTS software to acquire single-beam spectra rather than computing straight absorbance had distinct advantages that should be mentioned here. A single-beam spectrum is the most pristine data set one can acquire just after a Fourier transform is taken of the digitally recorded interferogram. If one chooses to compute and display an

absorbance or transmission spectra, then one must immediately measure and select a background reference in the lab and run the computation. Once the absorbance file is computed, the original single-beam spectrum of the sample is overwritten. By *not* computing an absorbance file, and instead, building a library of single-beam spectra, various background reference scenarios can be investigated by selecting any single-beam spectrum as a reference and computing the absorption spectra at some later time. In this study, over 1800 single-beam spectra were collected and cataloged.

This concept of collecting and storing data in its most raw and unprocessed form can be taken even one step further by collecting only the interferogram just *before* the Fourier transform. In this case, additional interferograms can then be taken later and "co-added" to the original data set to increase SNR; however, the data must eventually be Fourier transformed. (Due to linearity, the intensity spectra obtained after the Fourier transform may also be co-added; however, this capability is not featured in the BioRad software.) Since resolution may increase significantly by choosing different apodization functions as part of the transform, this method does provide a distinct advantage in that the original interferogram, taken before the transform, is preserved. After the transform is completed, absorption or transmission files must still be computed for a spectrum.

Peaks Observed at 3-5 microns Using SPNV Subtraction

When heavily doped samples were examined using the single-pass, normal view background subtraction technique, a single, broad, rounded peak was observed in the 3 to 5 μm region (see Figure 28). These results were first seen by Misrah and Greve at Carnegie-Mellon University (CMU) who first believed these peaks were attributed to quantum well phenomena. The CMU results were later confirmed at AFIT using the SPNV background subtraction technique on the original CMU samples and additional

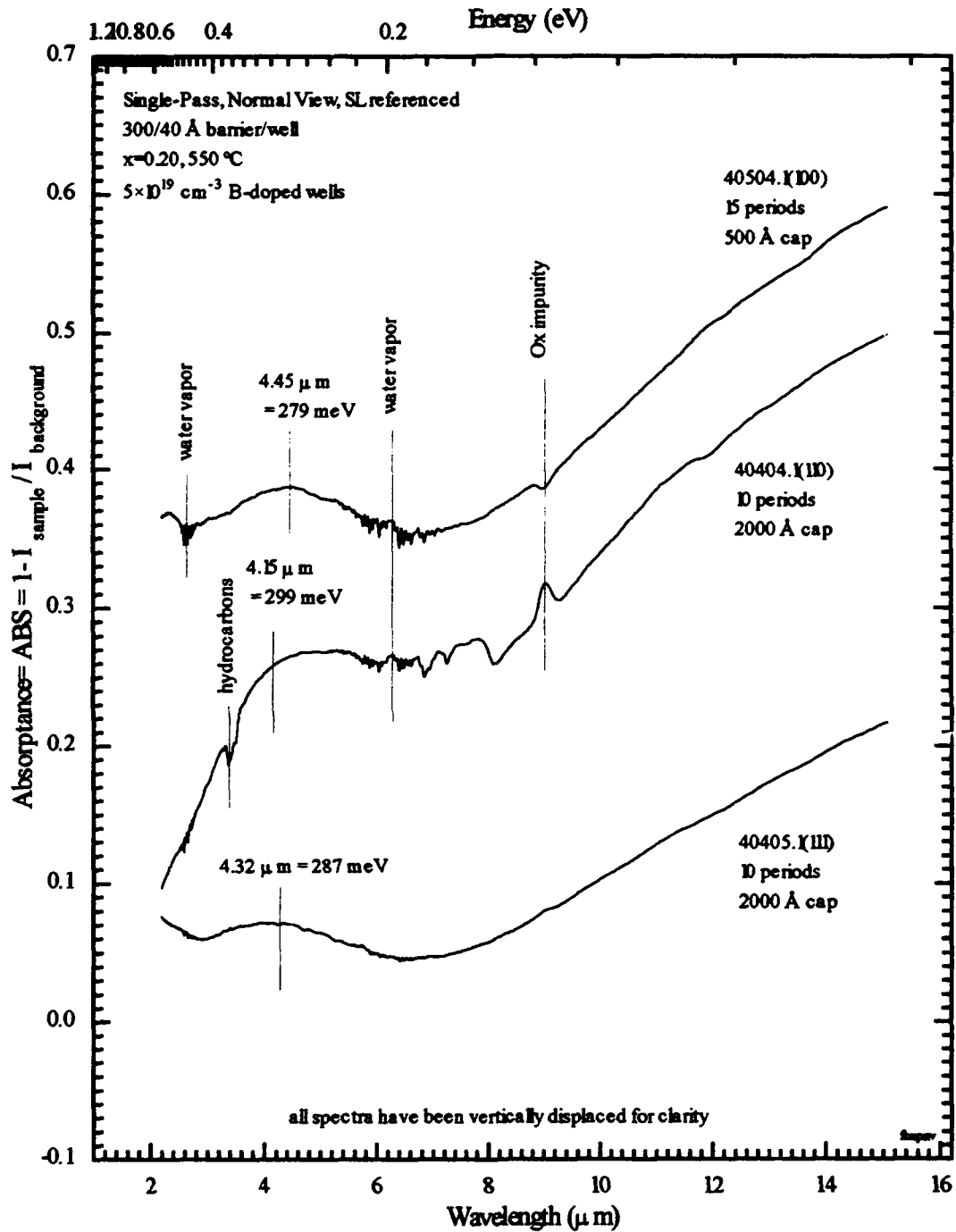


Figure 28. FTIR absorption data of similar SL structures on different substrate orientations in single-pass, normal-view mode.

samples provided by NRL. Later however, CMU reported to AFIT that these peaks exhibited a blue shift to shorter wavelengths when the cap layer was etched from the samples, which in effect, decreased the "etalon width". The blue shift was also confirmed after re-examining absorption data taken from several NRL samples with different cap thicknesses and periods. Peak values reported in Figure 28 were measured after background leveling.

In the case of thin film or etalon effects, the fraction of transmitted light incident upon the sample may be expressed as

$$\frac{I_t}{I_i} = \frac{(1-R)^2}{(1-R)^2 + 4R \sin^2(\delta/2)}, \quad (9)$$

where R is the fraction of the light intensity reflected at each surface, and δ is the phase angle delay,

$$\delta = \frac{4\pi\eta d \cos\theta}{\lambda}.$$

From Eq(11), the transmission is unity when

$$\delta = 2m\pi, \quad (10)$$

for any integer, m (see Figure 29). Then

$$2m\pi = \frac{4\pi\eta d \cos\theta}{\lambda}.$$

Setting $m=1$ and assuming normal incidence ($\theta=0$), then

$$\lambda_{\max} = 2\eta d. \quad (11)$$

Note that the maximum transmission may be interpreted as minimum absorption from the relation

$$ABS = 1 - \frac{I_t}{I_i}.$$

From inspection, the minimum transmission (which may, in turn, be interpreted as maximum absorption) occurs when

$$\delta = 2(m + 1/2)\pi ,$$

which drives the \sin^2 term to unity for any m , thus minimizing transmission. Since this expression occurs with the same periodicity as Eq(10) within the same free spectral range, Eq(9) may also be used to determine the same conditions for maximum absorption. Therefore, assuming the index of refraction is unchanged, the absorption peak will "blue shift" (to higher frequencies or shorter wavelengths) when the etalon spacing, d , is decreased. Conversely, if the etalon spacing increases, the apparent "absorption" peak will "red shift" to longer wavelengths.

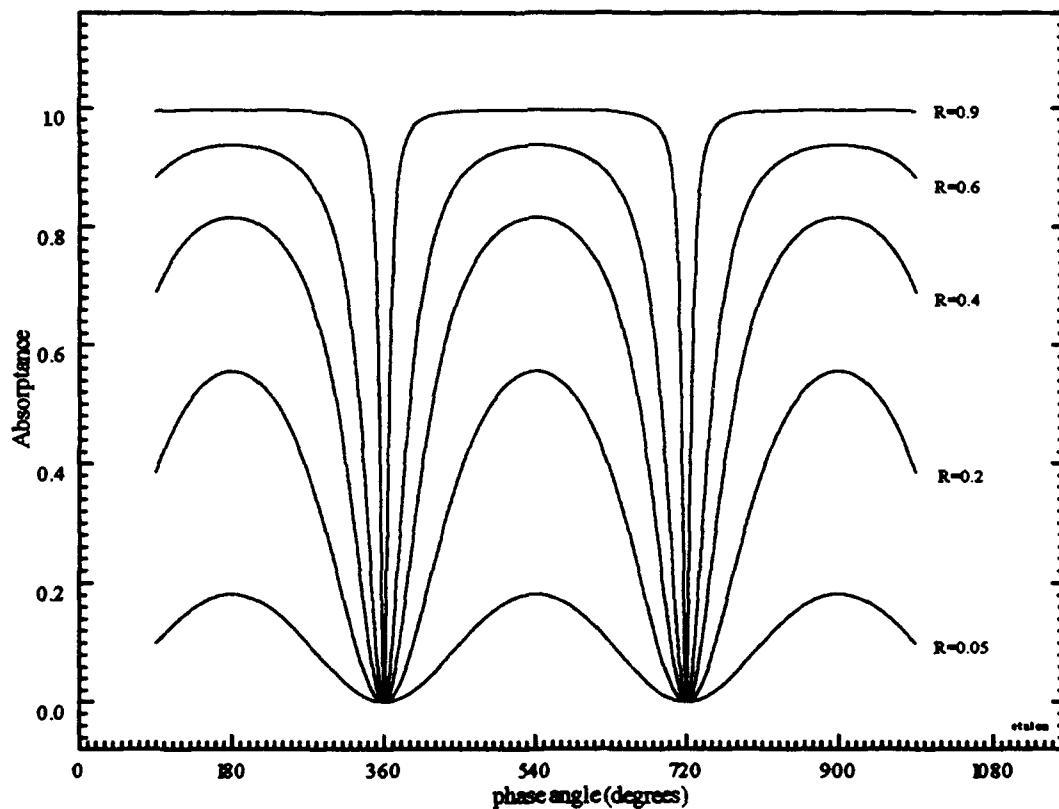


Figure 29. Plot of Eq(9) illustrating phase angle effects of an etalon.

Signal-to-Noise Ratio Analysis

Taking absorption data from small semiconductor waveguides mounted on edge pushed the capability of the BioRad FTS-60A to its outer operational limits. Several questions quickly arose during initial runs such as, "Can we see the true signal?" and "How many scans will be necessary to reduce the statistical noise in the signal?" To answer these questions a series of experiments were conducted over several days and nights to gather statistical evidence.

Every measured response of an optical detection system, such as the FTS, records a signal and its associated noise:

$$m(\lambda) = s(\lambda) + n(\lambda) ,$$

where $m(\lambda)$ is the measured response as a function of wavelength, $s(\lambda)$ is the signal, and $n(\lambda)$ is the total noise of the system. The signal-to-noise ratio of an optical system may be defined in statistical terms as

$$SNR = \frac{\text{mean value of the measured response}}{\text{standard deviation of the measured response}} .$$

The mean, \bar{k}_i , is defined

$$\bar{k}_N = \frac{1}{N} \sum_{i=1}^N k_i = \langle k \rangle ,$$

where N is the total number of events, and k_i are individual measurements. In the case of the FTS measurements, N , is the number of scans, while k_i represents the measured response of the detector as a function of wavelength (actually wavenumber) on the i th scan. Practically speaking, k_i is a discrete number loaded into one cell of the data file. Another term for the mean is the expected value, or $\langle k \rangle$. The standard deviation is defined

$$\sigma(\lambda) = \sqrt{\frac{\left(\sum_{i=1}^N k_i^2\right) - N \cdot (\bar{k}_N)^2}{(N-1)}} .$$

Then to determine the SNR as a function of wavelength in this experimental condition, we must first compute the mean of the measured response, or

$$\langle m(\lambda) \rangle = \frac{1}{N} \sum_{i=1}^N m_i(\lambda) ,$$

where

$$m_i(\lambda) = s_i(\lambda) + n_i(\lambda) .$$

Then

$$\langle m(\lambda) \rangle = \frac{1}{N} \sum_{i=1}^N [s_i(\lambda) + n_i(\lambda)] .$$

Assuming the true signal is unchanged for each scan and the measured response fluctuates only as a function of random system noise, then $s(\lambda)$ may pass directly through the averaging sum, leaving

$$\langle m(\lambda) \rangle = s(\lambda) + \frac{1}{N} \sum_{i=1}^N n_i(\lambda) .$$

Truly random statistical noise has a zero mean, then

$$\langle n(\lambda) \rangle = \frac{1}{N} \sum_{i=1}^N n_i(\lambda) = 0 ,$$

leaving

$$\langle m(\lambda) \rangle = s(\lambda) .$$

In other words, the mean value of the measured response is the signal—the numerator in the signal-to-noise ratio.

Next, consider the standard deviation. The standard deviation measures the statistical spread of the data (measured response) from the mean value (true signal). Once again, practically speaking, one may think of it as the average peak value associated with system noise as measured from the true signal in a spectra. This is a very important metric to quantify in very low-light level spectroscopy since it would be very difficult to identify

an expected peak if it is the same scale as the noise of the measured response. Using the definition of the standard deviation given earlier, the system SNR for N scans is the following:

$$SNR_N = \frac{\frac{1}{N} \sum_{i=1}^N k_i}{\sqrt{\frac{\left(\sum_{i=1}^N k_i^2 \right) - N \cdot (\bar{k}_N)^2}{(N-1)}}}$$

To determine the number of scans, one must first assume the system noise is uncorrelated—which is almost always true in nature—then the variance of the system noise may be defined as

$$\begin{aligned} \langle n_i(\lambda) n_j(\lambda) \rangle &= 0 && \text{for } i \neq j, \\ &= \sigma^2 && \text{for } i = j, \end{aligned}$$

or

$$\langle n^2(\lambda) \rangle = \sigma^2(\lambda).$$

which is the standard deviation squared. The variance of the noise term is then

$$\text{var} \left\{ \frac{1}{N} \sum_{i=1}^N n_i(\lambda) \right\} = \left\langle \frac{1}{N^2} \sum_{i=1}^N \sum_{j=1}^N n_i(\lambda) n_j(\lambda) \right\rangle.$$

Since the expectation and summation expressions are linear operators, they may be interchanged. The previous expression then reduces to

$$\begin{aligned} \text{var} \left\{ \frac{1}{N} \sum_{i=1}^N n_i(\lambda) \right\} &= \frac{1}{N^2} \sum_{i=1}^N \sum_{j=1}^N \langle n_i(\lambda) n_j(\lambda) \rangle \\ &= \frac{1}{N^2} \sum_{i=1}^N \sigma_i^2(\lambda) \\ &= \frac{1}{N} \sigma_i^2(\lambda). \end{aligned}$$

Returning to the original definition of SNR

$$SNR = \frac{\text{mean}}{\text{standard deviation}}$$

$$= \frac{\text{mean}}{\sqrt{\text{variance}}}$$

Then

$$SNR = \frac{\bar{k}_i}{\sqrt{N} \cdot \sigma}$$

leaving

$$SNR_N = \sqrt{N} \cdot SNR_1$$

Figure 30 shows the results of a SNR data analysis for the BioRad FTS-60A FTIR system using samples in the SPNV and waveguide configurations. The polarizer and associated condensing optics were included in the beam train when applicable. In this case, 256 single-beam spectra were recorded as individual data files. From the figure, the statistical analysis of this data as a function of wavelength indicates that $SNR_N \approx 10,000$ for the SPNV configuration and $SNR_N \approx 50$ for the waveguide configuration. Considering (1) the illuminated, circular area of the sample, as seen by the detector is 3-4 times greater than the narrow rectangular area of the sample edge in the waveguide configuration, and (2) no polarizer contributing to transmission loss is used in the SPNV configuration, one would expect the SNR to be greatly improved in the SPNV mode. Using the results from the more demanding, waveguide configuration case:

$$SNR_1 = \frac{SNR_N}{\sqrt{N}} = \frac{50}{\sqrt{256}} = 3.125$$

Then, to boost SNR five-fold

$$N = \left(\frac{SNR_N}{SNR_1} \right)^2 = \left(\frac{5 \cdot 50}{3.125} \right)^2 = 6,400 \text{ scans}$$

Therefore, for this given experimental configuration, to increase system SNR by a factor of five over existing noise levels, the FTIR spectrometer should be set to co-add 6,400 scans. Given typical optical resolution of 8 cm⁻¹ (recall that higher resolution increases the number of data points), a 6400-scan run would take approximately 75 minutes.

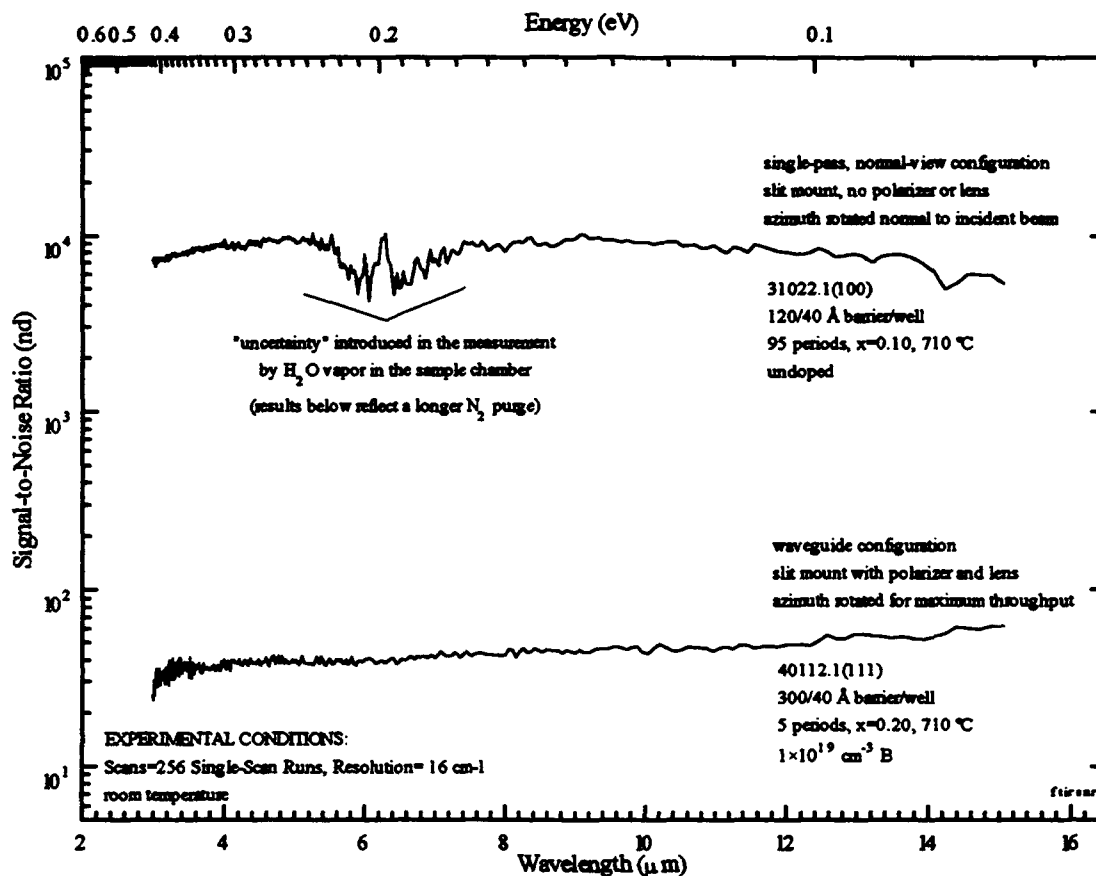


Figure 30. SNR data analysis for FTIR system using SPNV and waveguide configurations.

IV. Results and Discussion

Confirmation of Photoluminescence Emission from the Superlattice

PL emission from the superlattice was confirmed by first examining emission spectra from (100), (110), and (111) Si substrates and then examining spectra taken after superlattice epitaxial layers were grown on each substrate. All PL spectra reported in this study were taken with an Ar⁺ laser operating in multi-mode with a predominant source illumination at 4880 Å at 60 mW. Typical optical power density on the sample is estimated at 0.6 W/cm². The entrance and exit slits of the dispersive monochromator were each set to 600 μm providing a 12.3 Å spectral resolution. Except for studies requiring the sample temperature to vary, all spectra were taken at a sample temperature of 3 K.

PL spectra from three Si substrates is shown in Figure 31. In this figure, it is possible to resolve five possible peaks related to boron no-phonon and phonon replica emission from the Si substrates alone. The dominant peak at 1.093 eV has been identified⁹⁷ as a boron-related bound exciton emission whose downward transition is assisted across the indirect gap by transverse-optical and longitudinal-optical phonon emission, i.e., B:BE(TO,LO). In this case, the B:BE(TO,LO) is associated with boron impurities which *unintentionally* enter the substrate crystal system during the Si boule growth process. This peak should not be confused with boron acceptors which were *intentionally* doped in the VB well in subsequent studies.

The boron peaks were also observed after a superlattice structure was grown on the substrate, even though the Ar⁺ excitation source could only penetrate 0.5 μm to approximately the middle of the buffer layer. During MBE growth, residual boron and other background impurities from the chamber diffuse to the sample and lodge in the Si

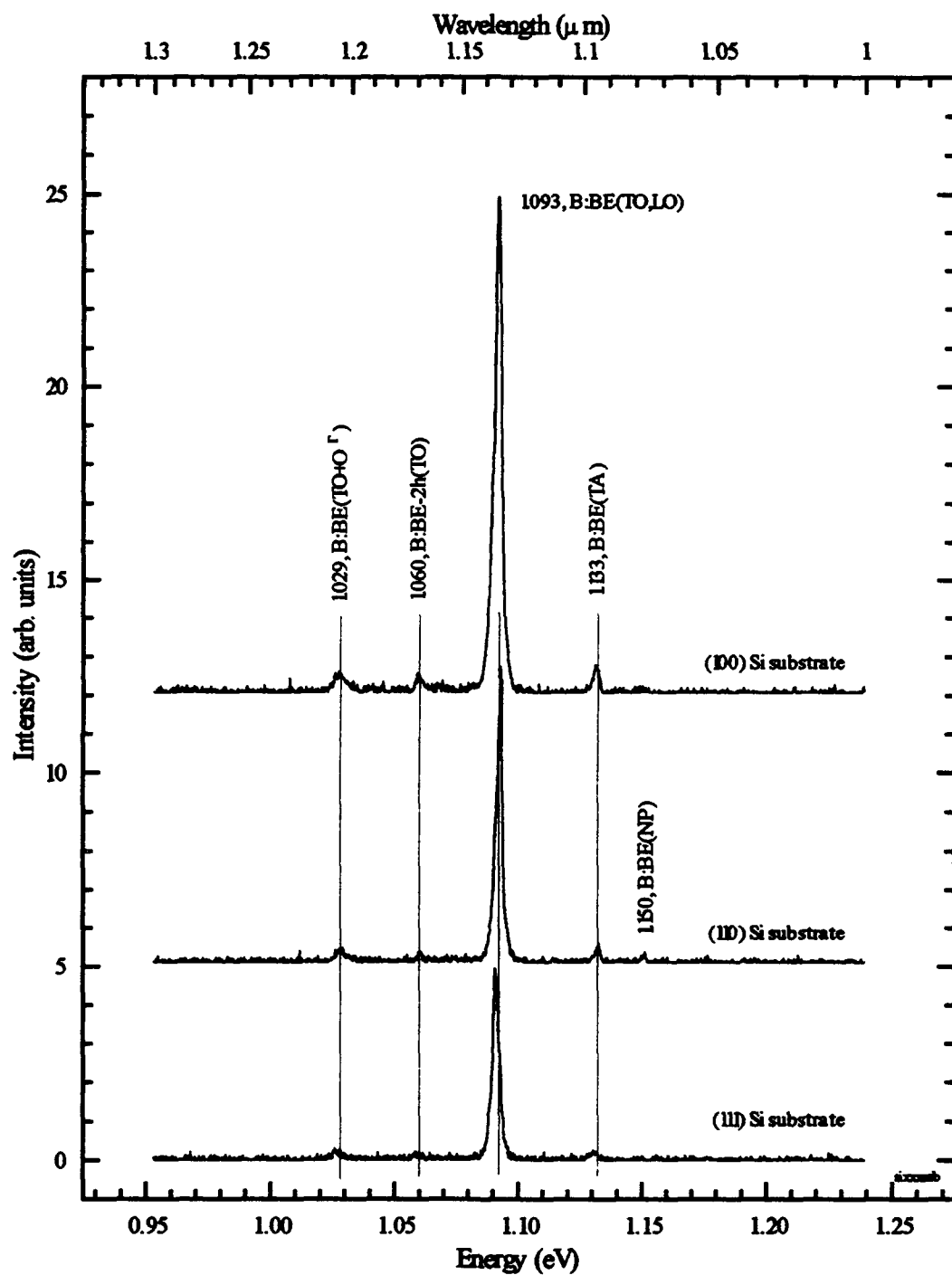


Figure 31. PL spectra from (100), (110), and (111) silicon substrates.

buffer, barrier, well, and cap layers. Secondary ion mass spectrometry (SIMS) performed at the National Institute of Standards and Technology measured background impurities of boron (B^{11}), chromium (Cr^{52}), aluminum (Al^{27}), and tantalum (Ta^{181}). A plot of background impurities is shown in Figure 32 for a 10-period $Si_{0.8}Ge_{0.2}/Si$ superlattice grown at 550 °C on a (110) Si substrate. In this sample, boron was intentionally doped in the SiGe alloy wells at very high levels, $8 \times 10^{19} \text{ cm}^{-3}$, to provide an excess of free holes for absorption measurements.

The B:BE(TO,LO) peak was a predominant peak and served as a landmark feature in tuning the PL system. Peak intensity changed with each substrate in Figure 31, however, note all other peaks changed a proportional amount. This overall change in signal strength was attributed to slight differences in optical alignments, etc., from measurement to measurement. The FWHM of BE(TO,LO) ranged from 3 to 6 meV indicating a sharp transition from a well-defined impurity level. The binding energy of an exciton to boron is approximately 4 meV.⁹⁷ Absorption data from earlier work reports a boron ionization energy of 38–40 meV above the valence band edge.⁹⁸

The remaining boron peaks were very weak and have been identified by Dean *et al.*⁹⁹ to other combinations of transverse-optical and -acoustic phonon-assisted transitions. The B:BE(TA) is a transverse-acoustic phonon assisted transition of an exciton bound to boron. The B:BE(TO+O Γ) peak is a transverse-optical plus zone center optical phonon transition of an exciton bound to boron. The B:BE-2h(TO) peak was ascribed to the decay of a bound exciton leaving a hole on a neutral acceptor in an excited state and is referred to as a two-hole transition. The weaker boron-related peaks were normally not observed in the presence of a strong superlattice peak emission. All observed boron-related peaks are summarized in Table IX.

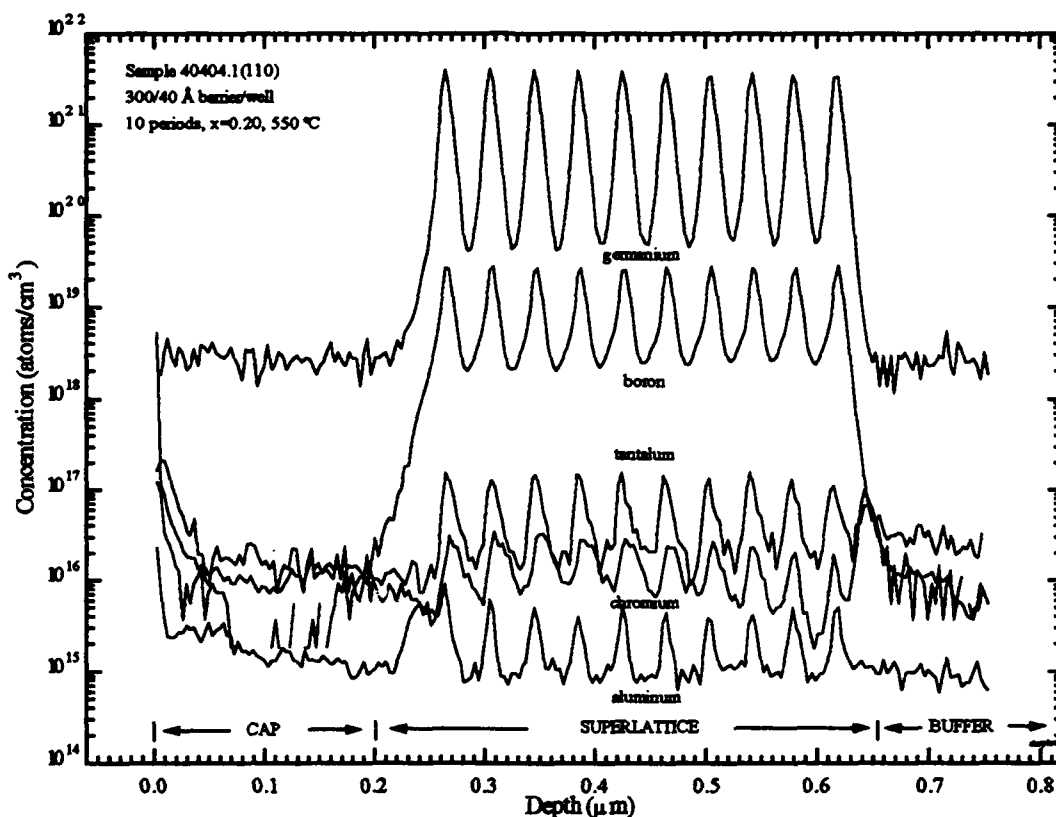


Figure 32. SIMS plot of a SiGe superlattice grown at 550 °C on (110) Si.

Table IX. PL emission peaks due to boron impurity in Si substrates.

energy (eV)	identification	comments
1.150	BE(NP)	very weak, rarely observed
1.133	BE(TA)	weak
1.093	BE(TO,LO)	very strong, ≤ 6 meV FWHM
1.060	BE-2h(TO)	weak
1.029	BE(TO+O ⁻)	weak

The PL spectra shown in Figure 33 are significantly different than the earlier figure and is the result of emission from a superlattice structure grown atop a (100) Si substrate. The B:BE(TO,LO) remains at 1.093 eV, however, it is now joined by superlattice-related no-phonon and phonon-replica pair emissions. The superlattice structure has a Si barrier 300 Å thick along with an undoped SiGe alloy 40 Å well in the valence band. This was repeated 5 times. The Ge composition ranges from 20-50% in 10% increments. The sample was grown at 710 °C.

The superlattice-related bound exciton lines vary as a function of germanium composition and are denoted as X:BE(). The X:BE(NP) line is typically the dominant superlattice-related line and represents a transition from an exciton bound to a neutral impurity at an energy level near the CB to the first heavy-hole state of the VB well. As Ge composition increases, the valence band well offset increases causing interband transitions from CB to VB to shift to lower energies as the first heavy-hole state approaches closer to the CB. The next most predominant superlattice peak after the NP line is the TO_{Si-Si} phonon replica which had a consistent 58-59 meV offset from the NP line. At lower Ge compositions, such as $x=0.20$, the TA_{Si} was also observed offset approximately 18 meV from the NP line. At $x=0.40$, the TO_{Si-Ge} line is barely resolved in Figure 33 at 49 meV from the NP line. The TO_{Ge-Ge} peak, offset at 34 meV from the NP line was never observed in the relatively limited sample set used in this study. Table X lists the phonon-related transitions which have been observed in SiGe superlattices as measured from the predominant no-phonon (NP) line. The relative intensities of the no-phonon/phonon-replica (NP/pr) peaks and the boron BE(TO,LO) reference peak remain consistent with the exception of the spectrum for $x=0.30$. In this case, the boron line decreases to the same height as the NP line while the TO_{Si-Si} rises significantly. In addition, as Ge increases, the NP/pr emission lines broaden considerably from 5 meV at $x=0.20$ to

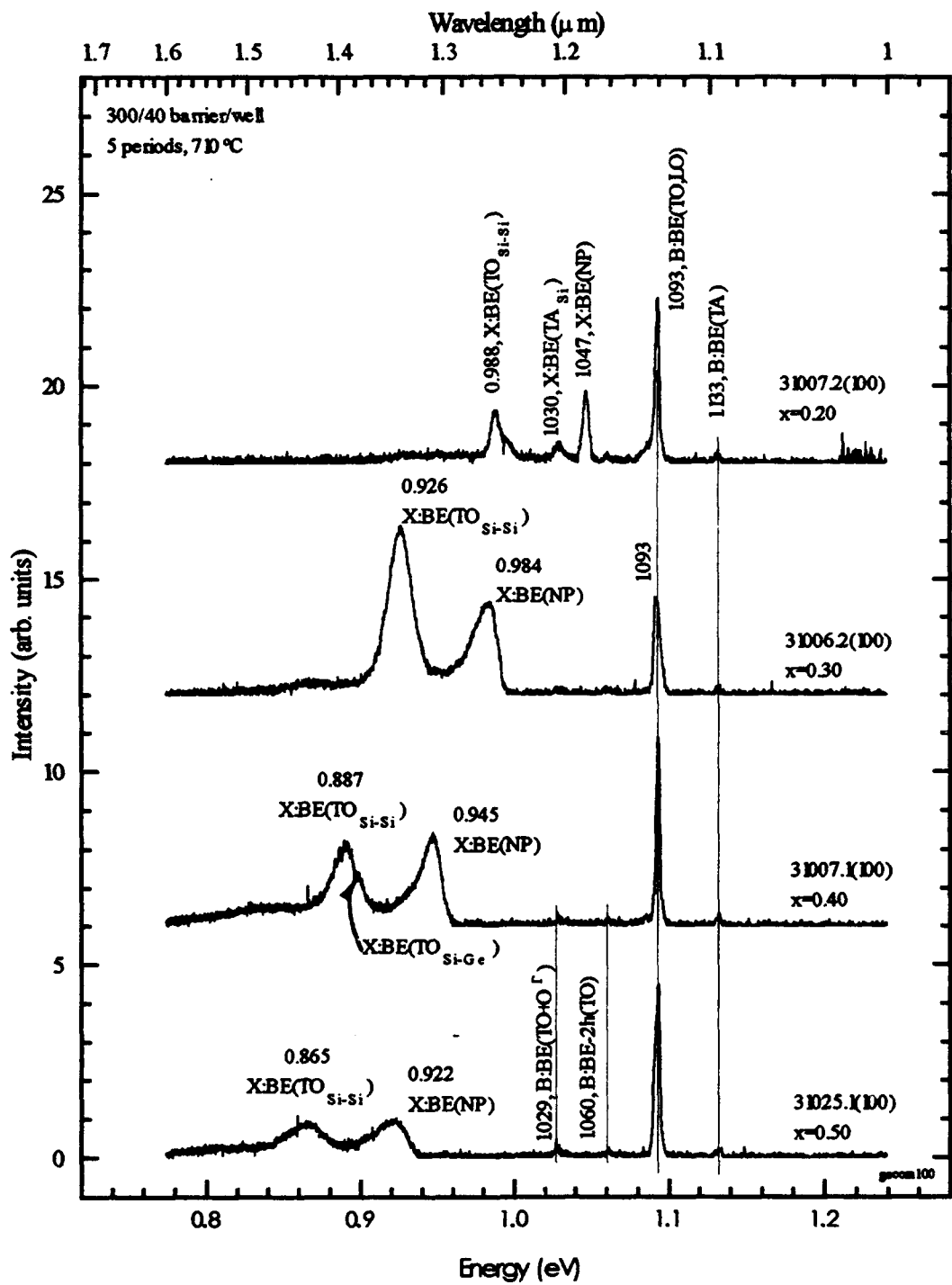


Figure 33. PL spectra of undoped SiGe superlattices as a function of Ge composition.

Table X. Identified phonon-assisted transitions measured below the no-phonon line. For example, if the NP transition occurs at 1.083 eV the TO_{Si-Si} occurs at 1.025 eV.

phonon replica	energy (meV)
TA_{Si}	18
TO_{Ge-Ge}	34
TO_{Si-Ge}	49
TO_{Si-Si}	58

approximately 20 meV for $x=0.30, 0.40,$ and 0.50 . This broadening was attributed to increased SiGe alloy scattering as Ge composition increased. As the FWHM increases, the less significant TO_{Si-Ge} and TA_{Si} emission peaks are completely enveloped and can no longer be resolved.

Effects of Growth Temperature on PL Emission

Sample growth temperature had a profound effect on PL emission from superlattice-related peaks. The PL spectra shown in Figure 34 was taken from superlattices grown with similar structures at different growth temperatures. The structures consisted of 5 or 10 periods of 300 Å Si barriers with undoped 40 Å SiGe wells. The Ge composition remained fixed at $x=0.20$ for all samples. The sample growth temperature ranged from 550-850 °C in 50 °C increments.

The boron BE(TO,LO) line is apparent in all six samples. However, PL emission attributed to superlattice NP/pr lines is nonexistent at lower growth temperatures and abruptly appears at and above 700 °C. This may be attributed to the segregation of trace impurities to the top surface of the wafer during the low-temperature growth. Although the deposition rate remained constant at 0.625 Å/sec for the SiGe alloy and 0.5 Å/sec Si epilayers, the lower temperature allowed impurities, including some Ge, to segregate,

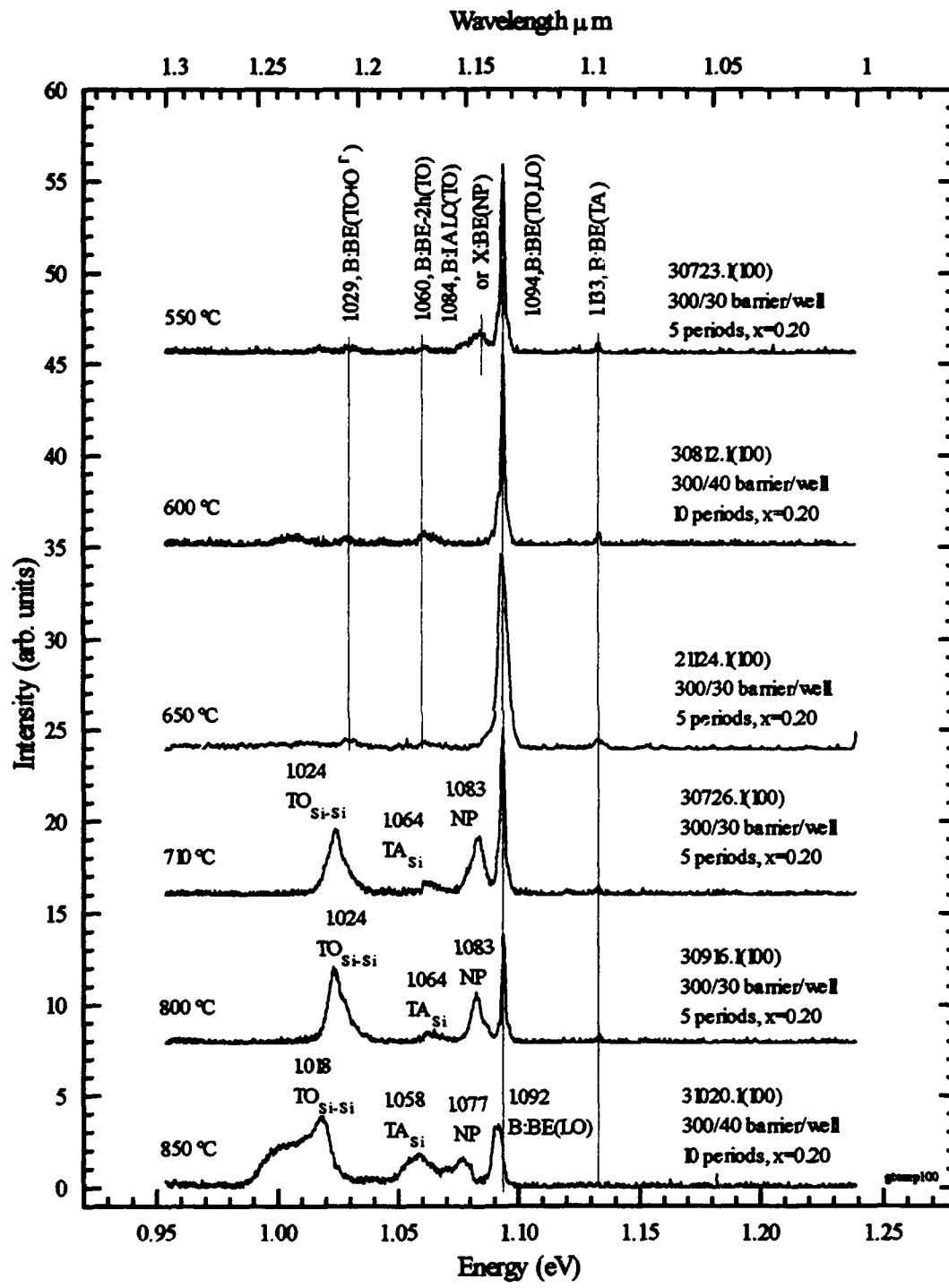


Figure 34. PL spectra of six SiGe (100) samples with similar superlattice structures grown at different substrate temperatures.

coalesce, and "bubble" to the top of the freshly deposited surface, much like the way oil separates from an oil/water emulsion and rises to the meniscus. This effect was first suspected after observing a slight haze on the wafer surface using 400× Nomarski optical microscopy, and further supported after observing evidence of Ge "islanding" from Transmission Electron Microscopy (TEM) studies on select samples for another study. This minority segregation may cause fewer radiative electron-hole recombinations in the wells eliminating PL emission from the superlattice.

However, above 710 °C, highly resolved PL emission from superlattice NP/pr pairs suddenly appears implying a better crystal has formed with fewer dislocations and less minority segregation. Two samples selected for 2×2 LEED indicated improved crystalline integrity with sharper interfaces at higher growth temperatures. Above 800 °C, however, the NP/pr emission begins to degrade: relative peak intensities shift, and peaks broaden 2-3 times their FWHM at growth temperatures of 710 °C. This degradation may be caused by the Ge itself now diffusing out of the well at the higher temperatures, effectively broadening the well and causing the interfaces to be less distinct. In addition, other impurities from the walls of the chamber itself may be deposited on the sample at these high growth temperatures, trapping charge carriers and creating competing radiative transitions.

Samples grown at 650 °C and below show the boron bound exciton lines mentioned earlier at 1.029, 1.060, 1.094 and 1.133 eV. A small peak at 1.084 eV can be seen which has been associated with multiple exciton phenomena and labeled "impurity associated localized carriers" (IALC), an all encompassing term adopted by Vouk and Lightowlers.⁹⁷ However, at 710 °C and above, the superlattice NP peak emerges, along with TO_{Si-Si} and TA_{Si} phonon replica peaks spaced 59 and 18 meV, respectively, from the NP line.

The PL spectra shown in Figure 35 was taken from similar structures grown at different growth temperatures on (110) Si substrates. In this case, only three samples grown at different growth temperatures were available yet the same trend may be seen. At 710 and 800 °C, the superlattice appears to be well formed with strong, narrow NP/pr peaks at the correct intervals. At 600 °C, the superlattice NP/pr peaks disappear leaving the boron-related phonon replicas and a single, broad peak at 0.936 eV. Once again, PL emission seems to be optimized at or near a 710 °C leading one to believe this is the best growth temperature for the best superlattice. To the best of my knowledge, this is the first report of SiGe superlattices successfully grown on a (110) Si substrate.

Although all the samples in Figures 35 and 36 were intended to have exactly the same structure with 300 Å barriers, 40 Å wells, and $x=0.20$; the NP line shifted 35 meV in the (110) case and 23 meV in the (111) case as the temperature changes from 710 to 800 °C. This shift is most likely caused by small changes in the growth conditions over a nine month time span rather than an effect related to growth temperature. Kronig-Penney calculations indicate that changes as small as 5% in Ge composition alone can cause the NP emission to shift as much as 30-40 meV. Discussions with NRL indicate that the Ge composition could drift 2-3% from week to week. After reviewing PL taken from samples over the past 18 months, the NP emission data remains consistent for samples grown within a period of several weeks but changed slightly over a period of several months. The NP-TO_{Si-Si} separation of 58 meV, however, is the clearest indicator of the existence of a SiGe superlattice using PL. This measure remained extremely consistent throughout the duration of the study.

The PL spectra shown in Figure 36 for a superlattice structure grown on (111) Si shows very similar behavior to the (110) case with only two minor differences: relative peak positions change only 5-7 meV, and the NP/pr peaks appear slightly more rounded with slightly greater FWHMs.

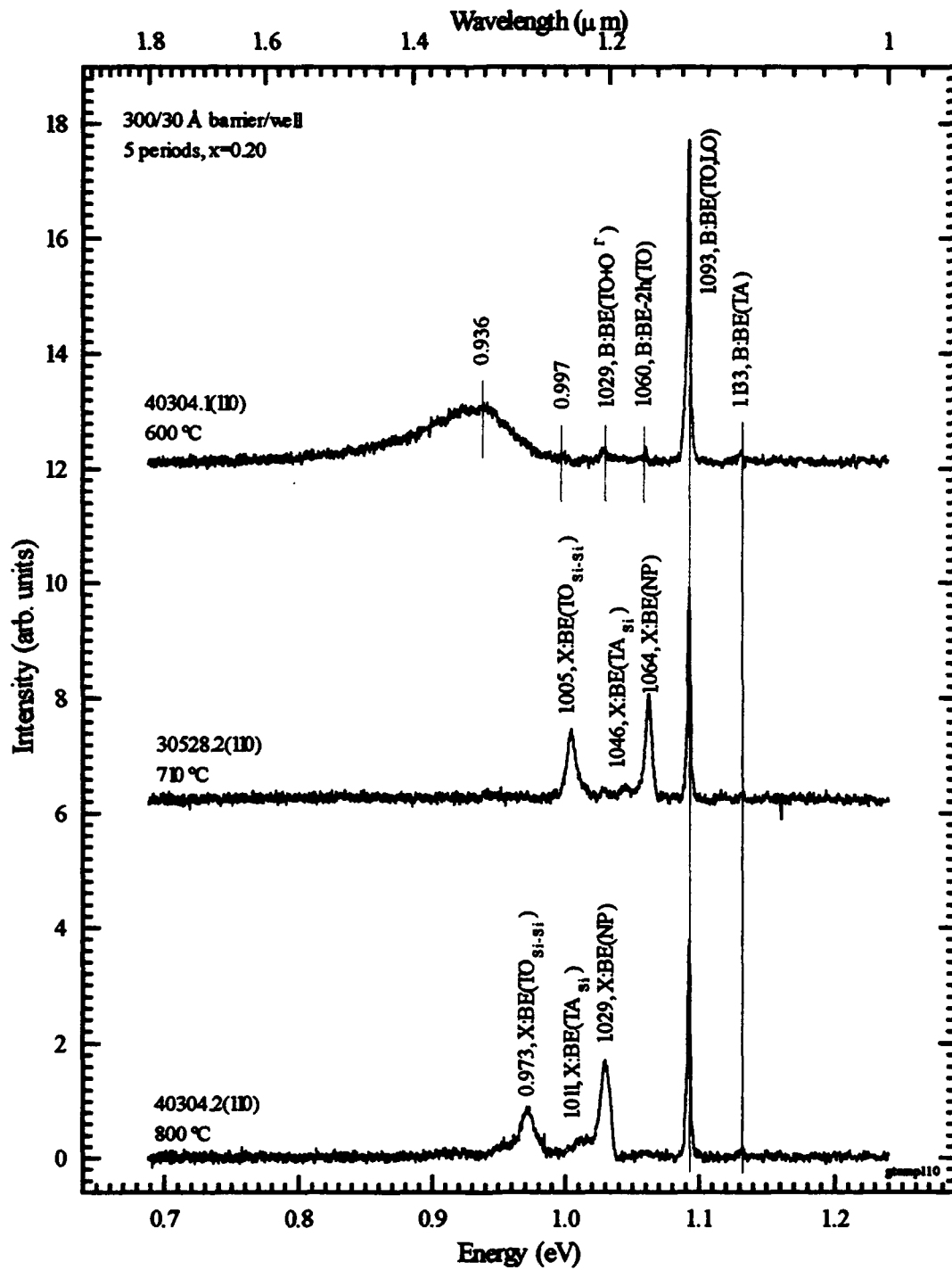


Figure 35. PL spectra of three SiGe (110) samples with similar superlattice structures grown at different substrate temperatures.

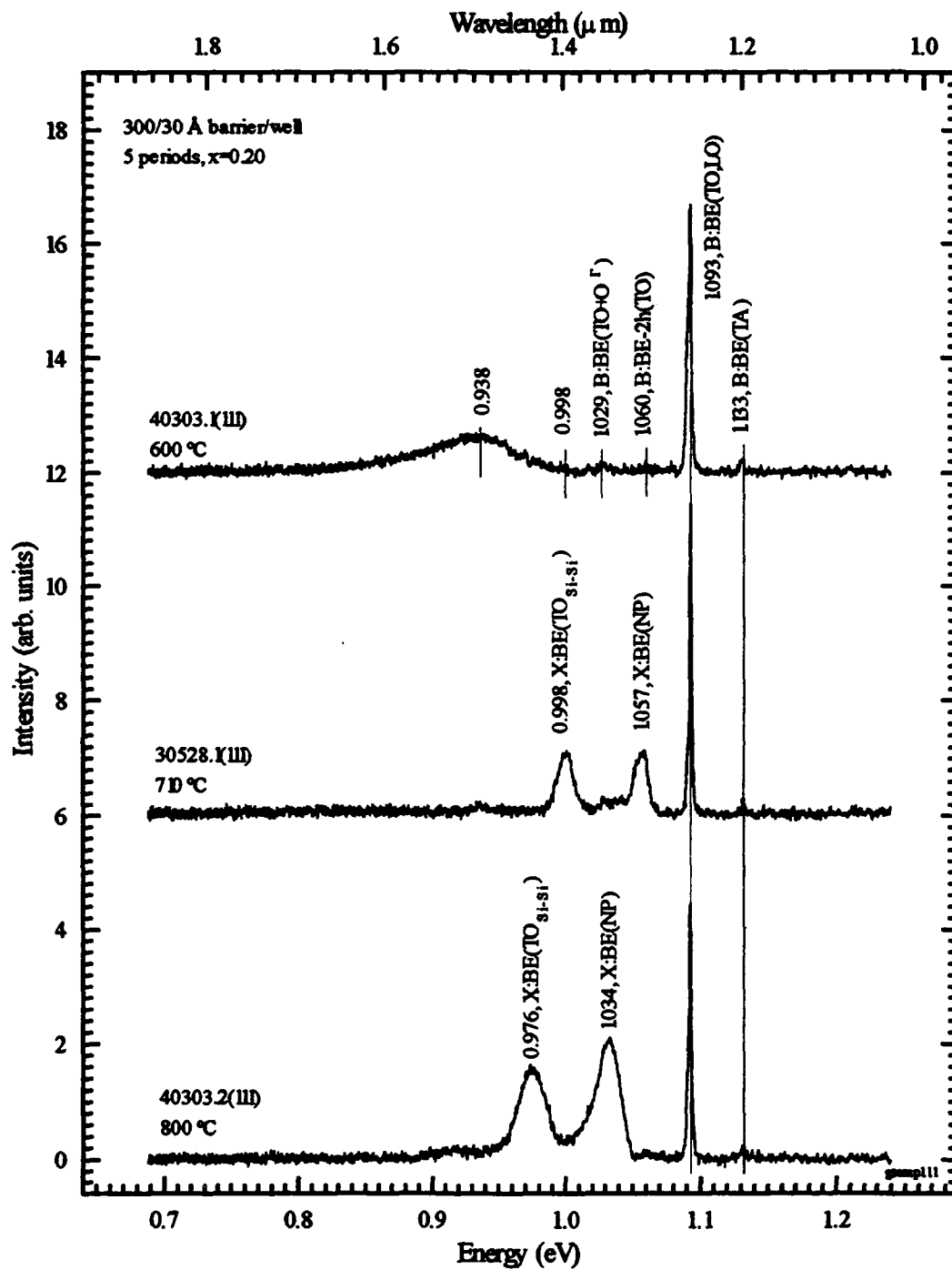


Figure 36. PL spectra of three SiGe (111) samples with similar superlattice structures grown at different substrate temperatures.

The dominant feature on the spectra of the low growth temperature samples observed on both non-conventional Si substrates is a strong, broad emission band at lower energies with a linewidth of 60 meV. A limited sample set did not allow this peak to be studied as a function of Ge composition or well width. However, several PL runs performed at different source power exhibit a weak dependence on excitation power densities. Another important feature of this peak is that the peak energy is approximately 100-120 meV below the expected bandgap of the strained alloy for a Ge composition of $x=0.20$.

There are three schools of thought which contribute toward the explanation of the broad-band emission peak found at low growth temperatures. In the first case, Sturm from Princeton,¹⁰⁰ reported a broad peak at low energies after implanting charged Si ions into bulk Si and attributed the radiative emission to excitonic recombination at damage sites in the crystal lattice. Although the peaks are similar, obviously this explanation does not apply in this study since these were not implanted with Si. In the second case, Noël from the National Research Council of Canada,¹⁰¹ attributed the reduced PL emission from the superlattice and the broad peak to Ge platelet aggregation which has been observed to increase slightly as the growth temperature is reduced in CVD grown samples. Ge platelet aggregation was confirmed in other (100) NRL samples using TEM; however, the broad PL was completely extinguished after the sample was annealed at 700 °C for one hour—with no reduction in the platelet density. In addition, Noël also reported significant platelet formation on samples grown at higher temperatures—significant enough to slightly broaden the FWHM of the NP/pr peaks associated with PL emission from the superlattice. Since sharp PL was observed in the NRL samples grown at 700 °C, and since platelets were not found on the (110) and (111) samples, Ge platelet formation alone cannot be considered the source of the broad peak at low energies.

The third case, first proposed by Glaser *et al.*¹⁰² at NRL, attributes the broad peak to donor-acceptor pair recombination from shallow impurities. SIMS on the samples in their study revealed the presence of B and Al (acceptors) along with Cr and Ta (donors) at the same levels as samples in our study, approximately 1×10^{16} atoms/cm³. Since measured ionization energies for these shallow donors and acceptors range from 40 to 70 meV, then the observed PL peak 100-120 meV below the strained alloy band gap can be accounted for by the difference in energy between the ionization energies located just below the CB and just above the first heavy-hole subband in the VB.

Effects of Sample Temperature on PL Emission

PL emission quickly diminishes as sample temperature increases on all three Si substrates. In all cases, PL spectra changed very little from 1.4 K, the coldest temperature obtained, to 3 K the typical PL experimental condition. However, from 3 K to 12 K, peak intensities would decrease significantly while FWHMs would remain approximately the same. PL emission could be observed at sample temperatures as high as 24 K at 60 mW laser excitation power, and up to 60-70 K after raising laser power to 300 mW.

In Figure 37, PL intensity as a function of sample temperature is shown for a typical superlattice structure grown on a (100) Si substrate. As temperature was increased from 3 to 12 K, the B:BE(TO,LO) emission line shifts slightly to higher energies and decreases by 30%. This 2-8 meV shift in this boron-related peak may be attributed to the selection from the bound exciton transition at 1.092 eV to the free exciton transition, FE(TO,LO), at 1.094 eV, and eventually to the free-electron to bound-hole (Fe-Bh) transition near 1.099 eV identified by Lightowlers.⁹⁷

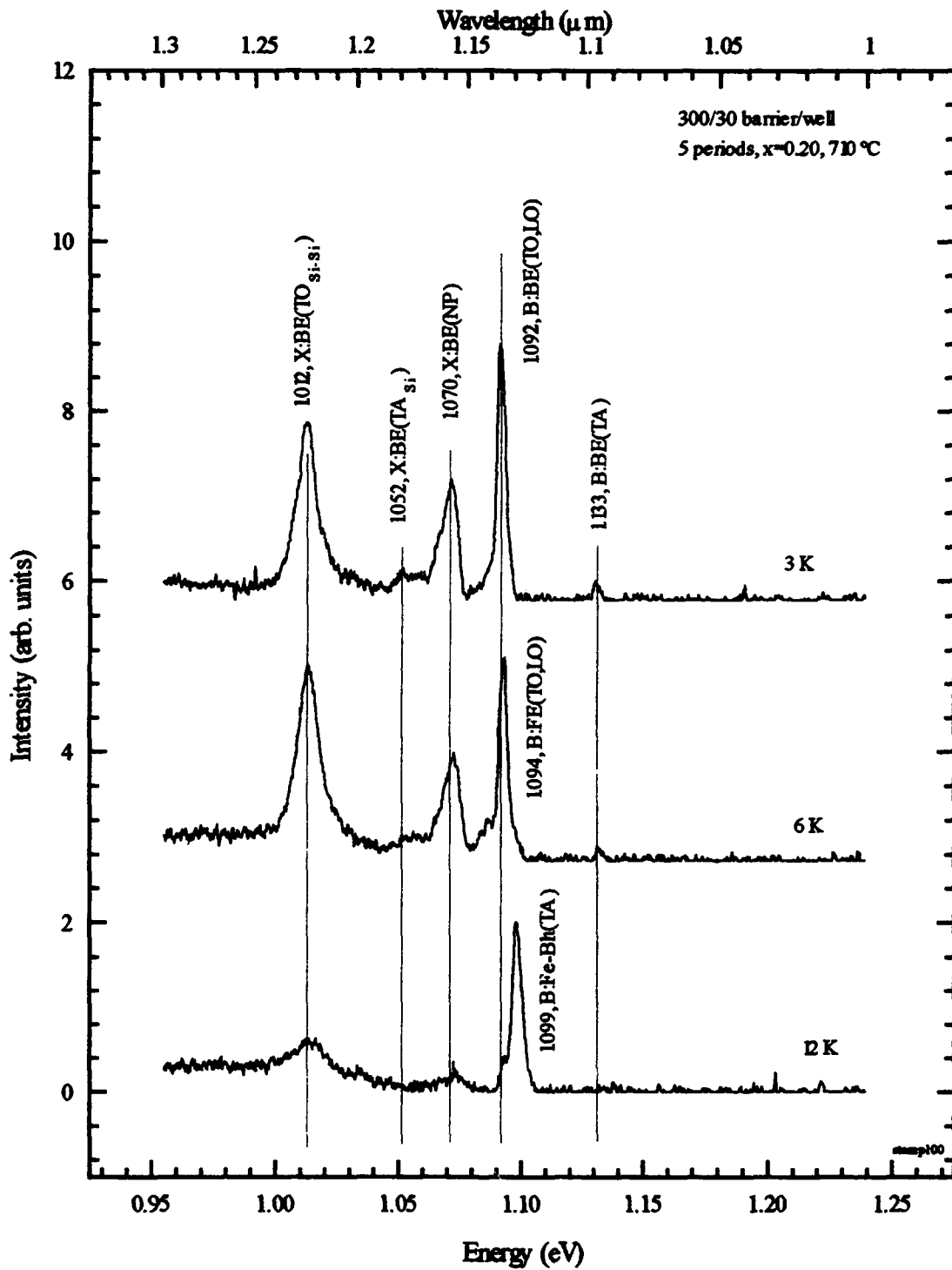


Figure 37. PL spectra of a (100) SiGe superlattice as a function of sample temperature.

These results also correspond to a thorough analysis of activation energy published by Bimberg *et al.*¹⁰³ In this paper, quantitative results were obtained for radiative transitions which could be caused from pair dissociation interactions involving (1) a free exciton, (2) one free exciton and one free hole, (3) one free hole, and (4) two free holes and one free electron. Bimberg concluded that increasing the sample temperature reduces PL intensity by liberating holes from the bound-exciton complex. At higher temperatures, however, the intensity decreases even more rapidly as the activation energy process dominates, with the dissociation of free electron-hole pairs. Effects from electron-hole pair-pair correlations (or multi-exciton interaction) were considered negligible.

PL spectra shown in Figures 38 and 39, for (110) and (111) materials respectively, are very similar to the (100) case with only a few minor differences. In these figures, the impurity-associated localized carrier (IALC) peak at 1.086-1.087 eV is significantly more pronounced than for the (100) sample. In addition, the superlattice-related NP/pr peaks on (111) remain fixed as in the (100) case; however, these same peaks on the (110) shift together to 2-4 meV lower in energy. The NP/pr peaks seen in both (110) and (111) gradually reduce to the signal-to-noise threshold of the system at 12 K leaving only the boron-related Fe-Bh(TA) transition at 1.099 eV.

Structural Uniformity

To determine the structural uniformity of the superlattice across the wafer, a single 4×40 mm specimen was scribed from center to edge, and mounted as a single, unstressed sample in the Janis dewar. The laser was targeted on one edge of the specimen and a PL run was performed with the sample temperature at 3 K. Keeping the laser power, sample temperature, and all other conditions of the experiment constant, the sample was carefully translated under the fixed laser spot in 4 mm steps across the entire radial distance of the wafer. PL spectra was taken at each step.

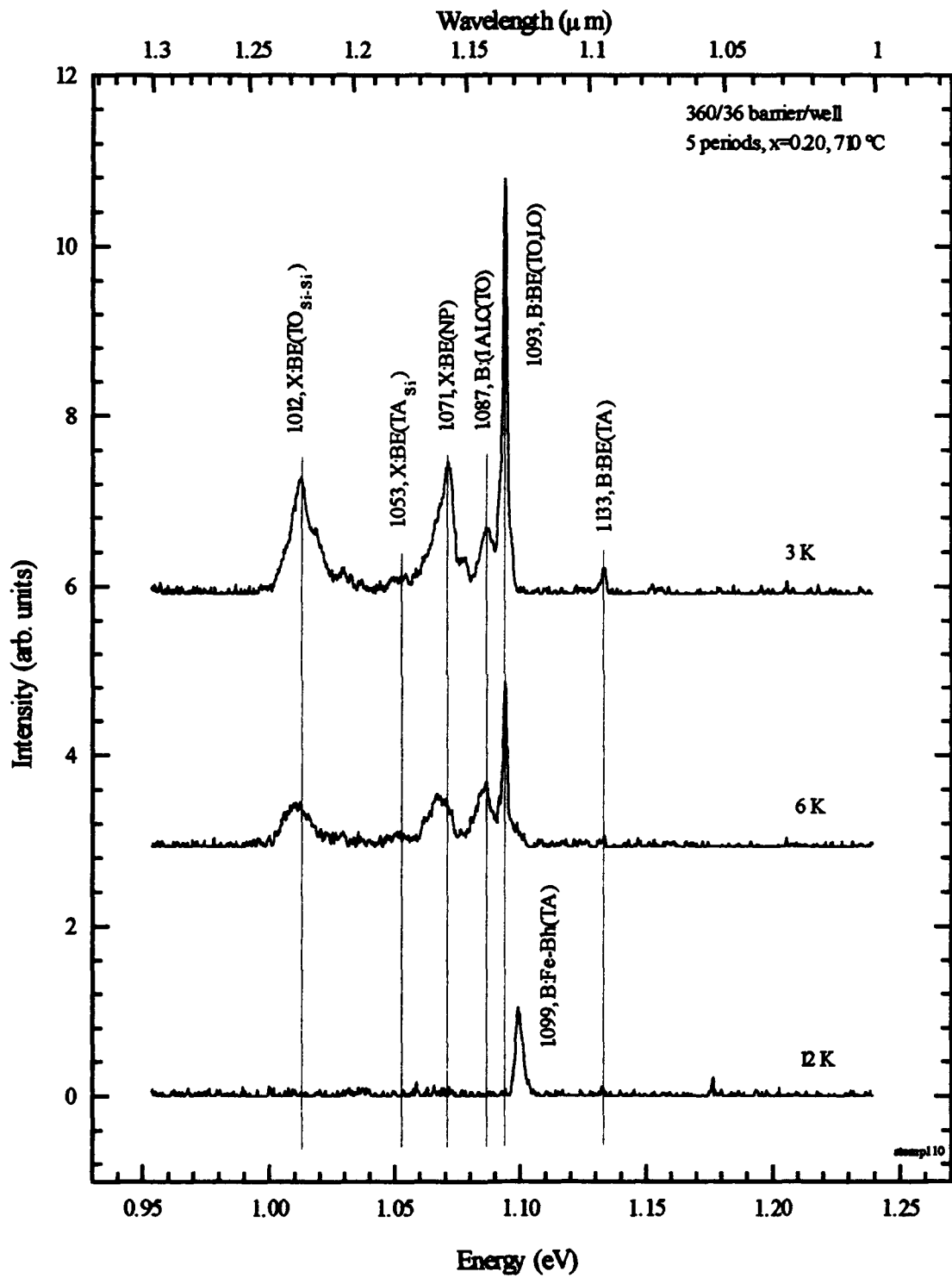


Figure 38. PL spectra of a (110) SiGe superlattice as a function of sample temperature.

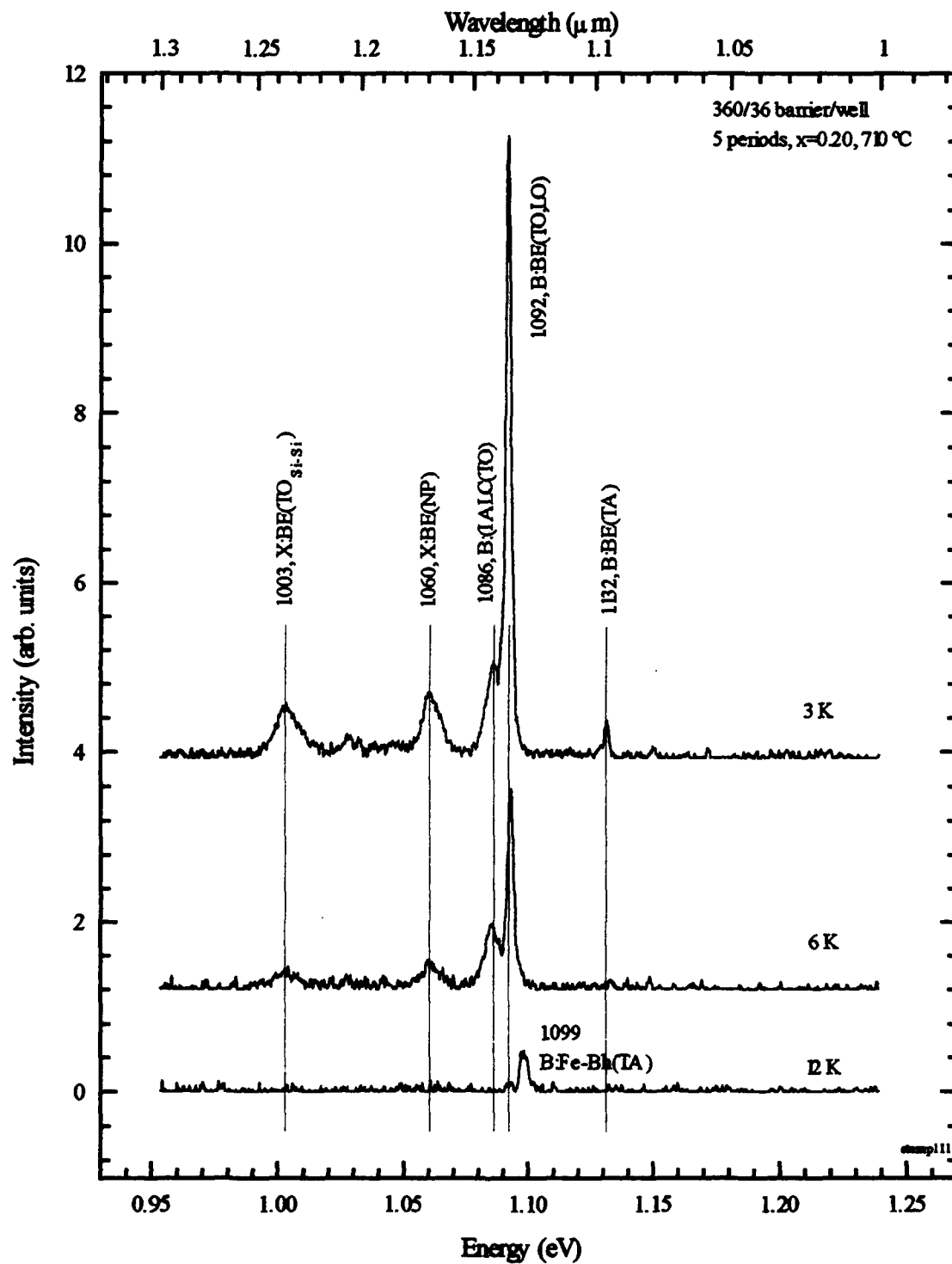


Figure 39. PL spectra of a (111) SiGe superlattice as a function of sample temperature.

Superlattices grown on (100), (110), and (111) Si substrates exhibited excellent structural uniformity as seen in PL spectra provided in Figures 40, 41, and 42, respectively. Peak intensities for all NP/pr peaks remained consistent relative to each other throughout the entire radial span of the wafer. In addition, peak intensities changed only 20% from wafer center out to 24 mm. PL intensity decreased another 20% beyond 24 mm out to wafer edge at 36 mm. Although great care was taken to ensure consistency between runs, it is possible that the sample may have rotated in azimuth very slightly while the sample was moved between steps. This would alter the optical alignment through the narrow slits of the spectrometer and could explain a decrease in the overall signal on the (100) and (110) Si samples. PL spectra from the (111) sample was especially uniform.

Checking wafer uniformity in this manner is important for two good reasons: First, PL is a very sensitive emission technique and when performed across a sample wafer as a function of radial position, it may reveal valuable information about surface deposition and growth kinetics as a function of source material temperature. Second, if focal plane array detectors are to be made from SiGe SLs, then uniform growth across a wide wafer area will be a critical growth condition. The MBE growth technique appears to deposit an extremely uniform center region, 1 in² on a 3-inch diameter wafer. As a comparison, commercial-grade laboratory detectors and CCD camera arrays have typical detector surface areas of 0.25 in².

Effects from Doping on Photoluminescence

One goal in this study was to attempt to tie together PL emission data depicting interband transitions and FTIR absorption data associated with intraband transitions in the VB well. One important step in making a successful detector, though, was to dope the quantum well with an acceptor element like boron. Unfortunately, doping boron in the

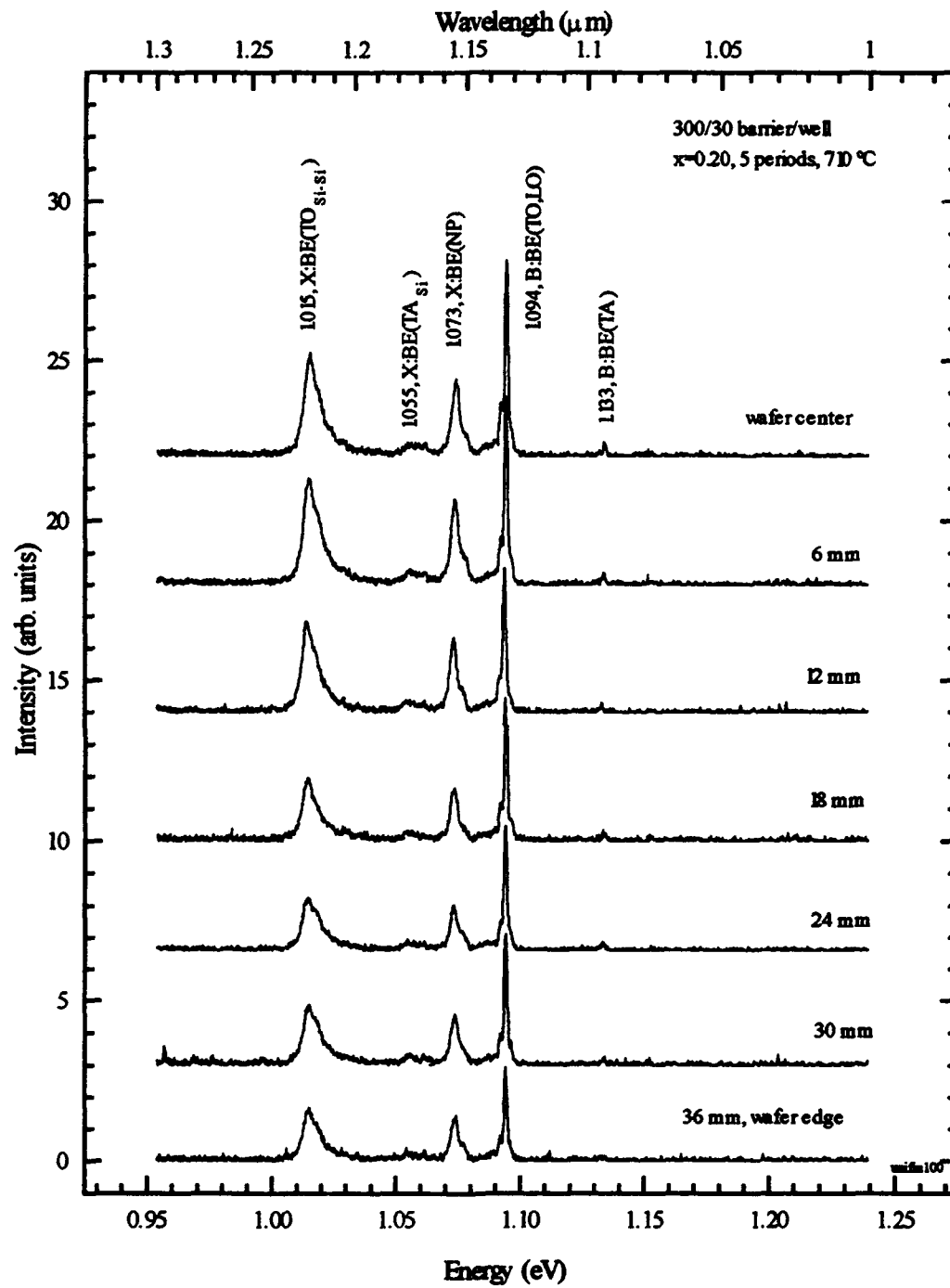


Figure 40. PL spectra of (100) SiGe superlattice showing wafer uniformity as a function of radial distance from center.

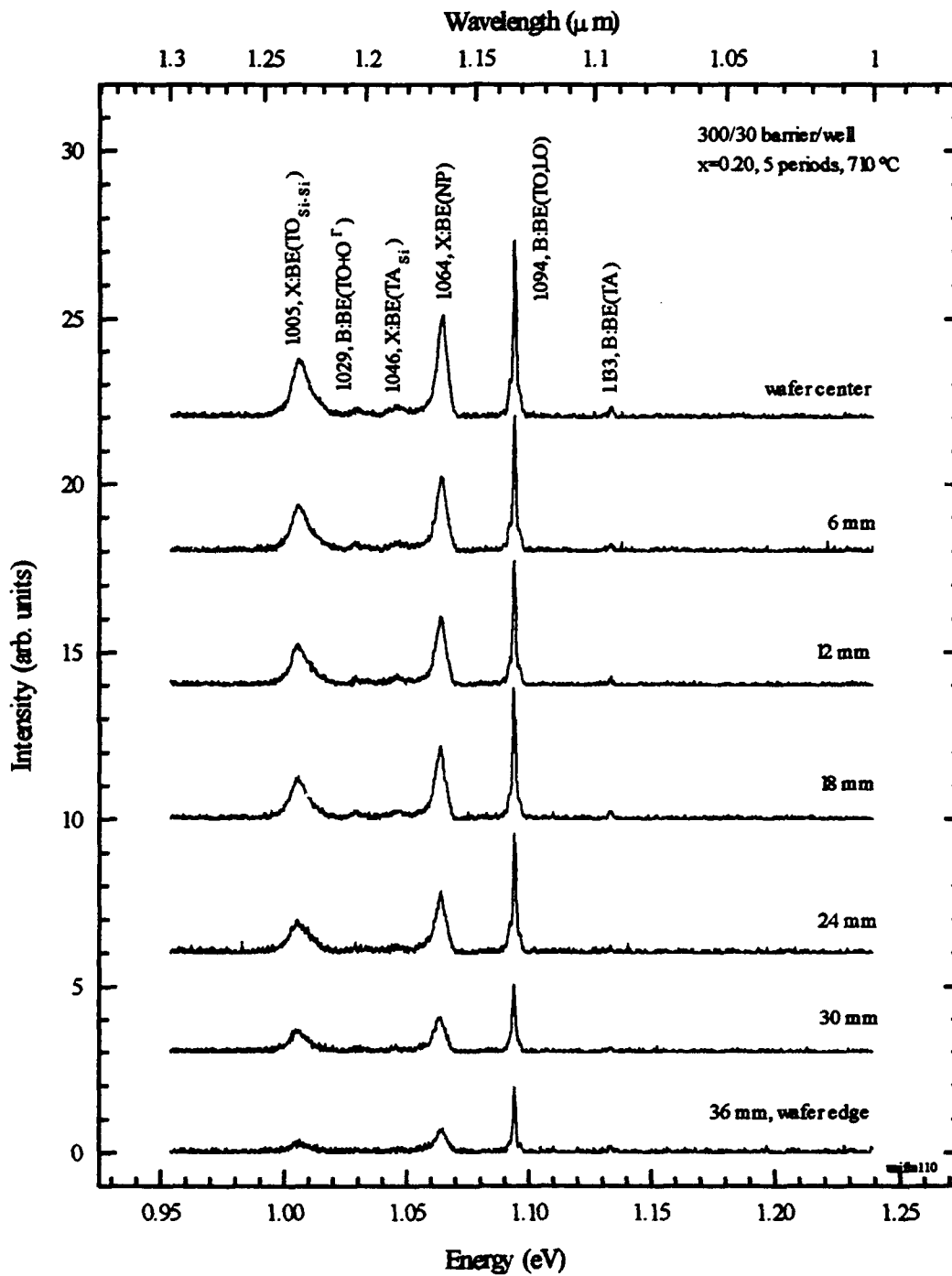


Figure 41. PL spectra of (110) SiGe superlattice showing wafer uniformity as a function of radial distance from center.

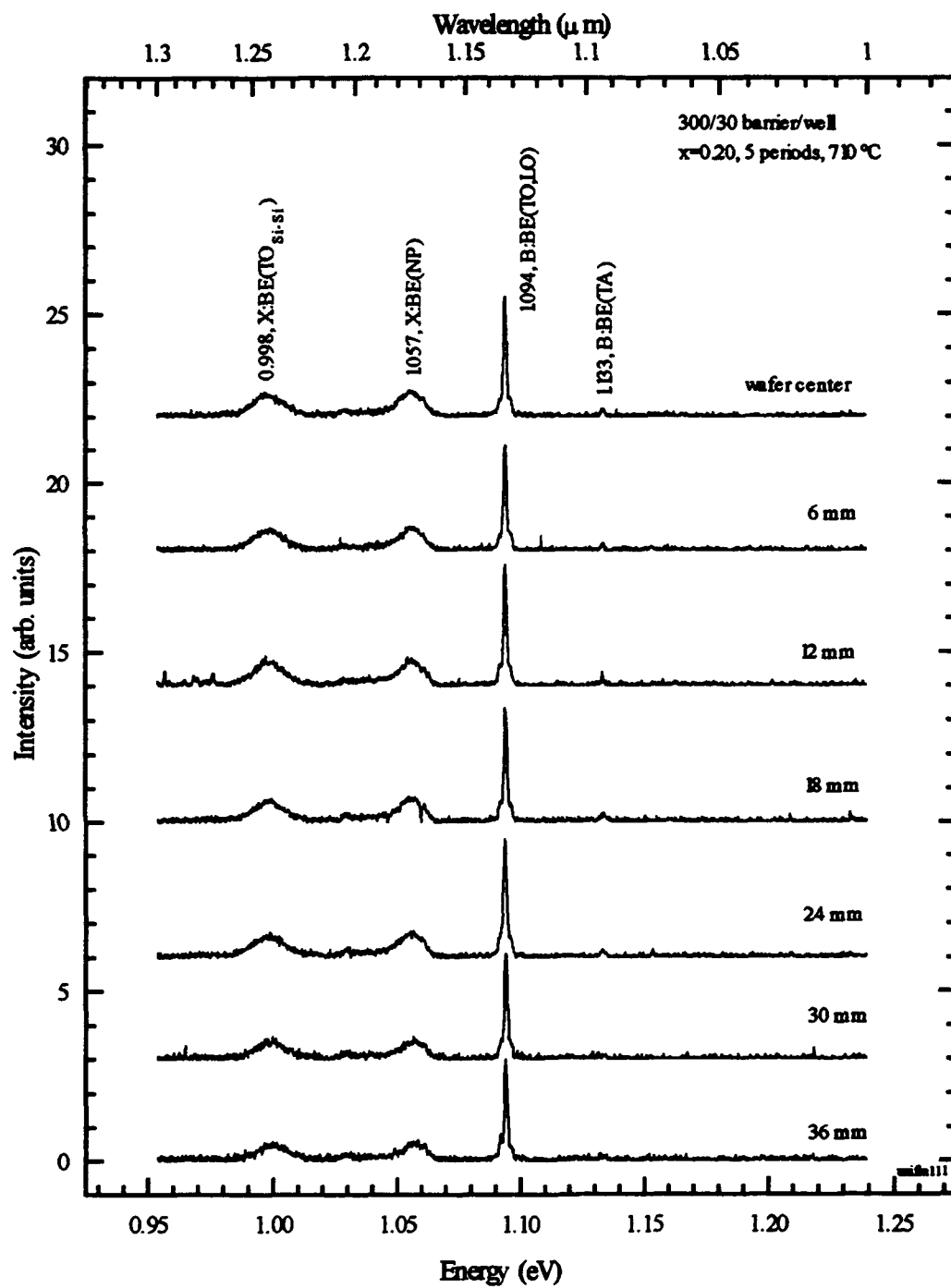


Figure 42. PL spectra of (111) SiGe superlattice showing wafer uniformity as a function of radial distance from center.

SiGe alloy epilayer greatly reduced PL emission which made it very difficult to correlate interband emission and intraband absorption data. In this study, boron dopant concentrations ranging from $1 \times 10^{19} \text{ cm}^{-3}$ to $1 \times 10^{20} \text{ cm}^{-3}$ were used.

In Figure 43, three doped (100) SiGe superlattice structures are directly compared to an undoped sample. In the undoped sample, the NP/pr peaks are clearly resolved with FWHMs measuring 5-8 meV. As dopant concentration increased, the FWHM broadened significantly, and the peak intensity of the NP/pr peaks decreased into noise. At the same time, the boron-related BE(TO,LO) and BE(TA) peaks increase in intensity by a factor of two, while their FWHM decreased from 6 to 2 meV. As doping increases, NP/pr emission from the superlattice structure broadens and diminishes as electron-hole pairs recombine in the degenerately doped SiGe epilayers. The almost total absence of NP/pr peaks in the highly doped structures may be attributed to screening of the electron-hole interaction by increased concentrations of free carriers. In addition, superlattice- and boron-related transitions may compete with each other for exciton capture and lead to non-radiative decay processes as was observed by Lightowlers in an 1990 survey of MBE Si.¹⁰⁴ Finally, the intensity of the boron-related peaks was shown to increase in intensity as the dopant concentration increases due to bound exciton transitions occurring with increased self-annihilation of excitons at the boron sites.

Three samples doped to $1 \times 10^{19} \text{ cm}^{-3}$ with boron are shown in Figure 44 with the Ge compositions of $x=0.20$, 0.30 , and 0.40 . In each case, an intense B:BE(TO,LO) line with a narrow FWHM is shown with broad NP/pr lines at lower energies. The NP/pr lines shift to lower energies, as they should for an interband transition, when the Ge composition is increased causing the valence band well to deepen.

Figures 45 and Figure 46 show PL spectra for similar $\text{Si}_{0.8}\text{Ge}_{0.2}/\text{Si}$ superlattice structures grown on (110) and (111) Si substrates, respectively, as a function of dopant

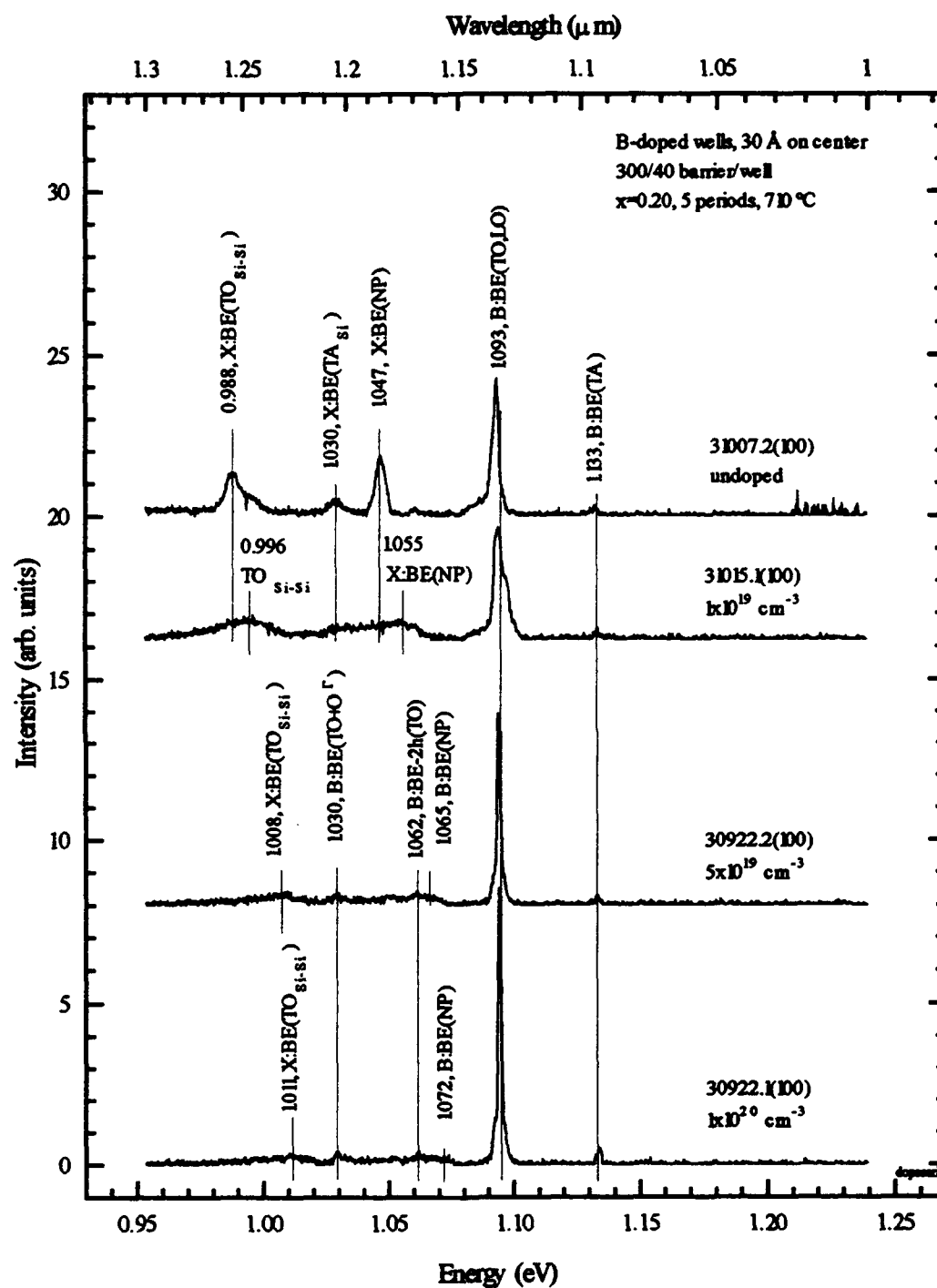


Figure 43. PL spectra of (100) SiGe superlattices with valence band wells which have been center-doped with boron.

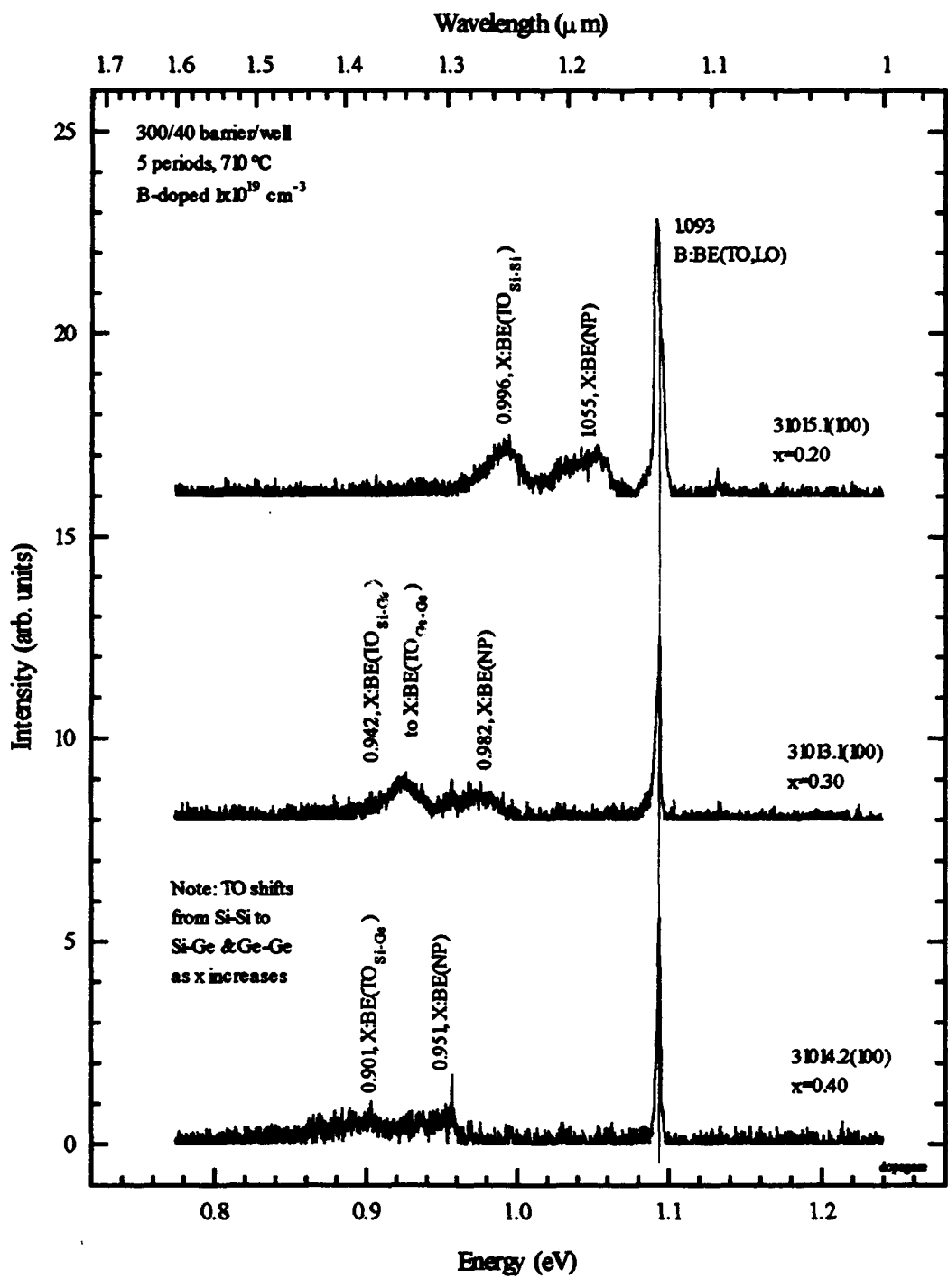


Figure 44. PL spectra of (100) SiGe superlattices with boron doped VB wells as a function of Ge composition.

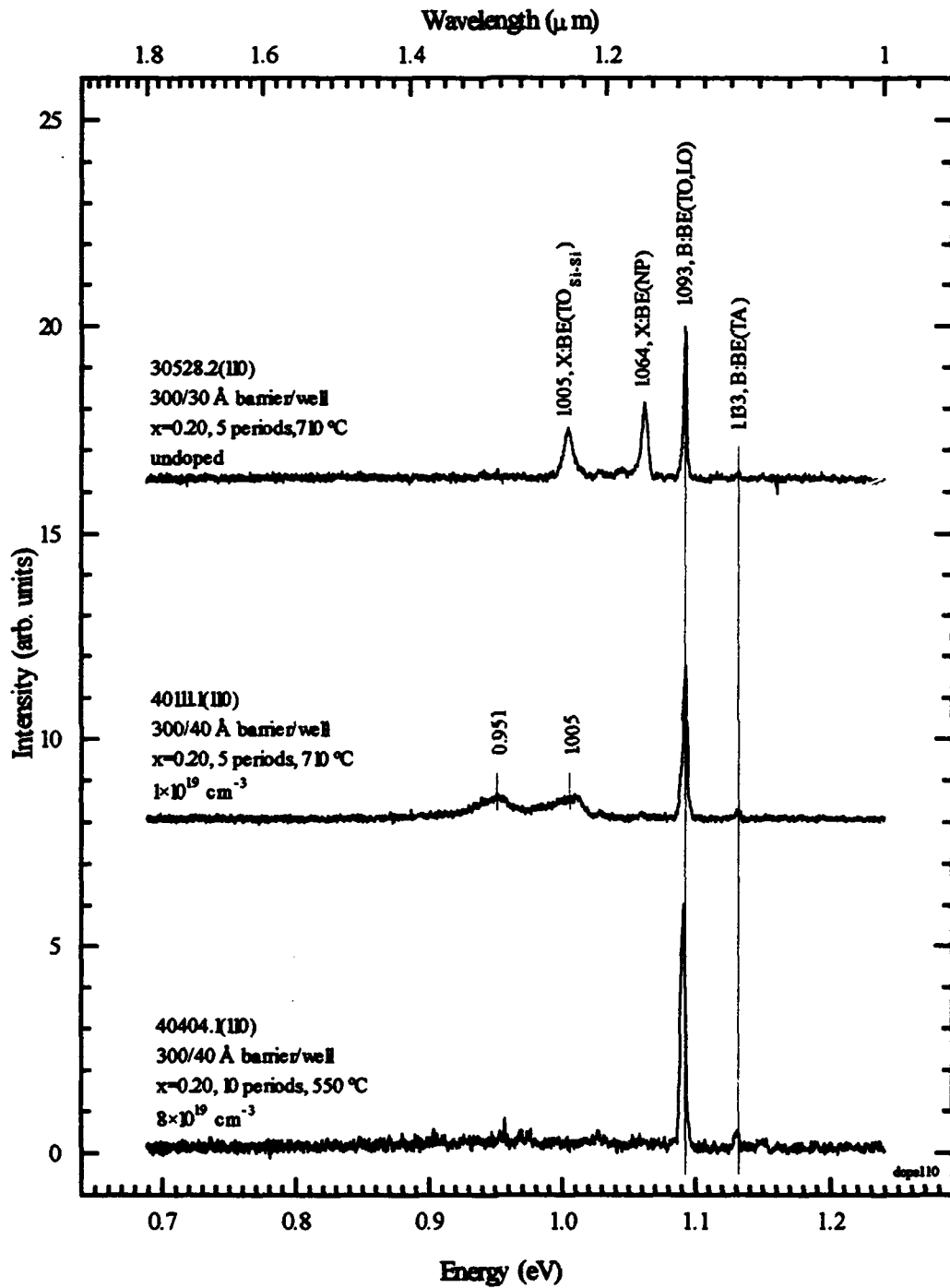


Figure 45. PL spectra of (110) SiGe superlattices with valence band wells which have been center-doped with boron.

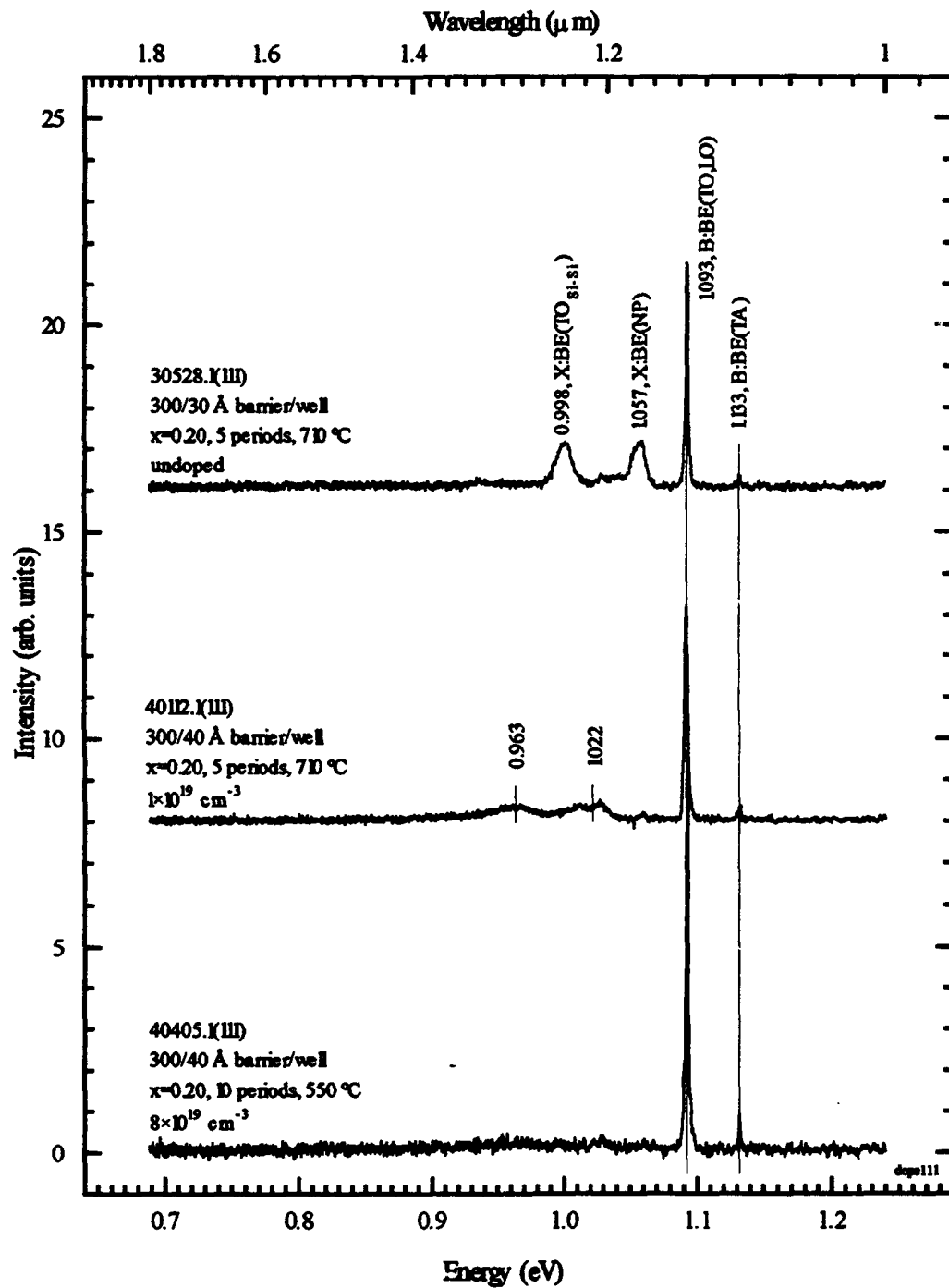


Figure 46. PL spectra of (111) SiGe superlattices with valence band wells which have been center-doped with boron.

concentration. This is the first reported case of a SiGe superlattice being grown on a (110) structure, and the first case of such heavily doped SiGe superlattices being grown on non-conventional Si substrates. As in the (100) case, the NP/pr peaks on (110) and (111) materials broaden and decrease in signal intensity. Note, the NP/pr shift to lower energy from the undoped superlattice to the sample doped 1×10^{19} B/cm³ is primarily due the increased well width from 30 to 40 Å. As in the (100) case, the boron-related peaks at 1.093 and 1.133 eV significantly increase and sharpen for both (110) and (111) structures.

PL Data Supporting FTS Absorption

One initial concern (of many) before attempting to measure the photo-absorption from a sample which had been fashioned into a waveguide was whether cutting the edge facets and polishing the backside of the sample would somehow damage the superlattice. To answer this concern, a waveguide was fabricated from a typical superlattice sample that had exhibited a highly-resolved PL spectrum. The results are shown in Figure 47.

Peak intensity of the all peaks decreased in the PL run taken after the sample was fabricated into a waveguide. These changes in absolute peak intensity may be explained by the fact that these runs were taken 10 days apart. No attempt was made to reproduce the exact same signal intensity for a given peak on the second run. The relative intensity between peaks, however, should remain very similar.

The superlattice-related NP/pr peaks changed very little relative to each other; however, the boron-related BE(TO,LO) decreased sharply, to almost the same relative intensity as the TO_{Si-Si} peak. The B:BE(TA) was completely absent after the waveguide was made. Only the top surface of the sample was illuminated with the excitation source in both runs, and the Ar⁺ beam can only penetrate to the buffer layer of the structure. Only the bottom surface and the edges of the sample were ground and polished to make the

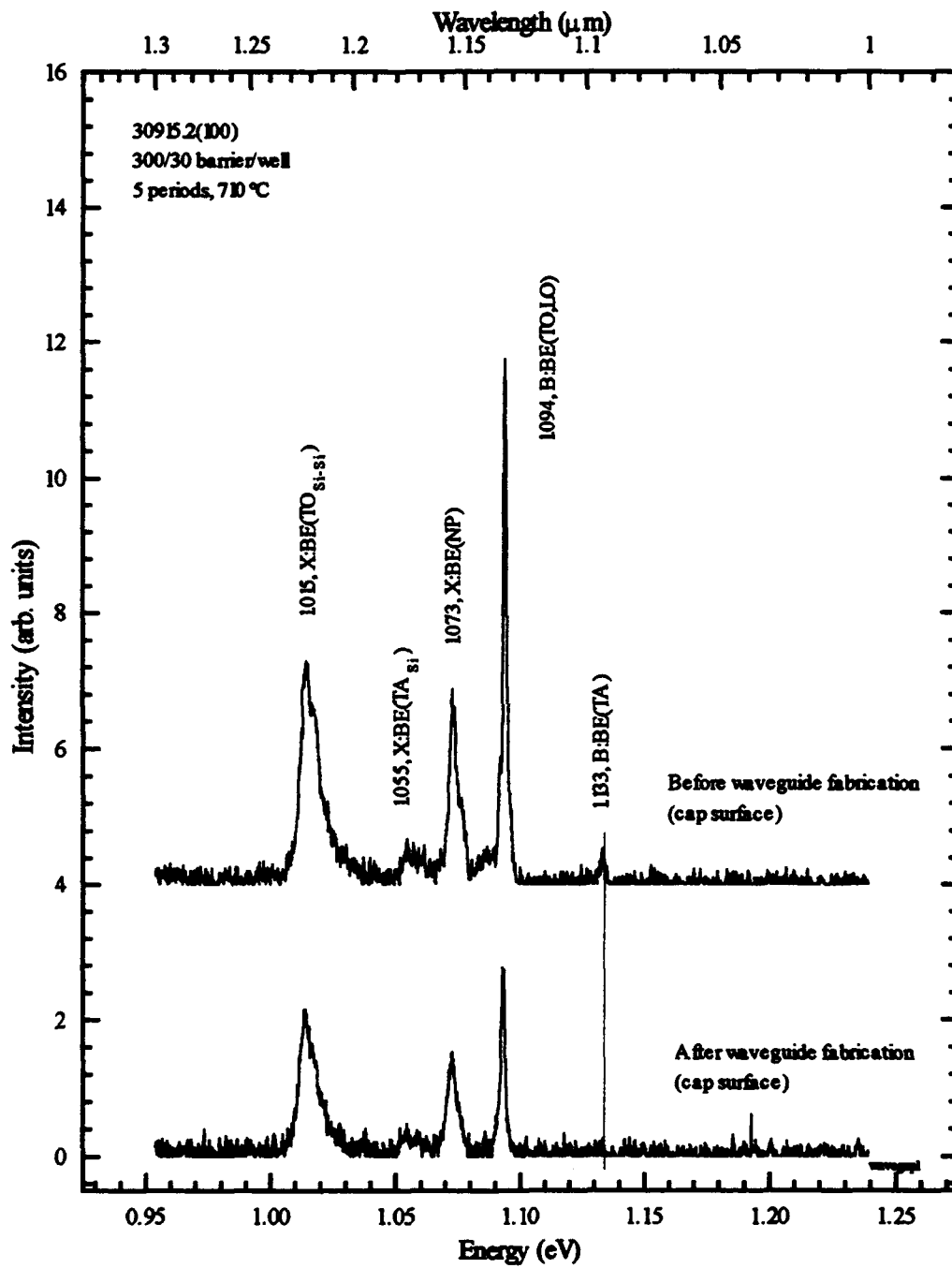


Figure 47. PL spectra of a (100) SiGe superlattice before and after waveguide fabrication.

waveguide. Although the PL system optics are usually tuned to detect emission from the sample edge for maximum signal, there is no evidence which explains why only the boron-related peaks would be affected after waveguide fabrication. In any case, this did not affect subsequent absorption measurements on other samples.

Fourier Transform Spectroscopy: Identification of Absorption Peaks Associated with the Si Substrate

A Si substrate with no superlattice structure was measured using the single-pass, normal view (SPNV) background subtraction technique. In Figure 48, the FTIR absorption spectrum of a p-type (100) silicon substrate is shown with the predominant peaks identified by Pradhan.¹⁰⁵ This spectrum was taken with 8 cm⁻¹ resolution, a typical resolution used throughout this study. Higher resolution runs reveal finer structure throughout the spectrum. In fact, further literature searches uncovered a tremendous number of peaks in the Si substrate alone, all a result of multiphonon transitions. A comparison of theoretical predictions,^{106,107,108} reported experimental values,¹⁰⁵ and peaks observed in this study are shown in Table XI beginning on the next page. The measurements in this table were taken at 5 K, from approximately 2 to 14 μm.

The sample used for measurements conducted at AFIT was a Czochralski (CZ), p-type (100) Si substrate. The SPNV background subtraction technique was used with no condensing optics and polarizer. The scan range was set from 4000 to 400 cm⁻¹ (i.e. 2.5 to 25 μm), for 512 co-added scans. No significant structure was observed from 4000-2000 cm⁻¹ although several weak Si-H complexes are predicted in that range based on theoretical calculations. The peak positions of some multiphonon bands differed by only a few wavenumbers; however, this can easily be due to small changes in ambient

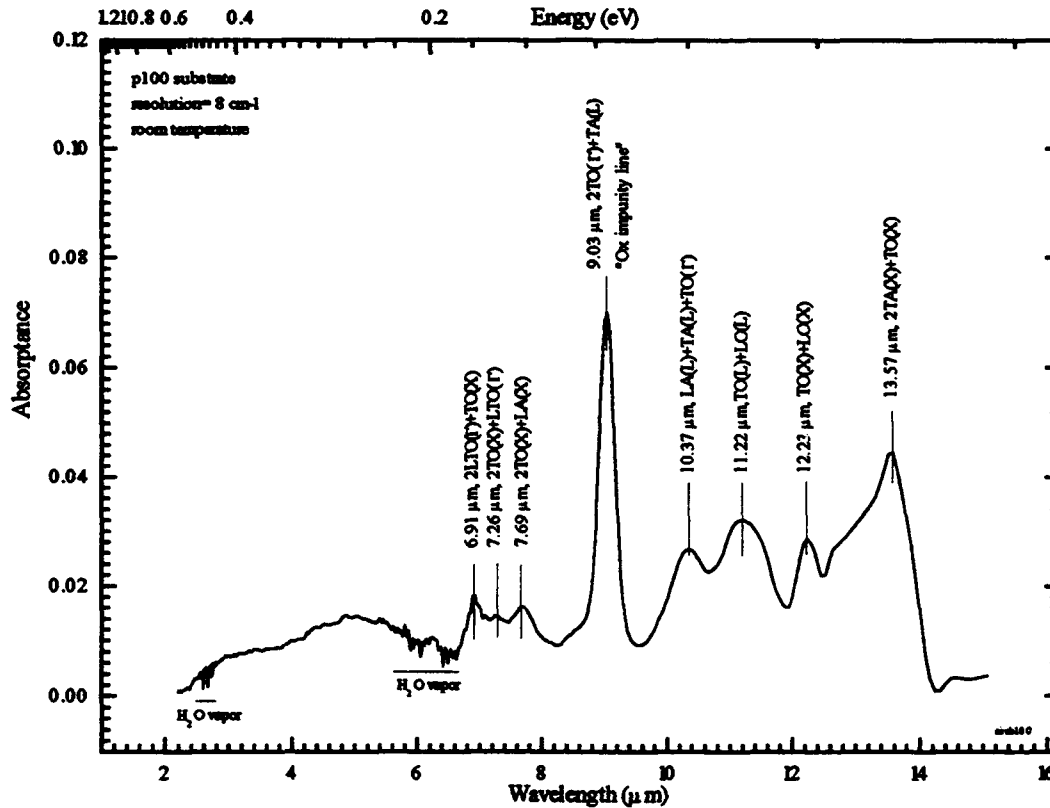


Figure 48. Absorption spectrum of a Czochralski p-type (100) silicon substrate.

Table XI. Multi-phonon transition peaks for bulk Si substrate.

Theoretical Values (cm ⁻¹)	assignment	comments	reported experimental values (cm ⁻¹)	experimental results at AFIT: p-type (100)Si
		strong Si-H complex	2210	not observed
		Si-H complex, (Ox related)	2191	not observed
		Si-H complex, (Ox related)	2123	not observed
		Si-H complex	2178	not observed
		Si-H complex	2048	not observed
		Si-H complex	1994	not observed
		Si-H complex	1950	not observed
		strong Si-H complex	1946	not observed

Theoretical Values (cm ⁻¹)	assignment	comments	reported experimental values (cm ⁻¹)	experimental results at AFIT: p-type (100)Si
1726	LTO(Γ) + LO(L) + TO(X) + LA(L)		1724	1717.4
1443	2 LTO(Γ) + TO(X)		1444	1440.3
1397	2 TO(X) + LTO(Γ)		1385	1376.9
1300	2 TO(X) + LA(X)		1300	1301.1
		O _i	1226	1224.2
		Si-O stretching	1207	not observed
1104	2 TO(Γ) + TA(L)	Si-O sym stretch Si ₂ O asym stretch strong O impurity line	1107	1107.1
		C-O complex	1093.6	not observed
		C-O complex	1047.5	not observed
		O _i	1059	not observed
		O _i	1013	not observed
968	LA(L) + TA(L) + TO(Γ)		968	961.7
		N impurity	963	not observed
888	TO(Γ) + LO(L)		887	868.1
849.6	TO(X) + LO(X)		839	817.0
		Si-H bending	812	not observed
		Si-H wagging	791	not observed
		N impurity	766	not observed
787	TA(X) + TO(Γ)		790	786.7
741.6	2 TA(X) + TO(X)		739	741.0
676.6	LO(L) + TA(L) + TA(X)	C-O complex	680	687.6
		N impurity	653	not observed
		C-O complex	636.7	not observed
614	TO(L) + TA(X)	strong "two-phonon" band, strong C impurity line inc., C-Si and C-O complexes	609.5	621.4
		C-O complex	586.2	not observed
562	2 TA(X) + TO(X)	O _i	567	566.4
		Si ₂ O bending Si ₂ O sym stretch, O _i	513	514.1

temperature of the FTIR system (not the sample temperature). At lower sample temperatures, certain lines would shift to slightly higher frequencies (wavenumbers) corresponding to slightly higher peak transition energies.

Once these peaks were identified, the true challenge, ironically, was to eliminate the Si-related peaks entirely from the spectrum leaving only peaks associated with intersubband transitions. In practice, it was *very* difficult to perform a clean subtraction between a superlattice and substrate-only sample. Consider that for a typical superlattice sample, only 150-200 Å of SiGe alloy is the "active" absorption region grown on 0.3 mm of Si substrate. Assuming an atomic spacing of 2 Å, then a clean FTIR absorption measurement becomes an attempt to discriminate the photo-absorption properties of approximately 80 atoms against a background of 1,500,000 atoms! By now it should be obvious why the Si substrate contributes such an overwhelmingly strong signal. The resulting division of both single-beam spectra is very sensitive to small changes and strongly affected by small differences in sample thickness. It took nearly seven months to design and build the correct sample mounts, develop the background subtraction techniques, and implement laboratory procedures to completely subtract out the spectrum associated with the Si substrate.

Validation of Background Subtraction Techniques

To validate background subtraction techniques, an *n*-type InGaAs/AlGaAs superlattice was acquired from Wright Laboratories. The excellent results obtained from this sample using the SelfRef technique are shown in Figure 49 and directly compared with results using the Fresnel angle technique. The SelfRef background subtraction technique improved signal intensity by a factor of 12 over the Fresnel Angle technique and resolved a second peak within the structure. This peak had been predicted theoretically but not seen until now. Because the signal was so strong, the SelfRef technique provided a

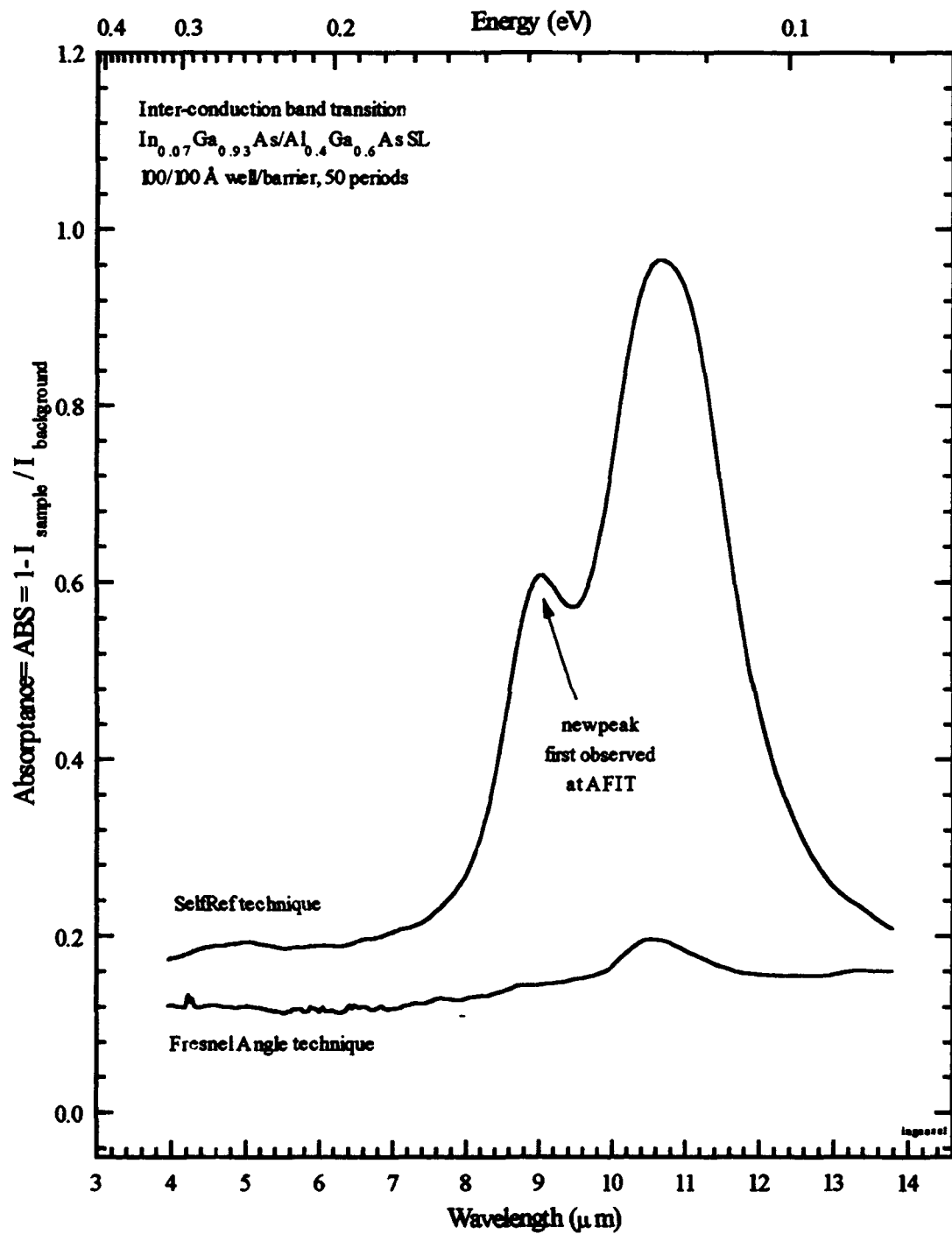


Figure 49. FTIR absorption spectra of an InGaAs/AlGaAs superlattice using the SelfRef and Fresnel Angle background subtraction techniques.

near-perfect background subtraction which effectively leveled the spectrum. No free-carrier effects, which typically cause the spectrum to assume an overall, negative linear slope were seen with this sample under these conditions. In addition, nine more samples were fabricated into waveguides and examined to track the intersubband absorption peak shift as a function of well width. All the *n*-type samples exhibited excellent background subtraction and leveling revealing clearly resolved, multiple peaks which shifted to longer wavelengths as well width increased from 100 to 200 Å with fixed 100 Å barriers. Five $\text{In}_{0.07}\text{Ga}_{0.93}\text{As}/\text{Al}_{0.4}\text{Ga}_{0.6}\text{As}$ provided by Wright Laboratories are shown in Figure 50. Note, as well width increases beyond 150 Å, the second peak disappears indicating that the energy difference between two higher transition energy levels above the ground state in the CB has decreased so that the difference between both excited levels above the ground state is nearly indistinguishable at room temperature. All InGaAs/AlGaAs spectra were taken with 256 scans.

After validating each absorption technique with the $\text{In}_{0.07}\text{Ga}_{0.93}\text{As}/\text{Al}_{0.4}\text{Ga}_{0.6}$ samples, several boron-doped, *p*-type, superlattices with 40 Å $\text{Si}_{0.80}\text{Ge}_{0.20}$ VB wells and 300 Å barriers were grown on (100) Si wafers. Eight attempts at growing such a structure at 710 °C produced excellent PL but failed to produce discernible absorption at or near 8 μm as expected. To further validate our own subtraction techniques and equipment, similar samples grown at UCLA were obtained.

The absorption spectrum from one of the UCLA samples is shown in Figure 51. Here, the SLRef background subtraction technique was used—the same technique used by Wang, Karunasiri, and Park at UCLA. In this case, single-beam spectra of the superlattice sample JP155 were taken at five polarization settings ranging from 0° to 90° in 22.5° increments. Next, a doped superlattice with a similar structure as JP155 was examined as a function of polarization, in exactly the same fashion. The spectrum from the undoped sample served as the background. The results shown in Figure 51 indicate

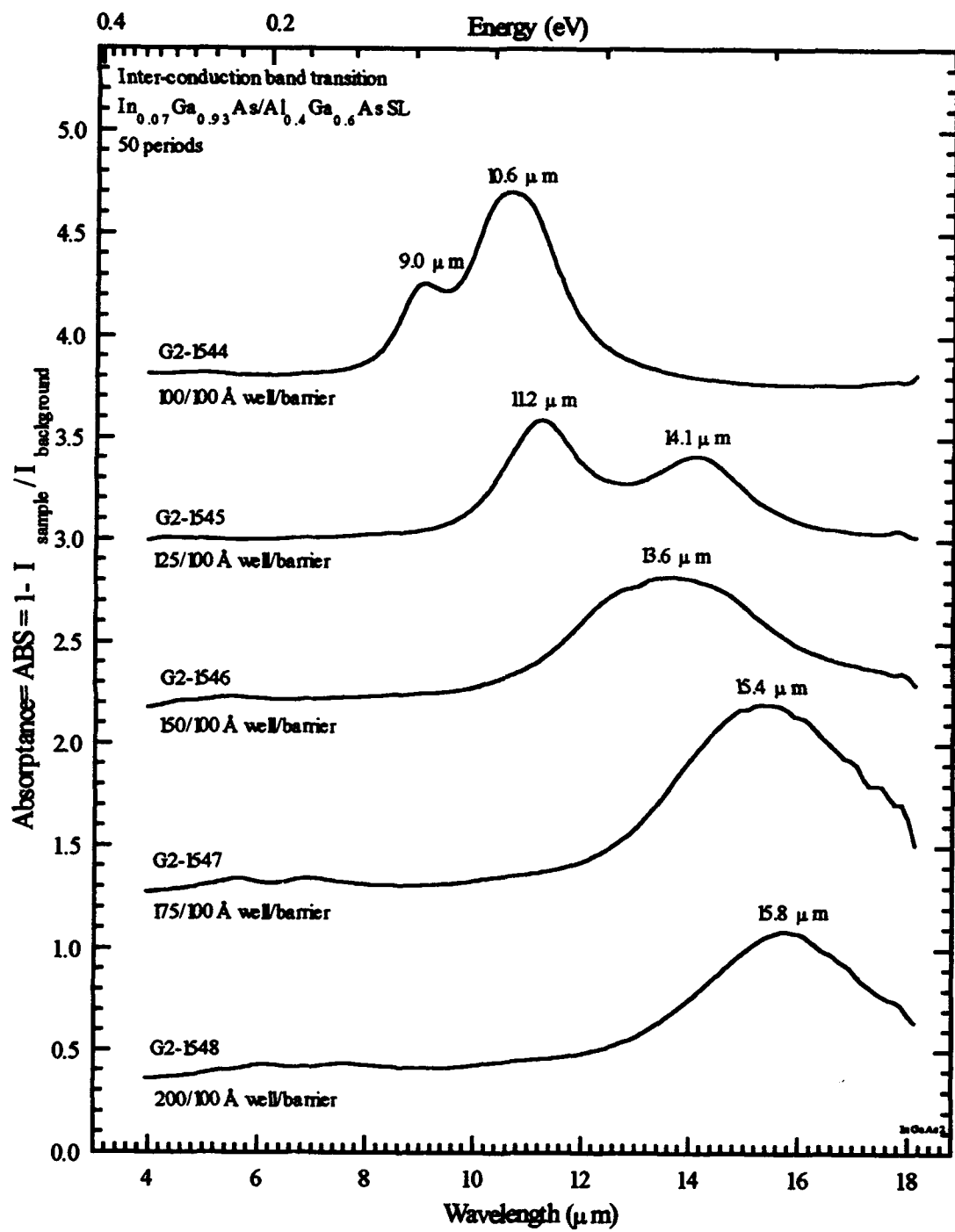


Figure 50. FTIR absorption of five InGaAs/AlGaAs superlattices with different well widths.

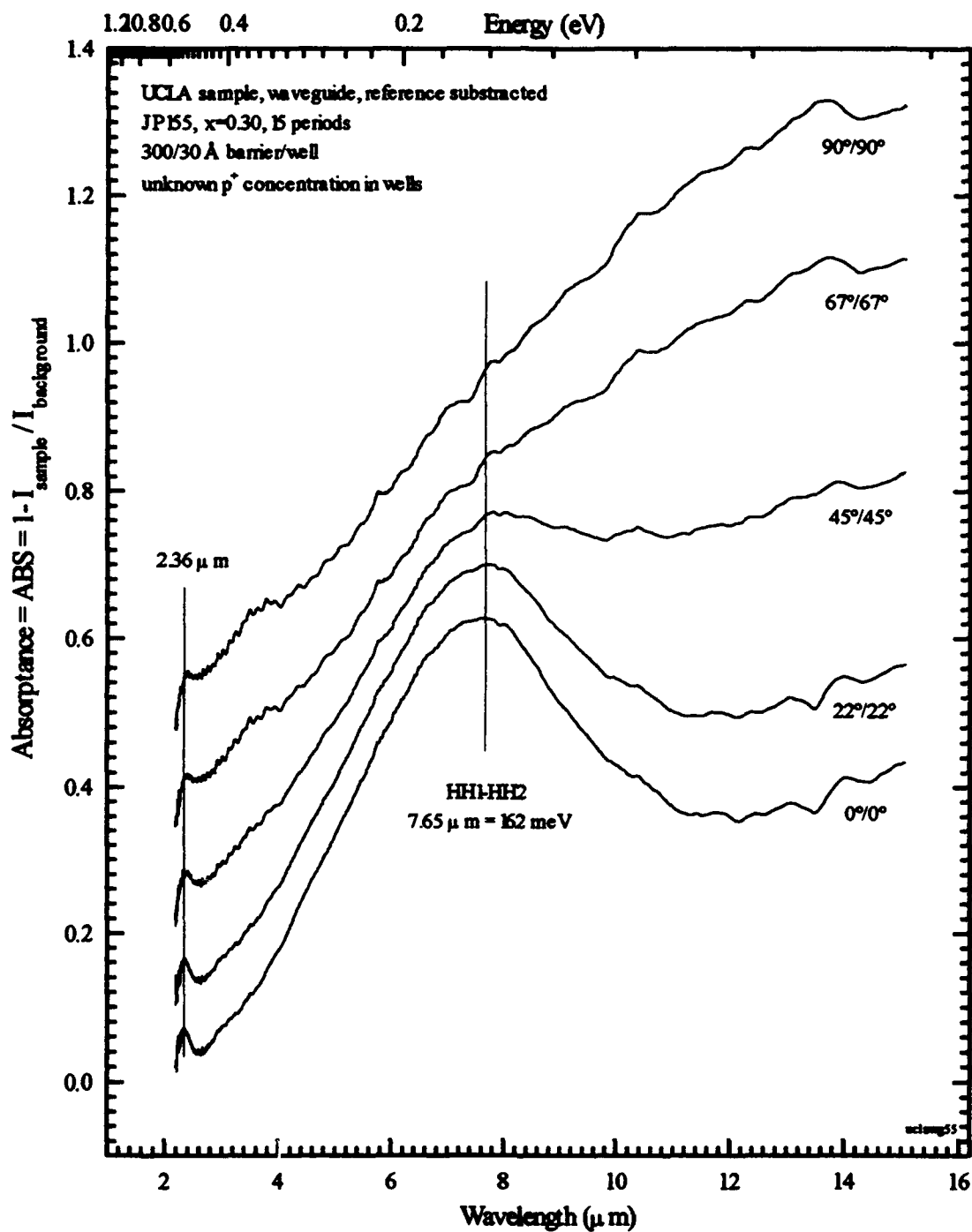


Figure 51. FTIR absorption spectra of a p -type SiGe superlattice as a function of polarization (SLRef).

that the intersubband, HH1→HH2 absorption peak is clearly observed when the polarized electric field vector is rotated 90° out from the quantum plane—just as the valence band selection rules predicts it should. As the polarizer rotates \vec{E} so that it lies on the plane, free-carrier absorption is the predominant transition, increasing linearly as a function of increasing wavelength—or ever-decreasing transition energy within the same subband.

The source of the small peak at 2.35 μm cannot be positively identified; however, it cannot be quantum-well related. Although peaks from 2-5 μm have been identified by Karunasiri as either an HH1→continuum or intervalence-subband transitions at normal incidence, this specific peak did not change during this study as a function of Ge composition, boron dopant concentration, silicon substrate, sample growth temperature, different optical layouts in the FTIR system sample chamber, or background subtraction technique. In fact, the same peak appeared consistently even on totally different *p*-type material systems, such as GaAs/AlGaAs superlattices. This peak is seen while using the DTGS detector in the sample waveguide configuration. To eliminate the possibility that the detector had an abrupt system response at that specific wavelength, the single-beam spectra were examined datum point-by-datum point; however, nothing unusual was uncovered. Since the detector response was consistent, this effect should have been background subtracted out in any case. It is possible that this peak may be associated with a common impurity found in SiGe and AlGaAs material systems; however, this same peak appears to shift slightly to 2.54 μm on boron-doped (110) SiGe samples. No impurities or contaminants have been identified with absorption peaks from 3900–4250 cm^{-1} . It was also considered that this peak could be attributed to another etalon-like absorption effect. For an index of refraction ranging from 3.4 to 4.0, this would require an etalon only 2900–3400 Å thick to be formed. Although this is the approximate thickness of the cap and a 5 period structure, the same peak was seen at the same energy on structures with 5, 10, 15, even 50 periods.

Absorption Results from NRL Samples

The absorption spectrum for a *p*-type SiGe MQW grown by NRL at 550 °C which exhibited strong intersubband absorption is shown in Figure 52. Since, an undoped superlattice was not available as a background reference, a *p*-type (100) substrate was used instead for the SubRef background subtraction. Peaks at 8.15 μm, 9.03 μm, and longer wavelengths have been identified as Si substrate related. Specifically, the sharp peak at 8.15 μm is attributed to a small difference in the amount of interstitial oxygen (O_i) found in the substrate as in the doped superlattice. Similarly, the 9.03 μm peak is attributed to Si-O complex symmetric stretching and Si-O₂ complex asymmetric stretching. The 9.03 μm (1107 cm⁻¹) peak was always the strongest silicon-related feature of the spectra and a great deal of time was spent finding ways to eliminate this feature.

Since all of the waveguide FTIR measurements on the SiGe materials were extremely low-light level, the sample waveguide would normally be rotated in azimuth to effectively "tune" the centerburst amplitude of the setup scan for maximum signal. Since every subtraction technique is based on the *divisor* difference in spectra amplitude, rotating a sample in azimuth should not have had any effect in the peak spectra from sample to sample using the SubRef or SLRef techniques, and especially with a single sample using the SelfRef technique. Yet, the 9.03 μm peak remained. Several numerical techniques were explored to eliminate the peak, including normalizing the single-beam spectrum to (a) the peak detector response, and (b) the oxygen impurity line itself, but these methods skewed the spectrum in undesirable ways.

Maintaining the waveguide sample at 45° azimuth angle from run to run finally eliminated the final vestiges of the silicon-related spectrum in most spectra. In this configuration, the FTIR probe beam is at normal incidence to the waveguide facet. More importantly, by selecting a specific azimuthal incidence angle and keeping that fixed, all

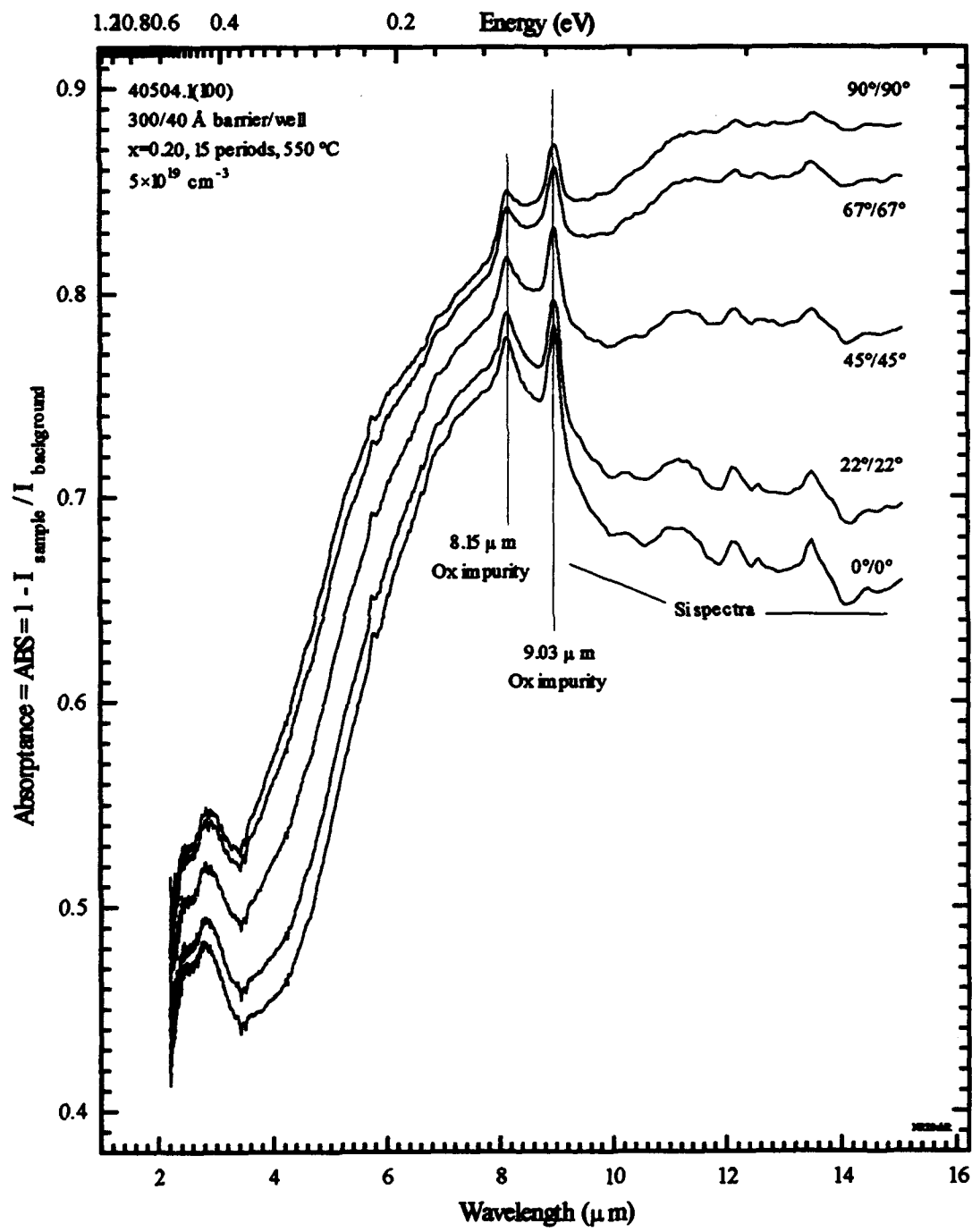


Figure 52. FTIR absorption of SiGe sample 40504.1(100) as a function of polarization (SubRef).

subsequent measurements could be compared effectively, even at low light levels. It is believed that by changing the incidence angle even slightly, to maximize signal throughput, the waveguide geometry causes the path length of the internally reflected light to change just enough so that more (or less) silicon is being sampled in a given single-beam spectrum. When this spectrum is compared to another spectrum, taken at another time from a different sample mounted with a slightly different azimuth angle, there is enough difference to cause a silicon-related peak to emerge.

The oxygen impurity absorption peak, and other silicon-related features, were much less pronounced using the SelfRef technique since the same sample, at the same azimuth, was used as a reference and not moved between runs at different polarizations. However, the 9.03 μm peak still remained evident until the waveguide was fixed at a 45° azimuth angle, so that the facet was at normal incidence to the FTIR beam. Although keeping the samples at 45° greatly reduced signal throughput—sometimes by more than 50% of an already weak signal—eliminating, or at least, greatly reducing the oxygen impurity peaks was one of the last hurdles in acquiring credible data.

As in the UCLA sample shown in Figure 51, the HH1→HH2 intersubband transition of the NRL sample shown in Figure 52 is also strongly dependent on the polarization of the incident beam. The intersubband absorption peak is clearly observed, and free-carrier absorption is minimized, when the polarized electric field vector is perpendicular to the quantum plane (polarizer set to 0°). At 90° free-carrier absorption is maximum now that the entire photon field lies in the quantum plane.

In Figure 53, the same sample is shown using the SelfRef background subtraction technique. Initially, the spectra obtained using the Sub/SLRef and SelfRef techniques looks very different; however, after proper interpretation and background leveling, these two very different background subtraction techniques actually provide very similar results.

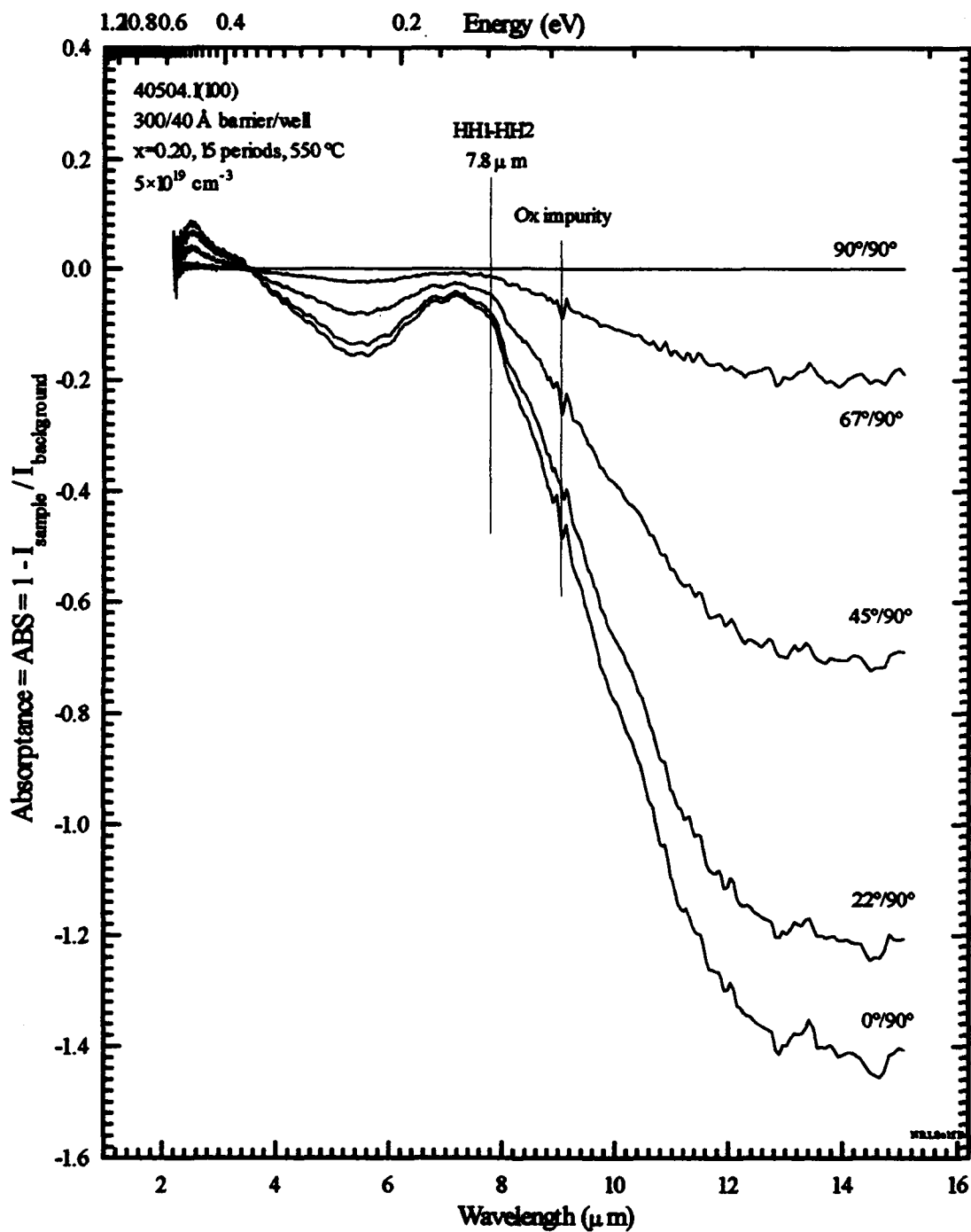


Figure 53. FTIR absorption of SiGe sample 40504.1(100) as a function of polarization (SelfRef).

The underlying principle supporting the SelfRef technique is that since Si is a cubic material, the spectrum taken at one polarization should be no different than the spectrum taken at another polarization. Therefore, the only spectral features that should remain using this subtraction technique should be those attributed to the superlattice alone, which should show distinct absorption preferences for one polarization over another.

Two effects occurring simultaneously account for the consistently decreasing slope of the spectra shown in Figure 53. Free carrier absorption is increasingly more predominant as wavelength increases (or as the transition energy decreases). Second, less absorption from free carriers occurs as the polarized electric field is rotated out of the quantum plane at 90° up to a position perpendicular to the quantum plane at 0°. Recalling the definition of absorptance,

$$ABS = 1 - \left(\frac{I_{sample}}{I_{background}} \right),$$

where I_{sample} represents the single-beam spectra at 67°, 45°, 22°, and 0°, and $I_{background}$ is the single-beam spectrum taken at 90°. As the polarizer setting advances from 67°/90° to 0°/90°, the quotient $I_{sample}/I_{background}$ becomes greater assuming the single-beam spectrum of I_{sample} has a greater magnitude point-for-point than the single-beam spectrum of $I_{background}$. At 90°, absorption from free-carriers is maximum since the entire electric field lies in the quantum plane, therefore $I_{background} < I_{sample}$. Therefore, ABS becomes increasingly negative resulting in a negative slope. As mentioned earlier, maintaining the sample at 45° in azimuth between runs, so that the incident beam is normal to the waveguide facet, effectively eliminates the oxygen impurity peak seen previously.

Although the SubRef and SLRef techniques are more straightforward conceptually, the SelfRef technique has two distinct advantages. First, the SelfRef technique does not require a separate background sample to be grown, fabricated into a waveguide, and mounted. Second, this technique appears to provide a slightly enhanced

signal intensity and resolution. This technique easily resolved the second peak in the *n*-type InGaAs/AlGaAs samples shown earlier which was not seen using the SLRef method.

In Figure 54 the SelfRef plot has been background *leveled* to resemble a more typical absorption spectrum. Leveling can be accomplished several ways using different data subtraction techniques and baseline equations. In this case, the data was baselined using a linear relation, or straight line, drawn from one datum point at 2 μm to another datum point at approximately 14 μm . The pristine data was then subtracted from this linear relation to level the overall spectrum along a zero reference. This type of background leveling can be accomplished almost effortlessly using powerful worksheet programs such as MicroCal Origin.

Comparing Figures 51 and 54, the HH1 \rightarrow HH2 transition identified on the UCLA sample occurs at 7.65 μm versus 7.8 μm reported on the NRL sample. This small energy shift of 3-4 meV is explained by noting the JP155 was grown with a germanium composition of $x=0.3$ while that for 40504.1(100) is $x=0.20$. As expected, the intersubband transition shifts to higher energy (shorter wavelength) as the well deepens with greater germanium composition. Since the transition occurs between two subbands in the VB well, this energy shift is not expected to be as sensitive to changes in Ge composition as an interband transition, where the NP emission peak may shift as much as 40-60 meV as shown directly in PL measurements and predicted in single quantum well and Kronig-Penney model calculations.

Results from the Single Quantum Well and Kronig-Penney Models

Single quantum well (SQW) and Kronig-Penney (K-P) models were developed to compute the bandgap and intersubband transition energies of $\text{Si}_{1-x}\text{Ge}_x$ structures grown on (100), (110), and (111) Si substrates. Interband bandgap measurements of multiple

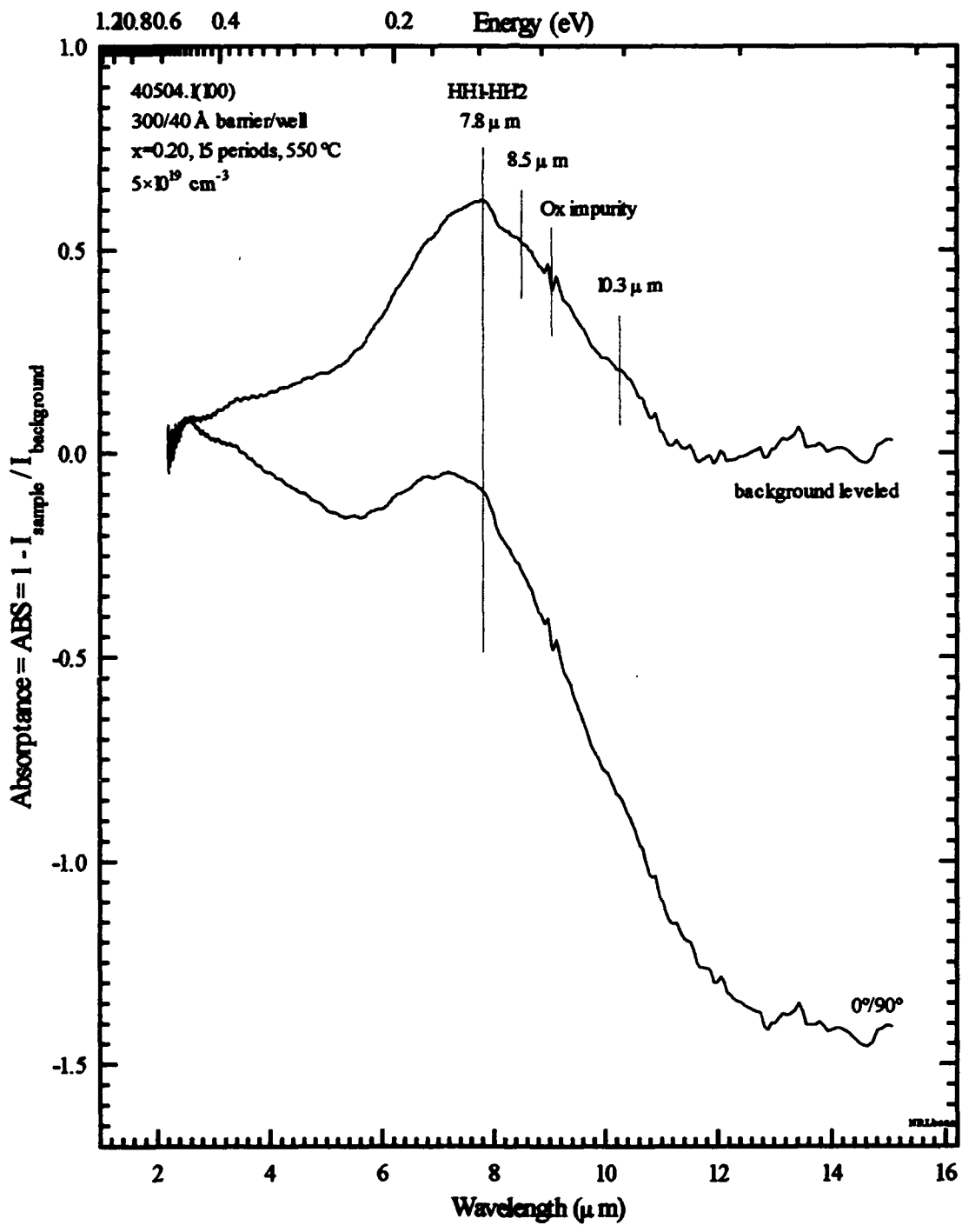


Figure 54. FTIR absorption of SiGe sample 40504.1(100), background leveled (SelfRef).

quantum well samples used in this study were accurate to approximately 20 meV from the measured NP values. These computational results are in close agreement to earlier work at AFIT by Steiner¹⁰⁹ who reported K-P bandgap predictions to within 30 meV.

The average difference in transition energy between the calculated and measured bandgap for each Si substrate was 16 meV for (100) Si, 26 meV for (110) Si, and 18 meV for (111) Si. Since there is less than a 1 meV uncertainty in the PL measurement itself, these differences may be attributed to several computational and growth uncertainties. For example, the K-P model is derived for an *infinite* number of wells and was shown to work well for structures of 20 or more periods. All of the samples used in this study had only 5, 10, or 15 periods. On the other hand, the SQW does not take into account the probability of tunneling from neighboring wells which slightly alters discrete energy levels within the well. In addition, heavy- and light-hole decoupling was assumed for all Si substrates. Later, after examining the appropriate 4×4 Hamiltonian, it will be shown that this is valid assumption for (100) and (111) Si, but not so for (110) Si. This assumption was used in this study for all Si substrates, however, to obtain a first-order approximation.

In addition, small uncertainties in well and barrier widths, and Ge composition also affect the accuracy of the SQW and K-P models when compared to laboratory measurements. Computations indicate that changes in well width from 3 to 5% between growths can easily account for differences of 4-10 meV. Similar changes in Ge composition caused the NP calculation to shift by 12-24 meV. These two effects, considered separately or combined, also affect structural strain which, in turn, affects the quantum energy levels. Changes in energy levels from strain and dopant concentration were also not considered in energy level calculations within the VB well.

Computational studies demonstrated that both models are also sensitive to small changes in effective mass. Changes as small as 5-10% of the effective mass resulted in changes up to 36 meV in some scenarios. The heavy- and light-hole effective masses for

(100), (110), and (111) Si substrates were derived from the matrix elements in the 4×4 Hamiltonian provided by Ikonic¹¹⁰ where

$$\left. \begin{aligned} m_{hh} &= \frac{m_o}{(\gamma_1 - 2\gamma_2)} \\ m_{lh} &= \frac{m_o}{(\gamma_1 + 2\gamma_2)} \end{aligned} \right\} \text{heavy - and light - hole effective mass for (100) Si,}$$

$$\left. \begin{aligned} m_{hh} &= \frac{2m_o}{(2\gamma_1 - \gamma_2 - 3\gamma_3)} \\ m_{lh} &= \frac{2m_o}{(2\gamma_1 + \gamma_2 + 3\gamma_3)} \end{aligned} \right\} \text{heavy - and light - hole effective mass for (110) Si,}$$

and

$$\left. \begin{aligned} m_{hh} &= \frac{m_o}{(\gamma_1 - 2\gamma_3)} \\ m_{lh} &= \frac{m_o}{(\gamma_1 + 2\gamma_3)} \end{aligned} \right\} \text{heavy - and light - hole effective mass for (111) Si.}$$

The Luttinger parameters γ_1 , γ_2 , and γ_3 for the $\text{Si}_{1-x}\text{Ge}_x$ VB wells were computed by linear interpolation as a function of Ge composition from the following values: ¹¹¹

$$\left. \begin{aligned} \gamma_1 &= 4.22 \\ \gamma_2 &= 0.39 \\ \gamma_3 &= 1.44 \end{aligned} \right\} \text{Luttinger parameters for Si,}$$

and

$$\left. \begin{aligned} \gamma_1 &= 13.35 \\ \gamma_2 &= 4.25 \\ \gamma_3 &= 5.69 \end{aligned} \right\} \text{Luttinger parameters for Ge,}$$

These trends were noted while running several simulations and were experimentally observed in interband PL emission and intersubband absorption measurements. PL results indicated that shifts in the NP line are non-linear and become less dramatic as Ge composition increased. For example, changing Ge composition, from $x=0.20$ to $x=0.30$ caused the NP emission line to shift approximately 60-70 meV lower in energy. Changes from $x=0.30$ to $x=0.40$ shifted the NP line approximately 30-40 meV, and so on. FTIR absorption data on (100) SiGe SL samples provided by UCLA indicate that Ge composition changes from $x=0.15$ to $x=0.30$ (with well and barrier widths remaining constant) caused the HH1-HH2 transition to shift 27 meV higher from 9.2 μm to 7.65 μm .

Changes as a Function of Well Width. As the quantum well width decreases in the alloy layer, the bandgap increases slightly as HH1 rises higher from the bottom of the valence band well. In addition, the relative difference between the intersubband levels in the well increases as the bound-state energy levels push out of the well. Therefore, as the well width decreases, interband transitions shift to slightly higher energies (shorter wavelengths). Intersubband transitions also shift to higher energies (shorter wavelengths). Therefore, both interband and intersubband peaks shift in the same direction when well width changes, which is just opposite the case when Ge composition changes.

Determination of Valence Band Selection Rules

The specific selection rules for the first two levels of the heavy- and light-hole states of the valence band of a SiGe superlattice structure were derived from the Luttinger 4×4 bulk Hamiltonian. After properly defining coordinate systems and ordering the four-fold degenerate angular momentum states in the following manner:

$$\left(\left| \frac{3}{2}, \frac{3}{2} \right\rangle, \left| \frac{3}{2}, -\frac{1}{2} \right\rangle, \left| \frac{3}{2}, \frac{1}{2} \right\rangle, \text{ and } \left| \frac{3}{2}, -\frac{3}{2} \right\rangle \right),$$

the original result by Luttinger was extended by Ikonic¹¹⁰ to the following Hamiltonian which has a common form for (100), (110), and (111) structures:

$$H = \begin{pmatrix} T_+ & R & -S & 0 \\ R^* & T_- & 0 & S \\ -S^* & 0 & T_- & R \\ 0 & S^* & R^* & T_+ \end{pmatrix},$$

(* replaces "dagger" for complex conjugate)

where in the (100) case

$$T_{\pm} = \gamma_1(k_x^2 + k_y^2 + k_z^2) \pm \gamma_2(k_x^2 + k_y^2 - 2k_z^2),$$

$$R = (\sqrt{3/2}) [(\gamma_2 + \gamma_3)(k_x - ik_y)^2 + (\gamma_2 - \gamma_3)(k_x + ik_y)^2],$$

$$\text{and } S = 2\sqrt{3}\gamma_3 k_z(k_x - ik_y).$$

For the transition to occur at the center of the two-dimensional Brillouin zone, the envelope functions of the initial and final states must have opposite parities and the dipole operator matrix must have components connecting the envelope components of the initial and final states. Since the first heavy- and light-hole states, HH1 and LH1, are even, the final states must all have odd parity. For $k_x = k_y = 0$, the Hamiltonian reduces to a diagonal matrix which decouples the heavy- and light-hole bands for (100) and (111) Si substrates. As a result, the wave functions for the heavy- and light-hole states may be written¹¹² as the following 4×1 column vectors:

$$\begin{matrix} HH1 & LH1 & \overline{LH1} & \overline{HH1} & HH2 & LH2 & \overline{LH2} & \overline{HH2} \\ \begin{pmatrix} \text{even} \\ 0 \\ 0 \\ 0 \end{pmatrix} & \begin{pmatrix} 0 \\ \text{even} \\ 0 \\ 0 \end{pmatrix} & \begin{pmatrix} 0 \\ 0 \\ \text{even} \\ 0 \end{pmatrix} & \begin{pmatrix} 0 \\ 0 \\ 0 \\ \text{even} \end{pmatrix} & \begin{pmatrix} 0 \\ 0 \\ 0 \\ \text{odd} \end{pmatrix} & \begin{pmatrix} 0 \\ 0 \\ \text{odd} \\ 0 \end{pmatrix} & \begin{pmatrix} 0 \\ \text{odd} \\ 0 \\ 0 \end{pmatrix} & \begin{pmatrix} \text{odd} \\ 0 \\ 0 \\ 0 \end{pmatrix} \end{matrix},$$

where the terms *even* and *odd* represent a shorthand method of denoting complex trigonometric expressions in the subsequent wave functions. An *even* function behaves as $f(x) = f(-x)$ where as an *odd* function behaves as $f(x) = -f(-x)$. Wave functions with $\overline{\text{bars}}$ overhead denote time reversal partners of the unbarred states, i.e. states of the same energy and parallel momentum as the unbarred states, but with spin up and spin down components reversed. The barred states are handled in the same manner as the unbarred states. The selection rules may then be determined by examining the dipole matrix elements generated from the second derivative of the Hamiltonian from the following expression:

$$\left\langle Nk_p \left| \frac{\hbar}{m} \hat{\varepsilon} \cdot \mathbf{p} \right| Mk_p \right\rangle = \hat{\varepsilon} \cdot \sum_{\mu\nu} \left\langle F_\mu(Nk_p, z) \left| \frac{\partial H_{\mu\nu}}{\partial k \partial k_z} \left(\frac{1}{i} \frac{d}{dz} \right) \right| F_\nu(Mk_p, z) \right\rangle,$$

where N and M denote initial and final states at a given k_p (parallel), $\hat{\varepsilon}$ is the polarization vector (or direction of the electric field vector), \mathbf{p} is the momentum vector, z is in the growth direction, and F_μ and F_ν represent the components of the envelope functions. Note, for normal incidence $\hat{\varepsilon}$ may be replaced by E_N (or E_x and E_y), while for parallel incidence, $\hat{\varepsilon}$ may be replaced with E_p (or E_z). Also note, in cases with heavy doping, energy states with higher parallel momenta become occupied allowing transitions away from the center of the Brillouin zone to contribute to absorption. Computing the second derivative of the Hamiltonian for parallel incidence yields

$$\frac{\partial^2 H}{\partial k_z^2} = \frac{\hbar^2}{2m_0} \begin{pmatrix} \gamma_1 - 2\gamma_2 & 0 & 0 & 0 \\ 0 & \gamma_1 + 2\gamma_2 & 0 & 0 \\ 0 & 0 & \gamma_1 + 2\gamma_2 & 0 \\ 0 & 0 & 0 & \gamma_1 - 2\gamma_2 \end{pmatrix}.$$

If $HH1$ is the initial state, only $\overline{HH2}$ is of opposite parity and is connected to $HH1$ via the twice-differentiated Hamiltonian, or

$$(even \ 0 \ 0 \ 0) \begin{pmatrix} \gamma_1 - 2\gamma_2 & 0 & 0 & 0 \\ 0 & \gamma_1 + 2\gamma_2 & 0 & 0 \\ 0 & 0 & \gamma_1 + 2\gamma_2 & 0 \\ 0 & 0 & 0 & \gamma_1 - 2\gamma_2 \end{pmatrix} \begin{pmatrix} odd \\ 0 \\ 0 \\ 0 \end{pmatrix} = \text{some finite value.}$$

Repeating this operation for the light-hole ground state indicates that $LH1 \rightarrow \overline{LH2}$, $\overline{HH1} \rightarrow HH2$, and $\overline{LH1} \rightarrow LH2$ are also valid transitions. These results clearly show that only heavy-hole to heavy-hole, and light-hole to light-hole *intersubband* transitions are allowed for *parallel* incidence light on (100)Si substrates.

Similarly, for normal incidence polarization along the x direction,

$$\frac{\partial^2 H}{\partial k_x \partial k_x} = \frac{\hbar^2}{m_0} \begin{pmatrix} 0 & 0 & -\sqrt{3}\gamma_2 & 0 \\ 0 & 0 & 0 & \sqrt{3}\gamma_2 \\ -\sqrt{3}\gamma_2 & 0 & 0 & 0 \\ 0 & \sqrt{3}\gamma_2 & 0 & 0 \end{pmatrix},$$

which allows the following transitions to occur:

$$\begin{aligned} HH1 &\rightarrow LH2, \quad \overline{HH1} \rightarrow \overline{LH2}, \\ LH1 &\rightarrow HH2, \quad \overline{LH1} \rightarrow \overline{HH2}. \end{aligned}$$

These results indicate that one $LH \leftrightarrow LH$ *intersubband* and three $HH \leftrightarrow LH$ *intervalence-subband* transitions are allowed for *normal* incidence light on (100) Si substrates. To determine the specific selection rules for the non-conventional substrates, this procedure must be repeated for each Si substrate in x, y, and z directions using the Ikonic Hamiltonian with new definitions for its matrix elements.

In the (110) case:

$$T_{\pm} = \left[2\gamma_1(k_x^2 + k_y^2) \mp \gamma_2 k_x^2 \pm 2\gamma_2 k_y^2 \pm 3\gamma_3 k_x^2 + (2\gamma_1 \mp \gamma_2 \mp 3\gamma_3)k_z^2 \right] / 2 ,$$

$$R = (\sqrt{3}/2) \left[-2\gamma_3(k_x - ik_y)^2 + (\gamma_2 - \gamma_3)(2k_y^2 - k_x^2 - 2k_z^2) \right] ,$$

$$\text{and } S = 2\sqrt{3} \left[\gamma_3(k_x - ik_y) + (\gamma_2 - \gamma_3)k_x \right] k_z .$$

In the (111) case:

$$T_{\pm} = (\gamma_1 \pm \gamma_3)(k_x^2 + k_y^2) + (\gamma_1 \mp 2\gamma_3)k_z^2 ,$$

$$R = -2 \left[(\gamma_2 + 2\gamma_3)/\sqrt{3} \right] (k_x - ik_y)^2 + 4 \left[(\gamma_2 - \gamma_3)/\sqrt{6} \right] (k_x + ik_y)k_z ,$$

$$\text{and } S = 2 \left[(2\gamma_2 + \gamma_3)/\sqrt{3} \right] (k_x - ik_y)k_z - 2 \left[(\gamma_2 - \gamma_3)/\sqrt{6} \right] (k_x + ik_y)^2 .$$

When $k_x = k_y = 0$, the matrix elements of the (111) Hamiltonian reduce to a diagonal, just as before in the (100) case. The heavy- and light-hole states are decoupled and the same shorthand wavevectors may be used to determine the selection rules. However, in the (110) case, finite off-diagonal elements exist when $k_x = k_y = 0$ allowing some heavy-hole to light-hole coupling. The wavevectors in the (110) case may be written as

$$\begin{array}{cccccccc} HH1 & LH1 & \overline{LH1} & \overline{HH1} & HH2 & LH2 & \overline{LH2} & \overline{HH2} \\ \left(\begin{array}{c} \text{even} \\ \text{even} \\ 0 \\ 0 \end{array} \right) & \left(\begin{array}{c} \text{even} \\ \text{even} \\ 0 \\ 0 \end{array} \right) & \left(\begin{array}{c} 0 \\ 0 \\ \text{even} \\ \text{even} \end{array} \right) & \left(\begin{array}{c} 0 \\ 0 \\ \text{even} \\ \text{even} \end{array} \right) & \left(\begin{array}{c} 0 \\ 0 \\ \text{odd} \\ \text{odd} \end{array} \right) & \left(\begin{array}{c} 0 \\ 0 \\ \text{odd} \\ \text{odd} \end{array} \right) & \left(\begin{array}{c} \text{odd} \\ \text{odd} \\ 0 \\ 0 \end{array} \right) & \left(\begin{array}{c} \text{odd} \\ \text{odd} \\ 0 \\ 0 \end{array} \right) \end{array} .$$

After much differentiation and matrix manipulation, a summary of the selection rules for heavy- and light-hole levels of the SiGe valence band are shown in Table XII. These selection rules are further summarized pictorially in a valence band energy level schematic shown in Figure 56.

Table XII. Selection rules for allowed valence-band transitions on (100), (110), and (111) Si substrates. Transitions ending in states with (parenthesis) on the (110) substrate indicate a very weak transition due only to heavy-/light-hole mixing.

silicon substrate	electric field incidence	allowed transitions
(100)	parallel	$HH1 \leftrightarrow \overline{HH2}, \overline{HH1} \leftrightarrow HH2$ $LH1 \leftrightarrow \overline{LH2}, \overline{LH1} \leftrightarrow LH2$
(100)	normal	$HH1 \leftrightarrow LH2, \overline{HH1} \leftrightarrow \overline{LH2}$ $LH1 \leftrightarrow HH2, \overline{LH1} \leftrightarrow \overline{HH2}$
(110)	parallel	$HH1 \leftrightarrow \overline{HH2}, \overline{HH1} \leftrightarrow HH2$ $HH1 \leftrightarrow \overline{LH2}, \overline{HH1} \leftrightarrow LH2$ $LH1 \leftrightarrow \overline{HH2}, \overline{LH1} \leftrightarrow HH2$ $LH1 \leftrightarrow \overline{LH2}, \overline{LH1} \leftrightarrow LH2$
(110)	normal	$HH1 \leftrightarrow (HH2), \overline{HH1} \leftrightarrow (\overline{HH2})$ $HH1 \leftrightarrow LH2, \overline{HH1} \leftrightarrow \overline{LH2}$ $LH1 \leftrightarrow HH2, \overline{LH1} \leftrightarrow \overline{HH2}$ $LH1 \leftrightarrow (LH2), \overline{LH1} \leftrightarrow (\overline{LH2})$
(111)	parallel	$HH1 \leftrightarrow \overline{HH2}, \overline{HH1} \leftrightarrow HH2$ $LH1 \leftrightarrow LH2, \overline{LH1} \leftrightarrow LH2$
(111)	normal	$HH1 \leftrightarrow LH2, \overline{HH1} \leftrightarrow LH2$ $HH1 \leftrightarrow \overline{LH2}, \overline{HH1} \leftrightarrow \overline{LH2}$ $LH1 \leftrightarrow HH2, \overline{LH1} \leftrightarrow HH2$ $LH1 \leftrightarrow \overline{HH2}, \overline{LH1} \leftrightarrow \overline{HH2}$

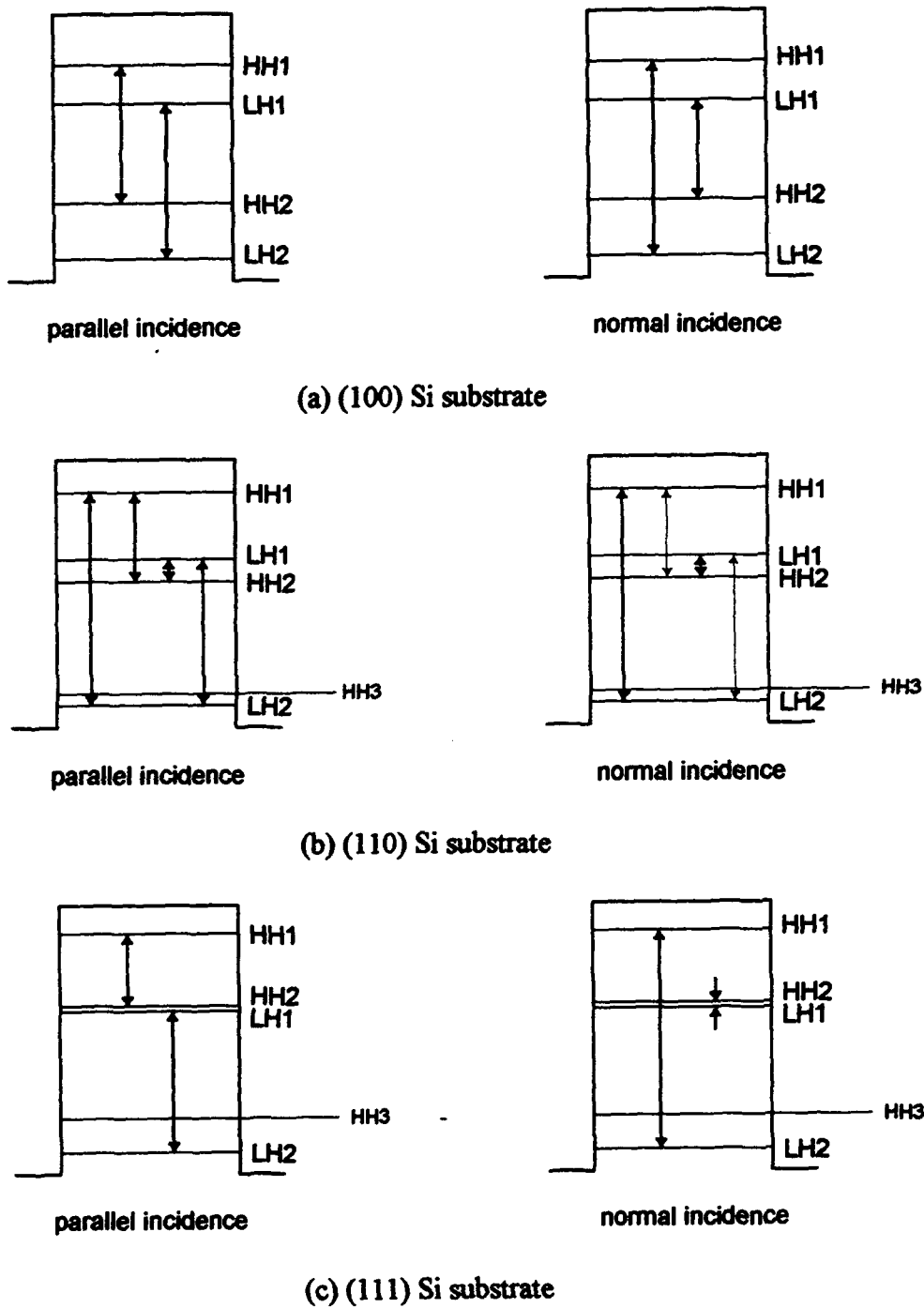


Figure 56. Selection rules for allowed valence-band transitions on (a) (100), (b) (110), and (c) (111) Si substrates.

A single quantum well model was used to compute a first-order approximation of the heavy- and light-hole energy levels contained in the VB well. With a barrier width of 300 Å, tunneling is improbable and the SQW assumption is valid. The energy levels in Figure 56 are shown at their approximate locations in the well. Transitions are illustrated with arrows connecting various levels. Dotted arrows indicate very weak transitions attributed to heavy-/light hole interaction. Moderate doping will cause only the HH1 level to be occupied with holes; therefore, HH1 transitions to other levels should dominate the absorption spectrum. Note that (100) and (111) substrates *only* exhibit intersubband absorption from HH1 during parallel incidence, and *only* intervalence-subband absorption for normal incidence; therefore, both of these substrates should exhibit strong polarization dependence. The (110) substrate, on the other hand, is unique in the sense that it exhibits intersubband *and* intervalence-subband absorption from HH1 at *both* polarizations. Since the HH1 \leftrightarrow LH2 transition on the (110) substrate remains relatively unchanged as a function of polarization, one should not expect to see much difference in the absorption spectrum as a function of polarization using the SubRef or SLRef background subtraction techniques. On the other hand, the SelfRef technique would subtract out a peak attributed to a transition allowed at both polarizations.

Calculations predicting the location of SiGe VB well energy levels vary 20-40% between authors depending on assumptions made regarding HH-LH coupling, strain, doping, and effective mass. Much work has already been accomplished on *n*- and *p*-type SiGe MQWs grown on (100) Si substrates, and limited work on *n*-type (110) and (111) Si substrates; however, little work has been accomplished on nonconventional *p*-type structures such as those used in this study. Only recently, a paper by Kahan *et al.*¹¹³ was published depicting the energy levels on fully-strained (100) and (111) SiGe structures. Their theoretical results for undoped (100) Si_{0.8}Ge_{0.2} predicted the HH1 \leftrightarrow HH2 transition to occur at 12.6 μm. The SQW approximation used in this study predicted the same

transition at 9.9 μm . The intersubband peak observed in NRL sample 40504.1(100) was measured at 7.8 μm . Polarization dependence of the intersubband transition observed agreed with the (100) selection rule.

Note in Figure 56 how the LH1 and HH2 levels for the (110) and (111) Si substrates approach the same energy and actually swap positions for the (111) Si substrate. In (110) and (111) substrates, the HH2 level drops lower in energy while the HH2 and LH1 levels approach the same energy. Allowed intersubband transitions from HH1 to HH2 on (110) and (111) substrates would then be significantly lower in energy (longer wavelength) than in the (100) case. Also note, an intervalence subband transition from HH1 to LH2 is allowed for both polarizations for the (110) substrate.

Results from the SQW model are shown in Table XIII. The HH1 \leftrightarrow HH2 transition on (100) Si was observed at 7.8 μm using the SubRef and SelfRef background subtraction

Table XIII. Transition wavelengths between HH and LH states within the SiGe valence band well.

Si substrate	SQW model results	polarization	transition
(100)	9.9 μm	E_p	HH1 \leftrightarrow HH2
	6.1 μm	E_N	HH1 \leftrightarrow LH2
(110)	14.8 μm	E_p	HH1 \leftrightarrow HH2
	5.4 μm	E_p	HH1 \leftrightarrow LH2
	5.4 μm	E_N	HH1 \leftrightarrow LH2
(111)	18.8 μm	E_p	HH1 \leftrightarrow HH2
	5.3 μm	E_N	HH1 \leftrightarrow LH2

techniques. This peak exhibited strong polarization dependence with the HH intersubband transition strongest when the electric field was rotated perpendicular to the quantum plane (E_p). Free-carrier absorption was dominant when the electric field lay in the quantum plane at normal incidence (E_N). A slight shoulder was observed from 5-7 μm using the SelfRef technique which may be attributed to the HH1 \leftrightarrow LH2 transition allowed at normal

incidence. Strain and dopant concentration were not accounted for in the SQW calculations. In addition, the HH and LH states were assumed uncoupled for all three substrate orientations for the first-order approximation.

In Figure 57, spectra from three doped (110) samples are compared with an undoped SL and a (110) substrate. The boron dopant concentration was varied from $2-8 \times 10^{19}$ atoms/cm³ with no significant change to the relatively featureless spectra on all three doped samples. Small peaks appeared at 2.54, 3.4, 4.64, and 10.3 μm along with an increasingly negative slope which was attributed to significant free-carrier absorption. No intersubband or intervalence-subband peaks were observed on these samples grown on (110) substrates for two reasons. First, SQW calculations indicate that the HH1 \leftrightarrow HH2 transition should occur near 14.8 μm which is outside the transmission bandpass of the optics and coatings in the experimental setup. Second, although the intervalence-subband peak expected at 5.4 μm peak lies within the transmission bandpass, VB selection rules allow this transition to occur at both polarizations. This peak would then be effectively subtracted out as background using the SelfRef technique. In addition, free-carrier absorption, which dominates the spectrum at normal incidence using the SubRef or SLRef subtraction techniques, would overwhelm the signal .

The same spectra are shown in Figure 58 after background leveling. The broad peak at 4.64 μm appears to grow significantly as the boron concentration increases. Another sample was grown for comparison with a dopant concentration of 2×10^{19} cm⁻³ and the Ge composition increased from $x=0.20$ to 0.30. The 2.54, 3.4, 4.64, and 10.3 μm peaks were present but did not change energy as a function of Ge composition; therefore, none of these peaks can be associated to a quantum-well effect.

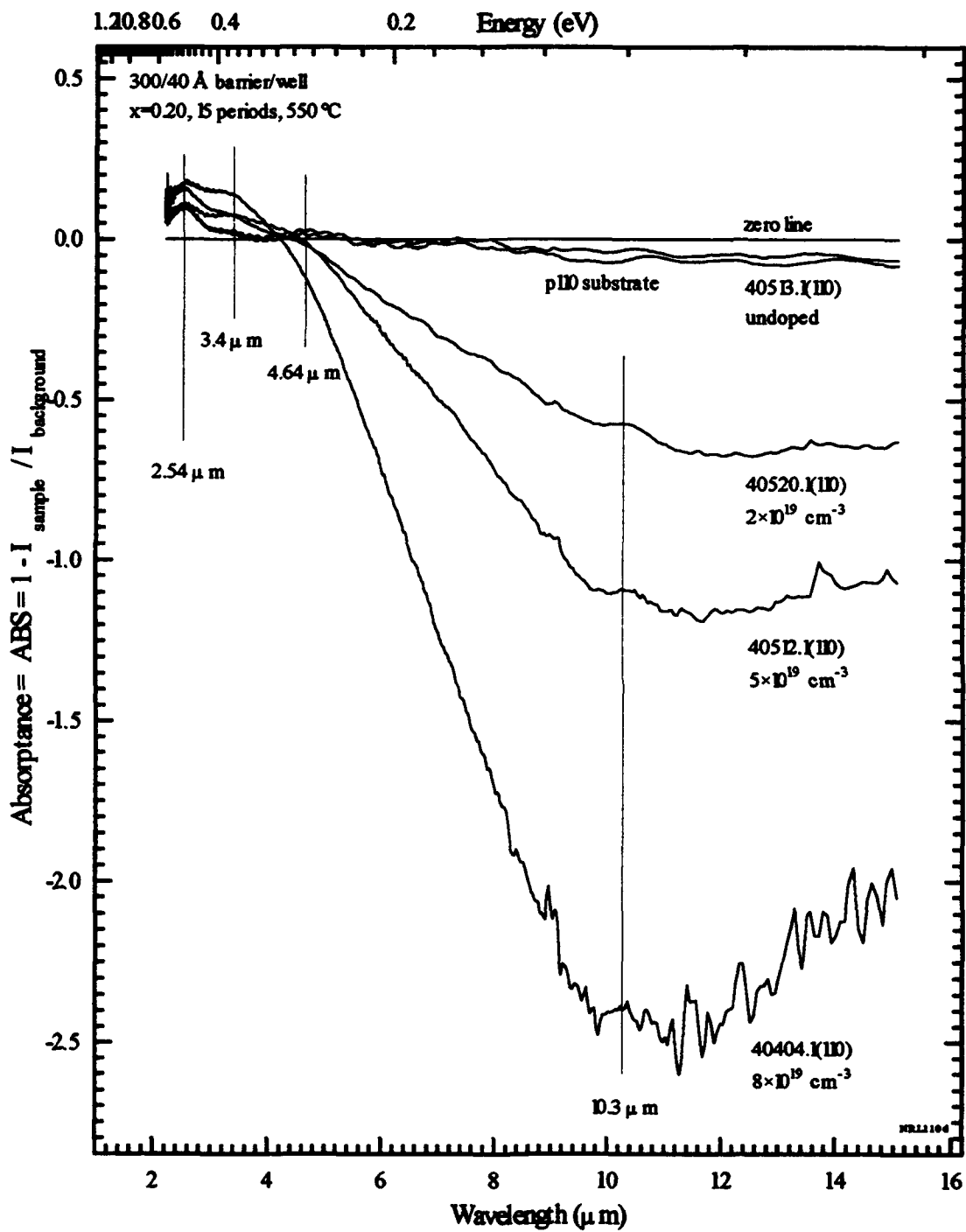


Figure 57. FTIR absorption of similar SiGe (110) structures as a function of boron dopant concentration (SelfRef).

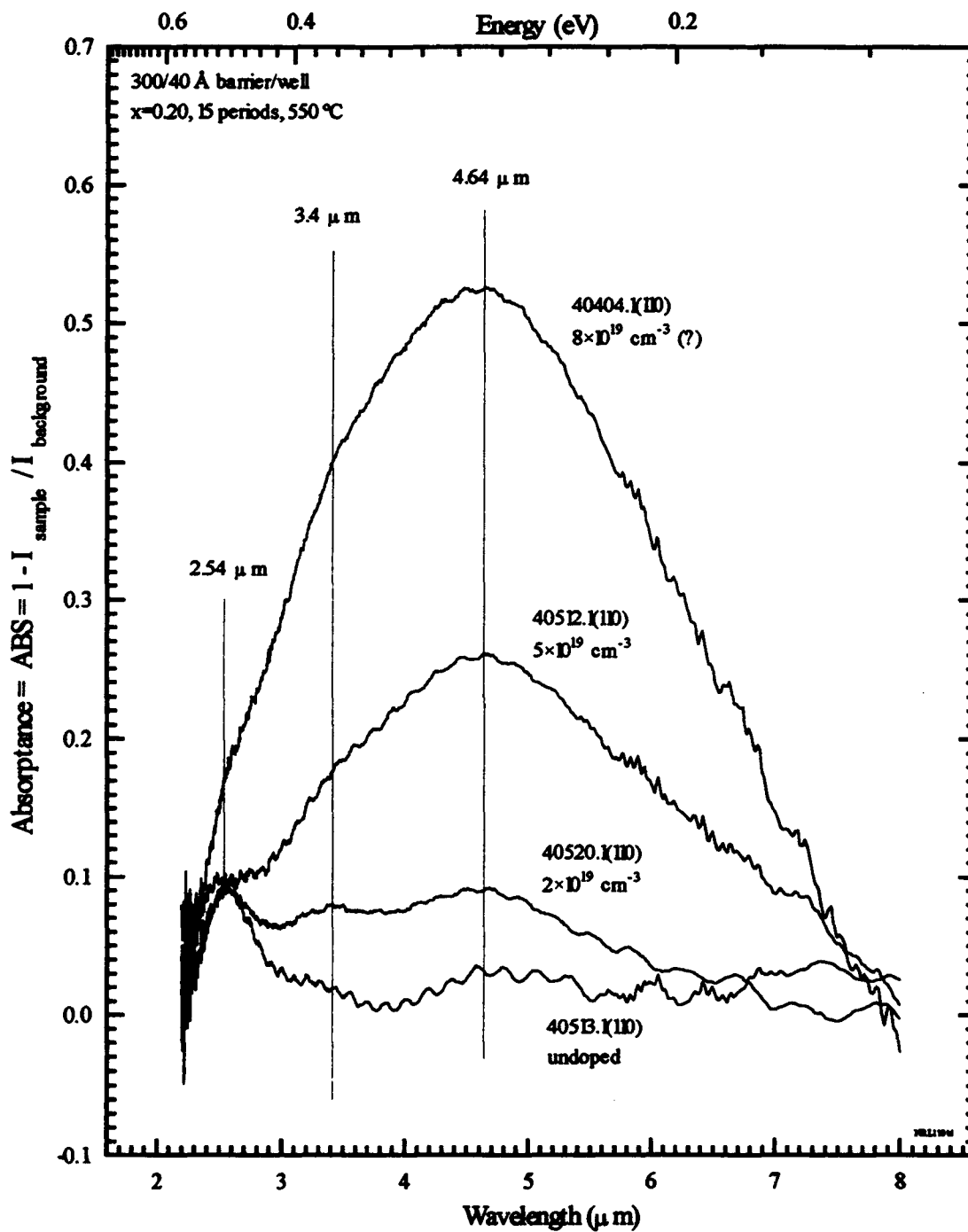


Figure 58. Background-leveled FTIR absorption of similar SiGe (110) structures as a function of boron dopant concentration (SelfRef).

V. Summary

The purpose of this research was to investigate the optical emission and detection properties of several silicon-germanium superlattices grown on (100), (110), and (111) Si substrates with different growth conditions, germanium alloy compositions, and doping concentrations in an ongoing effort to develop a normal-incidence silicon-based detector responsive in the mid-infrared. Over 52 SiGe superlattice structures were grown by MBE at NRL and sent to AFIT. In addition to these samples, 10 InGaAs/AlGaAs superlattice structures grown by MBE at Wright Laboratory, 7 SiGe superlattice samples grown by UHV CVD at Carnegie-Mellon, 3 SiGe superlattice samples grown by MBE at UCLA, and 2 SiGe superlattice samples grown by MBE at AT&T were examined to baseline the experimental apparatus and techniques.

Photoluminescence was used to identify the no-phonon and phonon replica peaks from interband transitions across the $\text{Si}_{1-x}\text{Ge}_x$ bandgap. The most intense PL was observed from superlattices grown at 710 °C for all three Si substrates. The interband no-phonon transition attributed to an exciton bound to a neutral impurity shifted to lower energy as germanium composition increased. The magnitude and direction of energy shifts associated with changes in Ge composition were validated using single quantum well (SQW) and Kronig-Penney models. These models agreed with laboratory measurements to within 16, 26, and 18 meV, for superlattices grown on (100), (110), and (111) Si substrates, respectively. Boron bound-exciton NP, TO, and TA emission peaks were unchanged as a function of Si substrate. Superlattice NP and phonon replicas maintained an energy difference of 58, 49, 34, and 18 meV for $\text{TO}_{\text{Si-Si}}$, $\text{TO}_{\text{Si-Ge}}$, $\text{TO}_{\text{Ge-Ge}}$, and the TA_{Si} , respectively, with no apparent difference in separation energy as a function of Si substrate. PL emission from no-phonon and phonon-replica transitions persisted until sample

temperature reached approximately 24 K for superlattices grown on (100), (110), and (111) Si substrates with an excitation energy density of 0.5 W/cm². Shifts from 2-6 meV from bound-to-free exciton emission was observed as a function of sample temperature. Superlattice uniformity was excellent for samples grown on all three Si substrates. This is the first report of intense, highly-uniform, phonon-resolved PL from a Si_{1-x}Ge_x superlattice grown on a *p*-type (110) Si substrate.

Poor PL at low growth temperatures may be attributed to the segregation of germanium and trace impurities to the top surface of the wafer during growth. This segregation causes fewer radiative electron-hole recombinations in the wells reducing PL emission from the superlattice. The degraded PL at higher growth temperatures is caused by Ge diffusion out of the well at the higher temperatures, effectively broadening the well and causing the well-barrier interfaces to be less abrupt. In addition, other impurities from the walls of the chamber itself may be deposited on the sample at high growth temperatures, trapping charge carriers and creating competing non-radiative transitions. Initial results from TEM studies conducted at the National Institute of Standards and Technology have found no germanium platelets on (110) and (111) Si_{1-x}Ge_x samples grown at low temperature.

Increasing the boron dopant concentration in the SiGe alloy layers significantly reduced PL emission on all three Si substrates. PL from doped structures with varying Ge composition showed degraded PL with the no-phonon and phonon-replica peaks shifting to lower energies as Ge composition was increased. The almost total absence of no-phonon, phonon-replica peaks in superlattices with higher doping levels is attributed to electron-hole interaction being screened by increased free-carrier concentrations. This is the first report of PL from doped SiGe superlattices grown by MBE on (110) and (111) Si substrates.

FTIR absorption measurements were conducted at room temperature as a function of incident electric field polarization on waveguided $\text{Si}_{1-x}\text{Ge}_x$ superlattices grown on (100) and (110) Si substrates. Strong intersubband absorption was observed at $7.8\ \mu\text{m}$ on a 15 period superlattice with $40\ \text{\AA}$ $\text{Si}_{0.8}\text{Ge}_{0.2}$ wells and $300\ \text{\AA}$ Si barriers grown on (100) Si by MBE at $550\ ^\circ\text{C}$. The center $30\ \text{\AA}$ of the wells were boron doped $5 \times 10^{19}\ \text{cm}^{-3}$. The intersubband peak was identified as the HH1 \rightarrow HH2 intersubband transition which exhibited strong polarization dependence according to selection rules. Peak absorption was observed when the polarized electric field vector was rotated 90° out from the quantum plane using the SubRef technique. When \vec{E} was rotated back onto the plane, free-carrier absorption became the dominant transition, increasing linearly as a function of increasing wavelength. The HH1 \rightarrow HH2 peak identification was further confirmed using the SelfRef background-subtraction technique which minimizes the effects from free carriers and provides improved resolution. Using the background-leveled SelfRef technique, small peaks at 2.54 and $10.3\ \mu\text{m}$ were also observed but did not shift as germanium composition was changed, and therefore, cannot be a result of quantum well effects. Intersubband absorption peaks were observed only for doped superlattices grown at $550\ ^\circ\text{C}$.

No absorption peaks attributable to intersubband or intervalence-subband transitions were observed on similar $\text{Si}_{1-x}\text{Ge}_x$ superlattices grown on (110) Si substrates doped from $1\text{--}8 \times 10^{19}\ \text{cm}^{-3}$ with boron. Selection rules indicate that an intersubband transition from HH1 \leftrightarrow HH2 is allowed with the incident electric field polarized parallel to the growth direction; however, the SQW model developed for this study predicts this optical transition lies beyond the transmission bandpass of the experimental apparatus. Another transition from HH1 \leftrightarrow LH2 lies within the transmission bandpass, but is allowed at both incident electric field polarizations. Therefore, this peak is most likely subtracted out as background using the SelfRef technique and is overwhelmed by free-carrier

absorption when examined using the SubRef or SLRef techniques. Increasing the VB well width to decrease the HH1 \leftrightarrow LH2 transition energy provides the most promise for detector applications on a (110) Si substrate: a device response in the 8-9 μm range with a transition allowed for incident light at any polarization.

Valence band selection rules between heavy- and light-hole energy levels for (100), (110) and (111) Si substrates were determined using a 4 \times 4 Hamiltonian. A single quantum well model assuming no strain and uncoupled heavy- and light-holes states was used for a first-order approximation of the transition energy levels for superlattices grown on (100), (110), and (111) Si substrates.

Several details in FTS data interpretation, subtle differences in absorption and transition definitions, waveguide fabrication, and various background-subtraction techniques were presented fully in this work. Absorption results from the SelfRef background-subtraction technique provided a more highly resolved spectrum than the Sub/SLRef technique; however, mastering both techniques is necessary to identify transitions which exhibit unique polarization behavior as a function of selection rules. Results from the single-pass, normal view (SPNV) technique exhibited broad, rounded peaks observed from 3-5 μm which were shown to be due to etalon interference effects between the front surface of the sample and the quantum well-buffer layer interface. Although the SPNV background subtraction technique is a straightforward method to obtain excellent absorption results in many cases, the SPNV technique should be used with caution in this specific application. The Fresnel Angle technique was able to resolve major absorption peaks in *n*-type InGaAs/AlGaAs superlattices but was totally ineffective for *p*-type SiGe superlattices.

There is insufficient evidence to postulate a clear correlation between PL emission and FTIR photo-absorption. The sharpest phonon-resolved PL emission came from undoped Si_{1-x}Ge_x samples grown at 710 °C. The only positive identification of photo-

absorption occurred on heavily-doped samples grown at 550 °C. More work is required to determine exactly why a difference in growth temperature of only 150 °C plays such a critical role for either good PL emission or photo-absorption in a $\text{Si}_{1-x}\text{Ge}_x$ materials system. Initial studies have shown that germanium is well localized in the well at 710 °C. Limited evidence also suggests that as growth temperature is decreased, germanium increasingly segregates forming platelets. On the other hand, the role of dopant concentration in the emission and absorption processes is much easier to correlate. The excess of free carriers needed to lower the Fermi level below the first heavy hole state required for intersubband absorption also screens the electron-hole interaction, which significantly reduces PL emission. So, although sharp PL has always been considered an excellent indicator of crystalline quality, the very conditions necessary to ameliorate intersubband optical absorption quenches interband emission; therefore, PL cannot be used as a relevant diagnostic in determining the absorption properties of a $\text{Si}_{1-x}\text{Ge}_x$ superlattice.

Recommendations for Future Work

There are always questions left unanswered in basic research. The broad PL emission peak found at low energies on SiGe MQWs grown on non-conventional Si substrates should be further investigated as a function of excitation energy. Further research in the photo-absorption properties of non-conventional $\text{Si}_{1-x}\text{Ge}_x$ samples must be continued, especially now that (1) nearly all of the FTIR system unknowns have been answered, (2) (100) and (110) Si samples have been successfully grown and characterized, (3) a first-order approximation of the energy levels has been established, and (4) the heavy- and light-hole selection rules have been determined. Finally, the next logical step in developing a simple detector would be to examine similar structures using photo-response techniques as a function of polarization.

References

- ¹M. J. Kelly, *Sci. Prog.*, **72**, 99 (1988).
- ²C. G. Smith, H. Ahmed, M. J. Kelly and M. N. Wybourne, *Superlattices and Microstructures*, **1**, 153 (1985).
- ³C-I Yang and D-S Pan, *J. Appl. Phys.*, **64**, 1573 (1988).
- ⁴Y. Rajakarunanayake and T.C. McGill, *J. Vac. Sci. Technol. B*, **8**, 929 (1990).
- ⁵S. C. Jain and W Hayes, *Semicond. Sci. Tech.* (UK), **6**, 547 (1991).
- ⁶A. J. Moses, *The Practicing Scientist's Handbook*, Van Nostrand Reinhold Co., pp. 614, 662 (1978).
- ⁷T. Miya, Y. Terunuma, T. Hosaka, and T. Miyashita, *Electron. Lett.*, **15**, 108 (1979).
- ⁸S. Luryi, A. Kastalsky, and J. C. Bean, *IEEE Trans. Elect. Dev.*, **ED-31**, 1135 (1984).
- ⁹E. R. Johnson, and S. M. Christian, *Phys. Rev.*, **95**, 560 (1954).
- ¹⁰R. Braunstein, A. R. Moore, and F. Herman, *Phys. Rev.*, **109**, 695 (1958).
- ¹¹M. Glicksman, *Phys. Rev.*, **111**, 125 (1958).
- ¹²G. C. Osbourne, *IEEE J. Quantum Electron.*, **QE-22**, 1677 (1986).
- ¹³J. C. Bean, L. C. Feldman, A. T. Fiory, S. Nakahara, and I. K. Robinson, *J. Vac. Sci. Technol.*, **A 2**, 436 (1984).
- ¹⁴J. P. Dismukes, L Ekstrom and R. J. Paff, *J. Phys. Chem.*, **68**, 3021 (1964).
- ¹⁵H. Aharoni, *Vacuum*, **28**, 571 (19XX).
- ¹⁶E. Kasper, H. J. Herzog, and H. Kibbel, *Appl. Phys.* **8**, 199 (1975).
- ¹⁷S. Luryi, T. P. Pearsall, H. Temkin, and J. C. Bean, *IEEE Electron Dev. Lett.*, **EDL-7**, 104 (1986).
- ¹⁸H. Temkin, J. C. Bean, A. Antreasyan, and R. Leigbenguth, *Appl. Phys. Lett.*, **52**, 1089 (1988).
- ¹⁹S. S. Iyer G. L. Patton, D. L. Haramé, J. M. C. Stork, E. F. Crabbe, and B. S. Meyerson, *Thin Solid Films*, **184**, 153 (1990).
- ²⁰H.-U.Schreiber, and B. G. Boshch, *Proc. IEEE Electron Devices Meeting*, 643 (1989).
- ²¹A. Y. Cho and J. R. Arthur, *Progress in Solid-State Chemistry*, (Pergamon), **10**, 157 (1975).
- ²²L. Esaki and R. Tsu, *IBM J. Res. Dev.*, **14**, 61 (1970).

-
- ²³G. Döhler, *J. Vac. Sci. Technol.*, **B1**, 278 (1983).
- ²⁴F. Capasso, S. Luryi, W. T. Tsang, C. G. Bethea, B. F. Levine, *Phys. Rev. Lett.*, **51**, 2318 (1983).
- ²⁵R. Dingle, H. L. Störmer, A. C. Gossard, W. Wiegmann, *Appl. Phys. Lett.*, **33**, 665 (1978).
- ²⁶H. M. Manasevit, I. S. Gergis, and A. B. Jones, *Appl. Phys. Lett.* **41**, 464 (1982).
- ²⁷G. Abstreiter, K. Eberl, E. Friess, W. Wegscheider, and R. Zachai, *J. Crystal Growth*, **95**, 431 (1989).
- ²⁸M. Gell, *Appl. Phys. Lett.*, **55**, 484 (1989).
- ²⁹S. Froyen, D. M. Wood, and A. Zunger, *Phys. Rev. B*, **37**, 6893 (1988).
- ³⁰E.E. Anderson, *Modern Physics and Quantum Mechanics*, Saunders:PA, 167 (1971).
- ³¹J.P. McKelvey, *Solid State and Semiconductor Physics*, Krieger:FL, 212 (1986).
- ³²T. P. Pearsall, *J. Luminesc.*, **44**, 367 (1989).
- ³³T. P. Pearsall, *J. Luminesc.*, **44**, 367 (1989).
- ³⁴T. P. Pearsall, *CRC Crit. Rev., Solid State Mater. Sci.*, **15**, 551 (1989).
- ³⁵M. Gell and D. C. Herbert, *Phys. Rev. B.*, **35**, 9591 (1987).
- ³⁶M. Gell, *Phys. Rev. B.*, **38**, 7535 (1988).
- ³⁷S. Satpathy, R. M. Martin, and C. G. Van de Walle, *Phys. Rev. B.*, **38**, 13237 (1988).
- ³⁸S. Froyen, D. M. Wood, and A. Zunger, *Phys. Rev. B.*, **37**, 6893 (1988).
- ³⁹M. Gell, *Phys. Rev. B*, **38**, 7535 (1988).
- ⁴⁰M. Gell, *Phys. Rev. B*, **41**, 7611 (1990).
- ⁴¹M. Gell, *Appl. Phys. Lett.*, **55**, 484 (1989).
- ⁴²U. Gnutzmann, and K. Clausecker, *Appl. Phys.*, **3**, 9 (1974).
- ⁴³J. C. Bean, L. C. Feldman, A. T. Fiory, S. Nakahara, and I. K. Robinson, *J. Vac. Sci. Technol.*, **A2**, 436 (1984).
- ⁴⁴E. Kasper, *Surf. Sci.*, **174**, 630 (1986).
- ⁴⁵E. Kasper, *Festkörperprobleme (Adv. Solid State Phys)*, ed P. Gross, **27**, 265 (1987).
- ⁴⁶H. J. Herzog, H. Jorke, E. Kasper, and S. Mantl, *Proc. Second Int. Symp. on Silicon Molecular Beam Epitaxy*, ed J. C. Bean and L. J. Schowalter (Pennington, NJ: Electrochemical Soc), **58** (1988).
- ⁴⁷R. Zachai, K. Eberl, G. Abstreiter, E. Kasper, and H. Kibbel, *Phys. Rev. Lett.*, **64**, 1055 (1990).

-
- ⁴⁸R. Zachai, E. Friess, G. Abstreiter, E. Kasper, and H. Kibbel, *Proc. of the 19th Int. Conf. on the Physics of Semiconductors*, ed C. Y. Fong, I. P. Batra, and S. Ciraci, Plenum: NY (1988).
- ⁴⁹A. Zrenner, and F. Koch, *Properties of Impurity States in Superlattice Semiconductors*, ed C. Y. Fong, I. P. Batra, and S. Ciraci, Plenum:NY (1988).
- ⁵⁰L. Esaki, and R. Tsu, *IBM J. Research and Development*, **14**, 61 (1970).
- ⁵¹G. H. Döhler, *Phys. Stat. Sol. B*, **52**, 79 (1972).
- ⁵²G. H. Döhler, *Phys. Stat. Sol. B*, **52**, 533 (1972).
- ⁵³G. H. Döhler, *Properties of Impurity States in Superlattice Semiconductors*, ed C. Y. Fong, I. P. Batra, and S. Ciraci, Nijhoff: Dordrecht, 159 (1988).
- ⁵⁴R. F. Gallup and C. Y. Fong, *Phys. Rev. B*, **41**, 5104 (1990).
- ⁵⁵M. Lanoo, and J. Bourgoin, *Point Defects in Semiconductors*, Springer Verlag: Berlin (1981).
- ⁵⁶G. P. Srivastava, *Properties of Impurity States in Superlattice Semiconductors*, ed C. Y. Fong, I. P. Batra, and S. Ciraci, Plenum: NY, 195 (1988).
- ⁵⁷U. Rossler, F. Malcher, and A. Ziegler, *Properties of Impurity States in Superlattice Semiconductors*, ed C. Y. Fong, I. P. Batra, and S. Ciraci, Plenum: NY, 195 (1988).
- ⁵⁸B.E.A. Saleh and M.C.Teich, *Fundamentals of Photonics*, John Wiley & Sons, Inc., (1991).
- ⁵⁹F. Capasso, *Physics and Applications of Quantum Wells and Superlattices*, Plenum:NY, (1987).
- ⁶⁰F. Capasso, W. T. Tsang, G. F. Williams, *IEEE Trans. Electron Devices*, **ED-30**, 381 (1983).
- ⁶¹F. Capasso, *IEEE Trans. Electron Dev.*, **ED-29**, 1388 (1982); F. Capasso, R. A. Logan, and W. T. Tsang, *Electron. Lett.*, **18**, 760 (1982).
- ⁶²E. Gatti, and P. Rehak, *Nucl. Instrum. Methods*, **225**, 608 (1984).
- ⁶³R. Tsu and L. Esaki, *Appl. Phys. Lett.*, **22**, 562 (1973).
- ⁶⁴D. Bohm, *Quantum Theory*, Prentice Hall, 283 (1951).
- ⁶⁵A. Rose, *Concepts in Photoconductivity and Allied Problems*, Wiley & Sons, (1963).
- ⁶⁶F. Capasso, *Phys. Lett.*, **47**, 420 (1985).
- ⁶⁷W. Bloss, M. O'Loughlin, and M. Rosenbluth, *SPIE Infrared Sensors: Detectors, Electronics, and Signal Processing*, **1541**, 2 (1991).
- ⁶⁸B. F. Levine, C. G. Bethea, G. Hasnain, V. O. Shen, E. Pelve, and P. R. Abbott, *Appl. Phys. Lett.*, **56**, 851 (1990).
- ⁶⁹S. D. Gunapala, B. F. Levine, D. Ritter, R. Hamm, and M. B. Panish, *Appl. Phys. Lett.*, **58**, 2024 (1991).

-
- ⁷⁰C. G. Bethea, B. F. Levine, V. O. Shen, R. R. Abbot, and S. J. Hsieh, *IEEE Trans. Electron Devices*, **38**, 1118 (1991).
- ⁷¹L. J. Kozlowski, G. M. Williams, G. J. Sullivan, C. W. Farley, R. J. Andersson, J. K. Chen, D. T. Cheung, W. E. Tennant, and R. E. DeWames, *IEEE Trans. Electron Devices*, **38**, 1124 (1991).
- ⁷²M. Rosenbluth, M. O'Loughlin, W. Bloss, F. DeLuccia, H. Kanger, B. Janousek, E. Perry, and M. Daugherty, *SPIE Quantum-Well and Superlattice Physics III*, **1283**, 82 (1990).
- ⁷³J.S. Park, R.P.G. Karunasiri, and K.L. Wang, *Appl. Phys. Lett.*, **60**(1), 103 (1992).
- ⁷⁴J.P. McKelvey, *Solid State and Semiconductor Physics*, Kreiger Publishing Co.: FL, (1986).
- ⁷⁵Z. Ikonc, V. Milanovic, and D. Tjapkin, *Phys. Rev. B*, **46**, 4285 (1992).
- ⁷⁶A. Kastalsky, S. Luryi, J.C. Bean, and T.T. Sheng, *ECS Proceedings*, 406 (1985).
- ⁷⁷H. Temkin, T.P. Pearsall, J.C. Bean, R.A. Logan, and S. Luryi, *Appl. Phys. Lett.*, **48**, 963 (1986).
- ⁷⁸H. Temkin, J.C. Bean, T.P. Pearsall, N.A. Olsson, and D.V. Lang, *Appl. Phys. Lett.*, **49**, 155 (1986).
- ⁷⁹T.P. Pearsall, H. Temkin, J.C. Bean, and S. Luryi, *IEEE Electron Device Letters*, **EDL-7**, (1986).
- ⁸⁰C.-I. Yang and D.-S. Pan, *J. Appl. Phys.*, **64**, 1573 (1988).
- ⁸¹R.P.G. Karunasiri, J.S. Park, K.L. Wang, and L.-J. Cheng, *Appl. Phys. Lett.*, **56**, 1344 (1990).
- ⁸²Y. Rajakarunanayake and T.C. McGill, *J. Vac. Sci. Technol.*, **B 8**, 929, (1990).
- ⁸³T.L. Lin and J. Maserjian, *Appl. Phys. Lett.*, **57**, 1422 (1990).
- ⁸⁴V.P. Arbet-Engels, R.P.G. Karunasiri, and K.L. Wang, *SPIE Quantum Well and Superlattice Physics III*, **1283**, 229 (1990).
- ⁸⁵R.P.G. Karunasiri, J.S. Park, Y.J. Mii, and K.L. Wang, *Appl. Phys. Lett.*, **57**, 2585 (1990).
- ⁸⁶J.S. Park, R.P.G. Karunasiri, Y.J. Mii, and K.L. Wang, *Appl. Phys. Lett.*, **58**, 1083 (1991).
- ⁸⁷R.P.G. Karunasiri, J.S. Park, and K.L. Wang, *Appl. Phys. Lett.*, **59**, 2588 (1991).
- ⁸⁸J.S. Park, R.P.G. Karunasiri, and K.L. Wang, *Appl. Phys. Lett.*, **60**, 103 (1992).
- ⁸⁹C. Lee and K.L. Wang, *J. Vac. Sci. Technol. B*, **10**, 992 (1992).
- ⁹⁰C. Lee and K.L. Wang, *Appl. Phys. Lett.*, **60**, 2264 (1992).
- ⁹¹Y.-C. Chang and R.B. James, *Phys. Rev. B*, **39**(17), 12672 (1989).
- ⁹²E. D. Richmond, J. G. Pellegrino, M. E. Twigg, S. Qadri, and M. T. Duffy, *Thin Solid Films*, **192**, 287 (1990).

-
- ⁹³A. Ishizaka and Y Shiraki, *J. Electrochem. Soc.*, **133**, 666 (1986).
- ⁹⁴P. E. Thompson, M. E. Twigg, D. J. Godbey, K. D. Hobart, and D. S. Simons, *J. Vac. Sci. Technol. B*, **11**, 1077 (1993).
- ⁹⁵D.E. Aspnes and A.A. Studna, *Physical Review B*, **27**, 985 (1983).
- ⁹⁶G. Davies, *Physics Reports*, **176**, 83 (1989).
- ⁹⁷M.A. Vouk and E.C. Lightowers, *Journal of Luminescence*, **15**, 357 (1977).
- ⁹⁸B.O. Kolbesen, *Applied Phys. Lett.*, **27**, 353 (1975).
- ⁹⁹P.J. Dean, J.R. Haynes, and W.F. Flood, *Phys. Rev.*, **161**, 711 (1967).
- ¹⁰⁰J.C. Sturm, A. St. Amour, Y. Lacroix, and M.L.W. Thewalt, *Applied Phys. Lett.*, **64**, 2291 (1994).
- ¹⁰¹J.-P. Noel, N.L. Rowell, D.C. Houghton, A. Wang, and D.D. Perovic, *Journal of Electronic Materials*, **22**, 739 (1993).
- ¹⁰²E.R. Glaser, T.A. Kennedy, D.J. Godbey, and P.E. Thompson, K.L. Wang, and C.H. Chern, *Phys. Rev. B*, **47**, 1305 (1993).
- ¹⁰³D. Bimberg, M. Sondergeld, and E. Grobe, *Phys. Rev. B*, **4**, 3451 (1971).
- ¹⁰⁴E.C. Lightowers, *Semicon. Sci. and Technol.*, **5**, 1161 (1990).
- ¹⁰⁵M.M. Pradhan, R.K. Garg, and M. Arora, *Infrared Phys.*, **27**, 207 (1987).
- ¹⁰⁶J. Ihm, M.T. Yin, and M.L. Cohen, *Solid-St. Commun.*, **37**, 491 (1981).
- ¹⁰⁷M.T. Yin and M.L. Cohen, *Phys. Rev.*, **B26**, 3259 (1982).
- ¹⁰⁸M.T. Yin and M.L. Cohen, *Phys. Rev. Lett.*, **45**, 1004 (1980).
- ¹⁰⁹T.D. Steiner, *Photoluminescence Study of Si_{1-x}Ge_x/Si and Si/Ge Strained Layer Superlattices*, Dissertation, AFTT/DS/ENP/92-002, (1992).
- ¹¹⁰Z. Ikonc, V. Milanovic, and D. Tjapkin, *Phys. Rev. B*, **46**, 4285 (1992).
- ¹¹¹P. Lawaetz, *Phys. Rev. B*, **4**, 3460 (1971).
- ¹¹²F. Szmulowicz, *discussions on 21 Jun 94 and Derivation of a General Expression for the Momentum Matrix Elements within the Envelop-Function Approximation*, Wright Laboratory, Materials Directorate (WL/MLPO), Wright-Patterson Air Force Base, Ohio, *pending publication*, (1994).
- ¹¹³A. Kahan, M. Chi, and L. Friedman, *J. Appl. Phys.*, **75**, 8012 (1994).

Vita

Captain Theodore (Ted) L. Kreifels was born on 15 February 1958 in Omaha, Nebraska. He graduated from Daniel J. Gross High School in Omaha and enlisted in the United States Air Force in 1976. After working as an avionics technician on F-111 aircraft at Pease AFB and R.A.F. Lakenheath (UK) for five years, he was accepted into the AFIT-sponsored Airman Education and Commissioning Program, and attended the University of Arizona, Tucson, graduating with a Bachelor of Science in Aerospace Engineering in May, 1984. He was commissioned in 1984 from Officer Training School and began his next tour at the 544th Strategic Intelligence Wing, Headquarters Strategic Air Command, Omaha, where he provided operational, test, and intelligence units with US, Soviet, and Chinese missile flight analysis. He entered his second AFIT Civilian Institution program to attend Creighton University, Omaha, where he graduated with a Master of Science in physics in 1988. Captain Kreifels was then assigned to the Imaging Branch of the Phillips Laboratory, Kirtland AFB, Albuquerque, New Mexico where he assisted in the development of a photolytic iodine laser, established the first high-energy laser diagnostic laboratory for imaging, and directed several satellite-imaging field experiments. He was accepted into the School of Engineering, AFIT, to pursue a Ph.D. in engineering physics in July 1991. Captain Kreifels is married to the former Susan J. Kunkel of Tucson; they have one daughter, Donna. He is a member of Sigma Pi Sigma, Tau Beta Pi, and the American Physical Society. After completing his studies, Captain Kreifels will be assigned to the Air Force Maui Optical Tracking Station (AMOS), Phillips Laboratory, Maui, Hawaii.

Permanent Address: Captain Ted Kreifels
c/o Mr. and Mrs. Gerald Kreifels
4513 Bancroft St.
Omaha, NE 68106

REPORT DOCUMENTATION PAGE

Form Approved
GSAF No. 0104-0188

1. AGENCY USE ONLY (leave blank)	2. REPORT DATE August 1994	3. REPORT TYPE AND DATES COVERED Doctoral Dissertation
4. TITLE AND SUBTITLE The Optical Emission and Absorption Properties of Silicon-Germanium Superlattice Structures Grown on Non-Conventional Silicon Substrate Orientations		5. FUNDING NUMBERS
6. AUTHOR(S) Theodore L. Kreifels, Captain, USAF		
7. PERFORMING ORGANIZATION NAME(S) AND ADDRESS(ES) Air Force Institute of Technology WPAFB OH 45433-6583		8. PERFORMING ORGANIZATION REPORT NUMBER AFIT/DS/ENP/94-04
9. SPONSORING MONITORING AGENCY NAME(S) AND ADDRESS(ES) AFOSR/NE (Lt Col Gernot S. Pomrenke) 110 Duncan Ave., Suite B115 Bolling AFB, D.C. 20332-6448		10. SPONSORING MONITORING AGENCY REPORT NUMBER

11. SUPPLEMENTARY NOTES

12a. DISTRIBUTION AVAILABILITY STATEMENT
Approved for public release; distribution unlimited.

12b. DISTRIBUTION CODE

13. ABSTRACT

Optical emission and absorption properties of Si_{1-x}Ge_x/Si superlattices grown on (100), (110), and (111) Si substrates were investigated to determine the optimal growth conditions for these structures to be used as infrared detectors. Fully-strained Si_{1-x}Ge_x/Si superlattices were grown by molecular beam epitaxy (MBE) and examined using low-temperature photoluminescence (PL) to identify no-phonon and phonon-replica interband transitions across the alloy bandgap. Phonon-resolved emission was most intense for undoped quantum wells grown at 710 °C for all three silicon orientations. Room temperature absorption measurements were conducted on (100) and (110) Si_{1-x}Ge_x/Si superlattices using Fourier transform spectroscopy while varying incident electric field polarization. Strong intersubband absorption was observed at 7.8 μm from a sample composed of 15 quantum wells of 40 Å Si_{0.8}Ge_{0.2} separated by 300 Å of Si grown on (100) Si by MBE at 550 °C. Valence band wells were doped 5×10¹⁹ cm⁻³ with boron. This transition, identified as HH1↔HH2, exhibited strong polarization dependence according to (100) Si selection rules. No subband transitions were observed on similar (110) Si_{1-x}Ge_x/Si superlattices ranging in boron dopant concentration from 1-8×10¹⁹ cm⁻³. Selection rules for (110) Si indicate an HH1↔LH2 transition is allowed within the transmission bandpass of the experimental apparatus at both parallel and normal incident electric field polarizations; however, this peak was most likely masked by free-carrier absorption which dominated the spectrum. Intersubband absorption transitions were observed only for doped superlattices grown at 550 °C.